The Dissertation Committee for Bin Wang
certifies that this is the approved version of the following dissertation:

Parallel Simulation of Coupled Flow and Geomechanics in Porous Media

Committee:

Mary Wheeler, Supervisor

Mojdeh Delshad

Rick Dean

Mark Mear

Rui Huang

Parallel Simulation of Coupled Flow and Geomechanics in Porous Media

by

Bin Wang, B.S.

DISSERTATION

Presented to the Faculty of the Graduate School of
The University of Texas at Austin
in Partial Fulfillment
of the Requirements
for the Degree of

DOCTOR OF PHILOSOPHY

THE UNIVERSITY OF TEXAS AT AUSTIN
December 2014

Dedicated to my parents, Mingyu and Ruiyun, my wife, Haiping, and my daughter, Jiale.

Acknowledgments

First and foremost, I would like to express my deepest gratitude to my advisor, Prof. Mary F. Wheeler, for her insightful guidance, invaluable support, and continuous encouragement over the past years. She offered me great opportunities to explore my research interests and broaden my knowledge base. Many profound and fruitful discussions with Prof. Wheeler helped me develop my research topics with clarity and acumen. Her great passion always inspires me to overcome obstacles encountered in my research. I am particularly grateful for the efforts she made to help me complete my work.

Special thanks are given to Dr. Rick H. Dean. I worked as an intern in Chevron with him for three summers. Whenever I have a question, he is always willing to help me with his broad and in-depth knowledge in various aspects of reservoir simulation. He is respectable as an expert, a mentor, and a friend.

I would also like to thank Prof. Mojdeh Delshad, Prof. Mark E. Mear, and Prof. Rui Huang for their time spent on reading my thesis as well as their valuable help with my work. Their constructive feedback and useful suggestions helped me think outside the box and improve my work.

My grateful thanks are also extended to current and former members and collaborators at the Center for Subsurface Modeling at the University of

Texas at Austin. I appreciate the technical help from Prof. Andro Mikelić, Prof. Ivan Yotov, Prof. Gabriel Wittum, Dr. Gergina Pencheva, Dr. Sunil George Thomas, Dr. Ben Ganis, Dr. Arne Nägel, Dr. Ruijie Liu, Dr. Guangri Xue, and Dr. Omar al Hinai.

I would like to acknowledge the U.S. Department of Energy (DOE) for funding the project to couple a geomechanics model with DOECO2, a compositional gas reservoir simulator, under contract number DE-FE0005952.

I am indebted to my parents, Mingyu Wang and Ruiyun Zhou, who provide me with unending love, meticulous care, and moral support all the time. I would also like to express my deepest gratitude to my beloved wife and best friend, Haiping Chen, for her unconditional love and always being with me through ups and downs. Finally, I would like to thank my daughter, Jiale Wang, for her sweet smiles which delight me in these busy days.

Parallel Simulation of Coupled Flow and Geomechanics in Porous Media

Publication No. ____________________

Bin Wang, Ph.D.
The University of Texas at Austin, 2014

Supervisor: Mary Wheeler

In this research we consider developing a reservoir simulator capable of simulating complex coupled poromechanical processes on massively parallel computers. A variety of problems arising from petroleum and environmental engineering inherently necessitate the understanding of interactions between fluid flow and solid mechanics. Examples in petroleum engineering include reservoir compaction, wellbore collapse, sand production, and hydraulic fracturing. In environmental engineering, surface subsidence, carbon sequestration, and waste disposal are also coupled poromechanical processes. These economically and environmentally important problems motivate the active pursuit of robust, efficient, and accurate simulation tools for coupled poromechanical problems.

Three coupling approaches are currently employed in the reservoir simulation community to solve the poromechanics system, namely, the fully implicit

coupling (FIM), the explicit coupling, and the iterative coupling. The choice of the coupling scheme significantly affects the efficiency of the simulator and the accuracy of the solution. We adopt the fixed-stress iterative coupling scheme to solve the coupled system due to its advantages over the other two. Unlike the explicit coupling, the fixed-stress split has been theoretically proven to converge to FIM for the linear poroelasticity model [90, 91]. In addition, it is more efficient and easier to implement than FIM. Our computational results indicate that this approach is also valid for multiphase flow.

We discretize the quasi-static linear elasticity model for geomechanics in space using the continuous Galerkin (CG) finite element method (FEM) on general hexahedral grids. Fluid flow models are discretized by locally mass conservative schemes, specifically, the mixed finite element method (MFE) for the equation of state compositional flow on Cartesian grids and the multipoint flux mixed finite element method (MFMFE) for single phase and two-phase flows on general hexahedral grids. While both MFE and MFMFE generate cell-centered stencils for pressure, MFMFE has advantages in handling full tensor permeabilities and general geometry and boundary conditions. MFMFE also obtains accurate fluxes at cell interfaces. These characteristics enable simulations of more practical problems.

For many reservoir simulation applications, for instance, the carbon sequestration simulation, we need to account for thermal effects on compositional flow phase behavior and solid structure stress evolution. We explicitly couple the poromechanics equations to a simplified energy conservation equation. A time-split scheme is used to solve heat convection and conduction successively. For the convection equation, a higher order Godunov method is employed to capture the sharp temperature front; for the conduction equation, MFE is utilized.

Simulations of coupled poromechanical or thermoporomechanical processes in field scale with high resolution usually require parallel computing capabilities. The flow, geomechanics, and thermodynamics models are modularized in the Integrated Parallel Accurate Reservoir Simulator (IPARS) which has been developed at the Center for Subsurface Modeling at the University of Texas at Austin. The IPARS framework handles structured (logically rectangular) grids and was originally designed for element-based data communication, such as pressure data in flow models. To parallelize the node-based geomechanics model, we enhance the capabilities of the IPARS framework for node-based data communication. Because the geomechanics linear system is more costly to solve than those of flow and thermodynamics models, performance of the linear solver for the geomechanics model largely dictates the speed and scalability of the coupled simulator. We use the generalized minimal residual (GMRES) solver with the BoomerAMG preconditioner from the hypre library and the geometric multigrid (GMG) solver from the UG4 software toolbox to solve the geomechanics linear system [61, 77]. Additionally, the multilevel k-way mesh partitioning algorithm from METIS is used to generate high quality mesh partitioning to improve solver performance.

Numerical examples of coupled poromechanical and thermoporome-

chanical simulations are presented to show the capabilities of the coupled simulator in solving practical problems accurately and efficiently. These examples include a realistic carbon sequestration field case with stress-dependent permeability, a synthetic thermoporoelastic reservoir simulation, two poroelasticity simulations on highly distorted hexahedral grids, and three parallel scalability tests on a massively parallel computer.

Table of Contents

List of Tables

List of Figures

List of Symbols

English and Greek Symbols

$\mathcal{A}$	global mass matrix in MFMFE formulation	125
$\mathbf{a}$	solid matrix displacement test function	42
$\mathbf{a}_h$	displacement test function on finite element space	44
$\bar{\mathbf{a}}$	vector of 8 3-component nodal values of a test function	49
α	Biot's coefficient	17
α^T	solid skeleton thermal expansion coefficient	39
B	Skempton pore pressure coefficient	25
$\mathbf{B}_j$	6×3 strain interpolation matrix associated with vertex j	50
$\mathcal{B}$	strain interpolation matrix	125
$\tilde{\mathcal{B}}$	global pressure difference matrix in MFMFE formulation	125
$\mathbf{C}$	fourth-order stiffness tensor	38
C_{pj}	isobaric molar specific heat capacity of fluid phase j	91
C_{vj}	isochoric molar specific heat capacity of fluid phase j	91
$C_{v,res}$	effective isochoric specific heat capacity	91
C_{vs}	isochoric mass specific heat capacity of solid phase	91
c	diffusivity coefficient	25
c_j	fluid compressibility of phase j	127
c_r	constant rock compressibility	64
DF_E	Jacobian matrix of mapping F_E	48
$\mathcal{D}^e$	elastic constitutive matrix	50
d_{fs}	invariant distance (metrics) for fixed-stress split	21
d_{ud}	invariant distance (metrics) for undrained split	19
δ_{ij}	Kronecker delta	38
$\delta(\cdot)^{k+1}$	$(k+1)^{th}$ Newton iteration solution at $(n+1)^{th}$ time step	67
E	Young's modulus	17
$e(\mathbf{u})$	linearized strain tensor	17
ε_{ij}	total strain tensor	39
ε_v	total volumetric strain	39
ε_{ij}^e	mechanical elastic strain tensor	38
ε_{ij}^T	thermal strain tensor	39
ε_v^e	mechanical volumetric strain	38

$\mathbf{F}^G$	global load vector	55
$\mathbf{f}^e$	local load vector for elasticity problem	54
f_i^j	fugacity of component i in phase j	66
Φ_i^j	fugacity coefficient of component i in phase j	66
ϕ	true porosity	59
ϕ^*	reservoir porosity in coupled poromechanics model	64
G	Lamé's second parameter or shear modulus	38
$\mathbf{g}$	gravitational acceleration vector	59
Γ	external boundary of the domain of interest	36
Γ_t	Neumann boundary for solid mechanics problem	36
$\bar{\Gamma}_t$	Neumann boundary for solid mechanics problem on $\mathcal{T}_h$	44
Γ_u	Dirichlet boundary for solid mechanics problem	36
$\bar{\Gamma}_u$	Dirichlet boundary for solid mechanics problem on $\mathcal{T}_h$	44
γ_{fs}	contraction factor for fixed-stress split	22
γ_{ij}	engineering shear strain	50
γ_{ud}	contraction factor for undrained split	20
$H^1(\Omega)$	Hilbert space on Ω	43
H_E	total thermal energy in Ω_E	93
h	finite element discretization parameter	44
$\mathbf{I}$	second order identity tensor	49
$\mathbf{K}$	absolute permeability tensor	59
$\mathbf{K}^G$	global stiffness matrix for force equilibrium equation	45
$\mathbf{K}^e$	local stiffness matrix for elasticity problem	54
K_{dr}	drained bulk modulus	62
K_f	bulk modulus of fluid	25
K_i	K-value of fluid component i	69
K_s	bulk modulus of solid constituent	25
k	magnitude of isotropic permeability tensor	17
k_i	magnitude of a component of a diagonal permeability tensor	76
k_{rj}	phase relative permeability	59
J_E	determinant of DF_E	48
J_e	determinant of Jacobian of boundary face mapping	52
Λ_o	normalized oil mobility matrix for a vertex in $\mathcal{T}_h$	132
Λ_t	normalized total mobility matrix for a vertex in $\mathcal{T}_h$	131
$\mathbf{\Lambda}_o$	global normalized oil mobility matrix	132
$\mathbf{\Lambda}_t$	global normalized total mobility matrix	132
λ	Lamé's first parameter	38

λ_o	normalized mobility for oil phase	129
λ_T	effective reservoir thermal conductivity	91
λ_t	normalized total mobility for two-phase flow	129
M	Biot's modulus	17
m	fluid mass per bulk volume	17
μ	fluid viscosity	17
μ_j	phase viscosity	59
N_i	molar concentration of component i	59
N_c	number of non-aqueous components in compositional flow model	59
$\bar{N}_i$	total number of moles for component i in a grid block/element	102
$\hat{N}_i$	trilinear shape function of vertex i in reference element $\Omega^{\hat{E}}$	47
$\mathcal{N}$	finite element interpolation matrix	49
$\mathbf{n}$	unit outward normal vector of boundary Γ	41
ν	Poisson's ratio	17
ν_u	undrained Poisson's ratio	25
Ω	domain of interest	36
Ω_i^E	domain of the finite element E_i	44
$\Omega^{\hat{E}}$	unit cube in reference coordinate	46
$(P_n(\hat{E}))^3$	space of 3D polynomials of degree $\leq n$ on $\hat{E}$	116
p	fluid pressure	17
p_{cj}	phase capillary pressure	66
$\mathcal{Q}_{fs}$	solution space for fixed-stress split	22
$\mathcal{Q}_{ud}$	solution space for undrained split	20
q_H	heat source/sink term	91
q_i	component source/sink term	59
q_j	molar injection or production rate per unit volume of phase j	92
$\bar{q}_j$	normalized source/sink term for phase j	128
$\mathbf{r}_i$	location vector of vertex i in $\mathcal{T}_h$	45
$\hat{\mathbf{r}}$	location vector in the reference space	47
$\hat{\mathbf{r}}_j$	location vector of vertex j of the reference cube $\Omega^{\hat{E}}$	48
$\rho_{f,0}$	reference state fluid density	17
ρ_j	molar density of phase j	59
ρ_s	solid phase mass density	59
$\bar{\rho}_j$	normalized density for phase j	128
S_j	saturation of phase j	59
S_T	total saturation of all fluid phases	69
$\mathcal{S}_{fs}$	fixed-stress split operator	22

$\mathcal{S}_{ud}$	undrained split operator	20
s	skin factor	77
$\boldsymbol{\sigma}$	Cauchy (total) stress tensor	17
σ_{ij}^e	effective stress tensor	38
$\boldsymbol{\sigma}^{e+T}$	effective and thermal stress tensor	49
σ_v^e	mean effective stress	38
σ_v	mean total stress	20
σ_{ij}^0	initial (in-situ) stress of the solid matrix	40
ψ_i	displacement basis function associated with vertex i	45
T	current temperature	39
T_0	reference temperature	39
$\mathcal{T}_h$	finite element partition of Ω	43
T_{src}	temperature of injected fluid or temperature at production well	92
τ_c	coupling strength between flow and geomechanics	25
$\boldsymbol{\tau}$	traction boundary condition for solid matrix	41
$\boldsymbol{\tau}_h$	approximate Neumann boundary condition	44
U	solid matrix displacement trial space	43
U_h	displacement trial function space on $\mathcal{T}_h$	44
$\mathbf{u}$	solid skeleton displacement vector	17
$\mathbf{u}_h$	finite element approximation of displacement $\mathbf{u}$	43
$\mathbf{u}_i$	displacement degree of freedom associated with vertex i	45
$\mathbf{u}_D$	solid matrix displacement boundary condition	41
$\bar{\mathbf{u}}$	vector of 8 3-component nodal displacements of a finite element	49
$\bar{\mathbf{u}}_D$	approximate Dirichlet boundary condition	44
$\bar{\mathbf{u}}^G$	global displacement degree of freedom vector	55
V	solid matrix displacement test space	43
$V_b(t)$	bulk volume at reservoir time t	58
V_b^0	initial (reference) bulk volume	58
V_h	displacement test function space on $\mathcal{T}_h$	44
V_p	pore volume	59
V_s	solid grain volume	60
V_t	total fluid volume	103
$\mathbf{v}^D$	Darcy velocity	17
$\mathbf{v}_{fj}$	interstitial velocity of fluid phase j in Eulerian coordinate	59
$\mathbf{v}_s$	solid phase velocity	59
$\mathbf{v}_t^D$	total velocity	128
$\mathbf{v}_j^D$	phase Darcy velocity	59

$\hat{\mathbf{v}}_{ij}$	velocity shape function of vertex $\hat{\mathbf{r}}_i$ in the direction $\hat{\mathbf{n}}_j$	117
ξ_i^j	molar fraction of component i in phase j	59

Chapter 1

Introduction

1.1 Motivation

In the petroleum industry, the coupling of reservoir flow and geomechanical responses poses a variety of challenges to the reservoir engineering community. Examples of such challenges include reservoir compaction, wellbore collapse, sand production, hydraulic fracturing, thermal fracturing, surface subsidence, and the like. Historically, there are many well-known cases with regard to these challenges. For instance, in 1918, the Goose Creek oil field in Texas started to subside because of the extraction of gas, oil, and sand from beneath its surface, which severely damaged the vegetation growth, destroyed the town near the oil field, and caused the disappearance of the Gaillard Peninsula in subsequent years. The geology of the Goose Creek oil field and the causes of its subsidence can be found in [104]. Also, in the early 1940's, the land subsidence of Wilmington oil field in California caused a bowl-shaped area of subsidence reaching a maximum depth of 30 feet, prevented further exploitation of oil, and required considerable work for subsidence control and oil recovery [88]. Moreover, in Belridge diatomite oil field in California, reservoir compaction resulted in an average of 3% well failure rates as well as several million dollars spent on replacement and repair every year in some areas [21].

Practical problems like these cases call for accurate and efficient reservoir simulations in order to characterize reservoir properties, predict well performance, avert operational risks, and increase hydrocarbon production.

Many applications in the petroleum industry involve the interactions among multiphase flow, geomechanical behavior, formation fracturing, and heat transfer. However, conventional reservoir simulations simplify the effect of rock compaction on pore pressure as a constant rock compressibility. It cannot explain the intricate and highly nonlinear multiphysics coupling of multiphase, multicomponent fluid flow and solid mechanics. In recent decades, researchers and engineers have been constantly aware of the importance of coupled geomechanics and reservoir simulations. For this reason, this research aims at developing an accurate and efficient reservoir simulator which couples geomechanical modeling, reservoir simulation, and thermodynamics to simulate complex coupled thermoporomechanical processes in porous media on massively parallel computers.

The coupling of geomechanics and reservoir simulation for practical large scale problems can be quite challenging in the sense of simulator development and computational cost. Consequently, it is very important to choose an efficient coupling approach. There are three major approaches for coupling geomechanics with reservoir simulation, namely, the fully implicit coupling (FIM), the explicit coupling, and the iterative coupling. FIM solves all of the governing equations simultaneously and is the most accurate and stable approach; but it requires massive computation memory and complex nonlinear and linear solvers. The explicit coupling, on the other hand, solves the field equations sequentially. It facilitates the use of specific discretizations and solvers for different field equations, resulting in more scalable simulations on parallel computation platforms. But it has stability and accuracy issues. Similar to the explicit coupling, the iterative coupling solves field equations sequentially. But it also iterates to converge the coupled system at each time step. Properly designed iterative coupling schemes have stability and accuracy similar to FIM, while still enjoying the benefit of good efficiency analogous to the explicit coupling. Considering simulator development cost, solution accuracy, and computation efficiency of the three approaches, the iterative coupling is employed for solving poromechanics problems because high accuracy is desired; and the explicit coupling is utilized to couple the thermal energy balance model with the poromechanics model since temperature changes for the problems we are interested in are relatively small.

Simulations of coupled thermoporomechanical processes in field scale with high resolution usually require parallel computing capabilities. The flow, geomechanics, and thermodynamics models are developed and modularized in IPARS. The IPARS framework handles logically rectangular data and was originally designed for element-based data communication, such as pressure data in flow models. To parallelize the node-based geomechanics model, we enhance the capabilities of the IPARS framework for node-based data communication. Because the geomechanics linear system is much more costly to solve than those of flow and thermodynamics models, performance of the linear solver for the geomechanics model largely dictates the speed and scalability of the coupled thermoporomechanics simulator. We use the GMRES solver with the BoomerAMG preconditioner from the hypre library and the GMG solver from the UG4 software toolbox to solve the geomechanics linear system. Additionally, the multilevel k-way mesh partitioning scheme from METIS is used to produce high quality mesh partitioning to improve solver performance.

1.2 Literature Review

1.2.1 Consolidation Theory

Consolidation theories form the basis of fluid-solid coupling in porous media. In particular, Terzaghi and Biot played an important role in the development of consolidation theories. In 1923, Terzaghi published his classic paper [121] in which his consolidation theory was proposed for the first time and his effective stress principle was fully developed. The reader is referred to the English version of this paper translated by Clayton and Steinhagen [121]. This theory was further developed in Terzaghi [122, 123] and Terzaghi and Peck [124]. Grounded in this theory, the settlement for many types of soil can be predicted, which propelled the development of modern soil mechanics. Also, this theory, particularly the definition of the effective stress, has constructed a useful conceptual framework for engineering applications. Studies and applications of Terzaghi's consolidation theory, to name a few, can be found in Gibson et al. [56], Taylor [120], Znidarcic and Schiffman [148], Schiffman and Znidarcic [112], Carroll and Katsube [28], and Carillo [27].

In spite of the significance of Terzaghi's consolidation theory in modern soil mechanics and other related disciplines, his theory is restricted to the one-dimensional case and ignores the compression of pore fluid and solid grains. In order to overcome these limitations, Biot [14] put forward his general theory of three-dimensional consolidation in 1941 in which the compression of pore fluid and solid grains was taken into account. In his subsequent papers, Biot applied his theory to the calculation of settlement under a rectangular load distribution [13], extended his theory from isotropic materials to anisotropic cases [15] and viscoelastic anisotropic solids [17], discussed the irreversible thermodynamics that is the basis of his theory [20], identified three kinds of elastic waves in poroelastic media [18, 19], and furnished the general solutions to consolidation problems [16].

Because of the interaction between geomechanics and reservoir flow, changes in reservoir stresses greatly influence changes in permeability and porosity, and thus lead to changes in hydrocarbon production. In order to better predict hydrocarbon production and analyze reservoir matrix deformation and stress state, consolidation theories have been widely applied in reservoir engineering [10]. For example, Geertsma [55] introduced a unified treatment of rock mechanics problems related to petroleum engineering. It is in Geertsma's paper that the term *poroelasticity* was coined. Many researchers have extended Biot's consolidation theory to couple multiphase flow models with more general geomechanics models. For example, Li and Zienkiewicz [78] and Gutierrez et al. [60] discussed the interaction between rock deformation and multiphase fluid flow in hydrocarbon reservoirs. Coussy [40, 41] described a general theory of coupled thermo-flow-elastoplasticity model in porous media. Kolditz et al. [75] developed *OpenGeoSys* which solves coupled thermo-hydro-mechanical-chemical processes in porous media. For more studies and applications of consolidation theories in petroleum engineering, the reader is referred to Settari and Walters [115], Dean et al. [47], Thomas et al. [125], Wang et al. [134], Mehrabian and Abousleiman [89], Booker and Small [22], Cryer [42], Rice and Cleary [108], Jha and Juanes [66], Schrefler et al. [113], Sukirman and Lewis [119], Wan [133], etc.

1.2.2 Coupling Approaches

In reservoir and environmental engineering, studies of multiscale and multiphysics phenomena such as surface subsidence, well stability, carbon sequestration, and hydraulic fracturing [46] require a comprehensive understanding of fluid flow and the induced geomechanical responses. However, conventional analyses of fluid flow usually simplify the effect of porous media deformation on pore pressure as a constant rock compressibility [93]. Because the constant rock compressibility assumption is usually only applicable to reservoirs with competent rock, it cannot analyze reservoirs with complex geomechanical behavior especially naturally fractured and stress-sensitive reservoirs [32, 36, 37, 93, 125]. As a result, this conventional decoupled analysis of fluid flow cannot provide enough information on solid phase strains and stresses. To overcome this limitation, coupled analyses of fluid flow and geomechanics are required.

In general, three major approaches have been applied to solving coupled flow and geomechanics problems. They are FIM, the explicit coupling, and the iterative coupling. [72, 91, 116]. FIM solves all governing equations of fluid flow and geomechanics simultaneously [97, 132]. It is the most stable approach, has internal consistency, and preserves second-order convergence for nonlinear iterations [47, 116]. Compared to the other two approaches, however, FIM has extremely high computational cost and requires more code development efforts [38, 47]. Applications of FIM can be found in Chin et al. [36], Gutierrez [59], and Chin and Thomas [37]. The explicit coupling solves two sets of equations in sequence and passes data at selected time steps in both directions between two simulators [94]. This approach has low computational cost and is easy to implement, but it is less accurate and needs to estimate when to update the mechanical response [47, 93, 94]. An example of the explicit coupling can be found in Inoue and Fontoura [65]. The iterative coupling also involves a sequential procedure in which the coupled system is solved iteratively at each time step and the data is passed back and forth between the simulators until the solution converges within an acceptable tolerance [47, 93, 131, 132]. This approach has higher computational cost than the explicit coupling, but it can produce the same results as FIM [47, 81, 94]. For a better understanding of merits and drawbacks of the three approaches, the reader is directed to Dean et al. [47] where the three approaches are compared in the same program, and Tran et al. [130] where the accuracy, adaptability, and running speed of the three approaches are discussed.

1.2.3 Iterative Coupling Schemes

In recent decades, the iterative coupling has gained great popularity in the reservoir simulation community. Chin et al. [38] concluded that the iterative coupling is an effective, robust approach to deal with complicated rock compaction behavior in reservoir simulation. They pointed out that compared to FIM, the iterative coupling has higher computational efficiency, is easier to implement, and can utilize computing technologies and numerical methods for the geomechanics model and the reservoir simulator separately. Tran [127] studied the convergence of the iteratively coupled reservoir simulator and geomechanics module. He developed a porosity formula to improve the efficiency of the iterative coupling between reservoir flow and geomechanical deformation. More applications of the iterative coupling can be found in Samier and De Gennaro [111], Tran et al. [128, 129], Mikelić and Wheeler [91], Thomas et al. [125], etc.

There are four major iterative coupling schemes, including the drained split, the undrained split, the fixed-strain split, and the fixed-stress split [72, 91]. For both the drained and the undrained splits, the mechanical problem is solved first. During the mechanical problem solve, the drained split freezes the pore pressure, whereas the undrained split freezes the fluid mass content. Compared to the drained split, the undrained split is unconditionally stable [73], and can be applied to both linear [66] and nonlinear problems

[8, 73]. Moreover, the undrained split with a fixed number of iterations leads to convergence for a compressible system, whereas the drained split with a fixed number of iterations may not converge even when it is stable [73].

Unlike the drained and the undrained splits, both the fixed-strain and the fixed-stress splits solve the flow problem first. During the flow problem solve, the fixed-strain split fixes the rate of change of the total strain, whereas the fixed-stress split fixes the rate of change of the total stress [74]. Based on a stability analysis, Kim et al. [74] concluded that the fixed-strain split has the same stability behavior as the drained split, that is, conditionally stable. Similar to the undrained split, the fixed-stress split is also unconditionally stable. Moreover, the fixed-stress split is convergent for incompressible systems and is more accurate than the undrained split with a fixed number of iterations [72, 74]. Furthermore, Mikelić and Wheeler [91] proved the convergence and convergence rates of the undrained and the fixed-stress splits.

Because of its advantages, the fixed-stress split has been widely used by researchers in the reservoir simulation community [47, 51, 53, 58, 70, 94, 97, 129, 131]. Using the fixed-stress split with an extended porosity correction, for example, Kim et al. [69] modelled thermo-hydro-mechanical processes in hydrate reservoir. Ganis et al. [52] employed the fixed-stress iterative coupling scheme with inner iterations between reservoir and fracture flows to model fractures in a poroelastic domain. Mikelić et al. [93] applied the fixed-stress iterative coupling for modeling poroelasticity with fracture propagation using a phase field approach.

1.2.4 Mixed Finite Element Method and Multipoint Flux Mixed Finite Element Method

The mixed finite element method (MFE) has been widely used to solve flow and transport problems. Unlike the standard finite element method that employs one single finite element space, MFE utilizes two different finite element spaces for two different variables [34]. Several families of mixed finite element spaces have been introduced in the literature [23, 24, 35, 106]. The primary advantages of MFE include local mass conservation, flux continuity, and the ability to handle discontinuous coefficients. Russell and Wheeler [109] used a special numerical quadrature rule on the lowest order Raviart-Thomas (RT) element [106] to reduce the pressure-velocity system to a cell-centered finite difference (CCFD) system for pressure which is a standard discretization method widely employed by the reservoir simulation community. Weiser and Wheeler [135] then showed first-order convergence for pressure and velocity of CCFD by exploring its relation to MFE and using MFE analysis and numerical quadrature error estimates. Phillips and Wheeler [102] coupled an MFE single phase flow model with a CG linear elasticity model on rectangular grids and demonstrated first-order convergence for pressure, velocity, and displacement.

There are diverse variations of MFE such as the control volume mixed finite element method (CVMFE)[26], the expanded mixed finite element method (EMFE) [33], and the multipoint flux mixed finite element method (MFMFE) [146]. In particular, MFMFE has been implemented for single phase and two-phase flows on general hexahedral grids in IPARS [138, 140]. It is closely related to the multipoint flux approximation method (MPFA) introduced by Aavatsmark [1]. The relation between MPFA and MFE is discussed in [2]. MPFA is a control-volume method which allows local flux elimination to generate a cell-centered pressure system [1]. The primary limitation of MPFA, however, is that its convergence properties cannot be theoretically analyzed due to its non-variational formulation [145].

Wheeler and Yotov developed MFMFE within the MFE variational framework [138, 139, 146]. MFMFE utilizes specifically chosen mixed finite element spaces and quadrature rules to locally eliminate velocity degrees of freedom and generate a cell-centered pressure matrix [118, 146]. This procedure is similar to that in MPFA. MFMFE uses two different mixed finite element spaces including Brezzi-Douglas-Marini (BDM) space on triangles, quadrilaterals, and tetrahedra [146] and the enhanced Brezzi-Douglas-Durán-Fortin (BDDF) space on hexahedra [64, 140]. Two types of quadrature rules are introduced for MFMFE: a symmetric quadrature rule which is accurate for smooth or h^2-perturbed grids [64, 146] and a non-symmetric quadrature rule which is accurate for distorted or h-perturbed grids [140, 144]. While both MFE and MFMFE generate a cell-centered pressure system, MFMFE has advantages in handling full tensor permeabilities and general geometry and boundary conditions [139, 140, 144]. First-order convergence for pressure and velocity has been proved for MFMFE on general quadrilaterals and hexahedra [64, 140, 146]. And first-order convergence for displacement has also been showed when the CG linear elasticity model is coupled to the MFMFE flow model [144]. More details regarding MFMFE can be found in Chapter 5. Because of these advantages, MFMFE has been gaining popularity in the reservoir simulation community [52, 93].

1.3 Dissertation Outline

This dissertation is organized as follows. In Chapter 2, the convergence of two iterative coupling schemes is analyzed numerically. We discuss the undrained and the fixed-stress splits for linear poroelasticity coupling and demonstrate the convergence results for Mandels problem. In Chapter 3, we introduce the isotropic linear elasticity model which will be coupled to different reservoir flow models and a thermal energy balance model in subsequent chapters. Discretization of the geomechanics model using CG FEM and the solution procedure is discussed. In Chapter 4, we iteratively couple the geomechanics model to an equation of state compositional flow model on rectangular grids. Both porosity and permeability couplings are considered. We also explicitly couple a thermal energy balance model to the poromechanics model to account for thermal effects on compositional flow phase behavior and solid skeleton strain and stress evolution. A time-split solution of the energy conservation equation is described. Numerical examples for stress-dependent permeability coupling and thermal coupling are provided. In Chapter 5, we couple the linear elasticity model with MFMFE flow models on hexahedral grids. We illustrate the capability of the poroelasticity model to handle general geometry and boundary conditions by a wellbore model simulation and a reservoir simulation with a distorted hexahedral mesh. In Chapter 6, we present simulation results to validate the parallelization of the coupled elasticity with MFE compositional flow and with MFMFE two-phase flow, respectively. We investigate the scalability of linear solvers for the elasticity model. The effects of mesh partitioning and heterogeneity of rock material properties on solver performance are discussed. In Chapter 7, we summarize contributions and findings from this work and recommend future research directions following this work.

Chapter 2

Numerical Convergence Study of Iterative Coupling Schemes for Poromechanics

2.1 Introduction

In recent decades, the iterative coupling approach has gained great popularity in solving poromechanics problems. Settari and Mourits [115] iteratively coupled a reservoir flow simulator, a 3D mechanics code, and a fracture-propagation model and showed its convergence to the fully implicit coupling. Chin et al. [38] and Dean et al. [47] compared different coupling approaches and pointed out that the iterative coupling is an effective, robust approach to deal with the complicated rock compaction behavior in reservoir simulation. Mainguy and Longuemare [86] and Tran et al. [131] derived porosity correction terms which accelerate the convergence of the iterative coupling scheme. Gai [51], Pan [97], Ganis et al. [53], and Mikelić et al. [90] successfully applied the iterative coupling to solve coupled multiphase flow and geomechanics simulations. Some commercial simulators, CMG for instance [131], also utilize iterative coupling to connect their reservoir flow and geomechanics modules.

Kim et al. [73, 74] analyzed four different iterative coupling schemes widely employed for linear poromechanics simulation. Using Von Neumann stability analysis for linear poroelasticity and an energy method for nonlinear poroplasticity, they concluded that the drained and the fixed-strain splits are only conditionally stable and their stability depends on the coupling strength but not the time step size. They also showed that the undrained and the fixed-stress splits are unconditionally stable. Mikelić and Wheeler [91] rigorously proved the undrained and the fixed-stress iterative coupling schemes are contraction mappings and derived their convergence rates.

In this chapter, we use Mandel's problem as an example to numerically show the fast convergence of the undrained and the fixed-stress splits. Mandel's problem is a classical plane strain poroelasticity problem with an analytical solution. The solution was first given by Mandel in [87] for incompressible fluid and solid constituents. It was later extended by Abousleiman et al. [3] to slightly compressible pore fluid and solid constituents with transverse isotropic and homogeneous materials. It has been used by multiple authors [51, 72, 79, 102] as a benchmark problem because of its non-monotonic pressure dissipation curve which is a characteristic of flow and solid coupling.

2.2 Mandel's Problem

Mandel's problem is described by the isothermal and quasi-static Biot system [3, 41, 87]. A rectangular 2D sample of saturated poroelastic material of width $2a$ and height $2b$ is considered. It is loaded by a constant compressive force applied on rigid impervious plates $y = \pm b$. The force intensity is $2F$. The application of the load is instantaneous at $t = 0^+$. The sample is free to drain laterally at $x = \pm a$ and the lateral edges are stress-free. The mathematical description of Mandel's problem is presented as follows.

Fluid Mass Conservation Equation:

$$\partial_t\left(\frac{m}{\rho_{f,0}}\right) + \nabla \cdot \mathbf{v}^D = 0 \tag{2.1}$$

$$m = m_0 + \rho_{f,0}\alpha\nabla \cdot \mathbf{u} + \frac{\rho_{f,0}}{M}(p - p_0) \tag{2.2}$$

Force Equilibrium Equation:

$$-\nabla \cdot \boldsymbol{\sigma} = 0 \tag{2.3}$$

Darcy's Law:

$$\mathbf{v}^D = -\frac{\mathbf{k}}{\mu}\nabla p \tag{2.4}$$

Effective Stress Relation:

$$\boldsymbol{\sigma} = \frac{E}{1+\nu}e(\mathbf{u}) + \frac{E\nu}{(1+\nu)(1-2\nu)}(\nabla \cdot \mathbf{u})\mathbf{I} - \alpha(p - p_0)\mathbf{I} \tag{2.5}$$

Equations (2.1)–(2.5) are defined on domain $\Omega = (-a, a) \times (-b, b)$ for $t > 0$.

Boundary Conditions:

$$p = 0 \;\text{ and }\; \boldsymbol{\sigma}\mathbf{n}^1 = 0 \;\text{ on }\; x = \pm a, \tag{2.6}$$

$$\begin{gathered} v_2^D = 0,\ \sigma_{12} = 0,\ \int_{-a}^{a} \sigma_{22}\, dx = -2F \\ \text{and }\; u_2 = \text{ an unknown constant on }\; y = \pm b. \end{gathered} \tag{2.7}$$

Initial Conditions:

$$p|_{t=0} = 0;\ m|_{t=0} = m_0;\ \mathbf{u}|_{t=0} = 0 \tag{2.8}$$

In the above equations, $\mathbf{u}$ is the solid skeleton displacement vector; p is fluid pressure; $\boldsymbol{\sigma}$ is Cauchy (total) stress tensor; $e(\mathbf{u})$ is the linearized strain tensor; $\mathbf{I}$ is the second-order identity tensor; k is the magnitude of an isotropic permeability tensor; $\mathbf{v}^D$ is Darcy's velocity; α is Biot's coefficient; $2F$ is the force intensity; μ is the fluid viscosity; M is Biot's modulus; ν is Poisson's ratio; E is Young's modulus; m is fluid mass per bulk volume; $\rho_{f,0}$ is the reference state fluid density. Note that equation 2.2 is only valid for isothermal condition. Thermal effects on solid skeleton deformation and reservoir porosity change will be discussed in Chapter 3 and Chapter 4.

For the simplicity of numerical implementation and without losing the generality of our contraction estimates, we replace the impervious rigid plate condition (2.7) with

$$v_2^D = 0,\ \sigma_{12} = 0, \ \text{ and }\ u_2 = U_2(\pm b, t) \text{ on }\ y = \pm b. \tag{2.9}$$

where $U_2(\pm b, t)$ is the value of the closed form solution to Mandel's problem at $y = \pm b$ [3, 41].

We introduce the functional spaces on Ω

$$V_T = \{\mathbf{z} \in C(0,T] \times H^1(\Omega)^3 \mid \quad z_2 = 0 \text{ on } \ y = \pm b; \\ \text{and } \ \partial_t e(\mathbf{z}) \in L^2(\Omega)^9\} \tag{2.10}$$

$$W_T = \{r \in H^1(\Omega \times (0,T)) \mid r \in C([0,T]; H^1(\Omega)) \\ \text{and } \ r = 0 \ \text{ on } \ x = \pm a\}. \tag{2.11}$$

Multiplication of equations (2.1)-(2.5) by test functions, allows us to write the virtual work formulation

$$\int_\Omega \left(\frac{E}{1+\nu} e(\mathbf{u}) : e(\mathbf{w}) + \frac{E\nu}{(1+\nu)(1-2\nu)} \nabla \cdot \mathbf{u} \nabla \cdot \mathbf{w} \\ -\alpha(p - p_0)\nabla \cdot \mathbf{w} \right) dxdy = 0, \quad \forall \mathbf{w} \in V_T, \tag{2.12}$$

$$\frac{d}{dt} \int_\Omega \left(\frac{p}{M} + \alpha \nabla \cdot \mathbf{u} \right) g \ dxdy + \int_\Omega \frac{k}{\mu} \nabla p \nabla g \ dxdy = 0, \\ \forall g \in W_T. \tag{2.13}$$

$$p|_{t=0} = 0 \quad \text{ and } \mathbf{u}|_{t=0} = 0 \quad \text{ in } \ \Omega. \tag{2.14}$$

2.3 Undrained Split Iterative Method for Mandel's Problem

The *undrained split* iterative method consists in imposing constant fluid mass during the structure deformation. Following [72], this means that we will calculate two pressures: $p^{n+1/2}$ at the half-time step and then p^{n+1}. It should be pointed out that here n denotes the iteration number, not the time step number. We set

$$m^{n+1/2} = m^n \quad \Longrightarrow$$

$$p^{n+1/2} = p^n - \alpha M \text{ div } (\mathbf{u}^{n+1/2} - \mathbf{u}^n). \tag{2.15}$$

Then, using equations (2.1)–(2.5) our iterative process reads as follows

$$-\nabla \cdot \left(\frac{E}{1+\nu} e(\mathbf{u}^{n+1}) + (\frac{E\nu}{(1+\nu)(1-2\nu)} + M\alpha^2)\nabla \cdot (\mathbf{u}^{n+1})\mathbf{I} \right)$$

$$= -\nabla \left(\alpha(p^n - p_0) + M\alpha^2 \nabla \cdot \mathbf{u}^n \right) \tag{2.16}$$

$$\frac{1}{M}\partial_t p^{n+1} - \frac{k}{\mu}\Delta p^{n+1} = -\alpha \nabla \cdot \partial_t \mathbf{u}^{n+1} \tag{2.17}$$

With initial and boundary conditions:

$$p^{n+1}|_{t=0} = 0 \quad \text{and } \mathbf{u}^{n+1}|_{t=0} = 0 \quad \text{on } \Omega, \tag{2.18}$$

$$p^{n+1} = 0 \quad \text{and } e_{12}(\mathbf{u}^{n+1}) = 0 \quad \text{on } x = \pm a, \tag{2.19}$$

$$\frac{E}{1+\nu}\frac{\partial u_1^{n+1}}{\partial x} + (\frac{E\nu}{(1+\nu)(1-2\nu)} + M\alpha^2)\nabla \cdot \mathbf{u}^{n+1}$$

$$= \alpha(p^n - p_0) + M\alpha^2 \nabla \cdot \mathbf{u}^n \text{ on } x = \pm a, \tag{2.20}$$

$$\frac{\partial p^{n+1}}{\partial y} = 0, \; e_{12}(\mathbf{u}^{n+1}) = 0 \text{ and } u_2^{n+1} = U_2(\pm b, t) \quad \text{on } y = \pm b. \tag{2.21}$$

Following the approach from [91], we introduce the invariant distance (the metrics) d_{ud}, given by

$$d_{ud}^2\left((\mathbf{u}, p), 0 \right) = \frac{k}{\mu M} \max_{0 \le t \le T} ||\nabla p(t)||^2_{L^2(\Omega)}$$

$$+ \frac{2E\alpha^2}{E\nu/(1-2\nu) + M\alpha^2(1+\nu)} ||e(\partial_\tau \mathbf{u})||^2_{L^2(\Omega\times(0,T))^3}$$

$$+\alpha|| \text{ div } \partial_\tau \mathbf{u}||^2_{L^2(\Omega\times(0,T))}$$

$$+|| \underbrace{\partial_\tau(\frac{1}{M}p + \alpha \text{ div } \mathbf{u})}_{\partial_t m/\rho_{f,0}} ||^2_{L^2(\Omega\times(0,T))}. \tag{2.22}$$

The distance is defined on the space $\mathcal{Q}_{ud}$:

$$\mathcal{Q}_{ud} = \{(\mathbf{A}, B) \in V_T \times W_T \mid \mathbf{A}|_{t=0} = \mathbf{0}; B|_{t=0} = 0 \}. \tag{2.23}$$

We have

$$d_{ud}\Big((\mathbf{u}^{n+1}, p^{n+1}) - (\mathbf{u}^n, p^n)\Big) \leq \gamma_{ud} d_{ud}\Big((\mathbf{u}^n, p^n) - (\mathbf{u}^{n-1}, p^{n-1})\Big) \tag{2.24}$$

with $\gamma_{ud} = \dfrac{M\alpha^2}{E\nu/(1+\nu)(1-2\nu) + M\alpha^2} < 1$. We see that the operator $\mathcal{S}_{ud}$, defined as

$$\mathcal{S}_{ud}(\mathbf{u}^n, p^n) = (\mathbf{u}^{n+1}, p^{n+1}) \tag{2.25}$$

is a contraction mapping on $\mathcal{Q}_{ud}$. By the **contraction mapping principle**, it has a unique fixed point in $\mathcal{Q}_{ud}$. This proves the convergence of the undrained split iterative method.

2.4 Fixed-stress Split Iterative Method for Mandel's Problem

The *fixed-stress split* iterative method consists in imposing constant mean total stress. This means that the $\sigma_v = \sigma_{v,0} + K^*_{dr} \operatorname{div} \mathbf{u} - \alpha(p - p_0)$ is kept constant at half-time step where σ_v is the mean total stress. K^*_{dr} is a generalized drained bulk modulus of the solid matrix under different boundary conditions. Chen et al. [32] gives K^*_{dr} for uniaxial, biaxial, and triaxial strain conditions. Assume $K^*_{dr} = \frac{\alpha^2}{\beta}$, mathematically we can choose K^*_{dr} to achieve an optimal convergence rate for the fixed-stress iterative coupling. We should point out that the choice of the optimal K^*_{dr} depends on the definition of the distance in the solution space. The iterative process reads as follows

$$\sigma_v^{n+1/2} = \sigma_v^n \Longrightarrow$$

$$\text{div } \mathbf{u}^{n+1/2} = \text{ div } \mathbf{u}^n + \frac{\alpha}{K_{dr}^*}(p^{n+1/2} - p^n) \tag{2.26}$$

$$\begin{aligned}\Big(\frac{1}{M} + \beta\Big)\partial_t p^{n+1} - \frac{k}{\mu}\Delta p^{n+1} &= -\frac{\beta}{\alpha}\partial_t \sigma_v^n \\ &= -\alpha \text{ div } \partial_t \mathbf{u}^n + \beta \partial_t p^n;\end{aligned} \tag{2.27}$$

$$\text{div } \{\frac{E}{1+\nu} e(\mathbf{u}^{n+1}) + \frac{E\nu}{(1+\nu)(1-2\nu)}(\nabla \cdot \mathbf{u}^{n+1})\mathbf{I}\} = \alpha \nabla p^{n+1}; \tag{2.28}$$

With initial and boundary conditions:

$$p^{n+1}|_{t=0} = 0 \quad \text{ and } e_{12}(\mathbf{u}^{n+1}) = 0 \quad \text{on } \Omega; \tag{2.29}$$

$$p^{n+1} = 0 \text{ and } e_{12}(\mathbf{u}^{n+1}) = 0 \text{ on } x = \pm a, \tag{2.30}$$

$$\begin{aligned}&\frac{E}{1+\nu}\frac{\partial u_1^{n+1}}{\partial x} + \frac{E\nu}{(1+\nu)(1-2\nu)}\nabla \cdot \mathbf{u}^{n+1} \\ &-\alpha(p^{n+1} - p_0) = 0 \text{ on } x = \pm a,\end{aligned} \tag{2.31}$$

$$\begin{aligned}&\frac{\partial p^{n+1}}{\partial y} = 0, \ e_{12}(\mathbf{u}^{n+1}) = 0 \\ &\text{and } u_2^{n+1} = U_2(\pm b, t) \text{ on } y = \pm b;\end{aligned} \tag{2.32}$$

Again, following the approach from [93], we introduce the invariant distance (the metrics) d_{fs} , given by

$$\begin{aligned}&d_{fs}^2\Big((\mathbf{u}, p), 0\Big) = \\ &\frac{k}{\mu}\frac{\alpha^2}{\frac{1}{M} + \beta}\max_{0\le t\le T} ||\nabla p(t)||^2_{L^2(\Omega)} \\ &+\frac{4E^2\nu}{(1+\nu)^2(1-2\nu)}||e(\partial_t \mathbf{u})||^2_{L^2(\Omega\times(0,T))^3} \\ &+||\underbrace{\partial_t(-\alpha p + K_{dr}^* \text{ div } \mathbf{u})}_{\partial_t\sigma_v}||^2_{L^2(\Omega\times(0,T))}\end{aligned} \tag{2.33}$$

The distance is defined on the space $\mathcal{Q}_{fs}$:

$$\mathcal{Q}_{fs} = \{(\mathbf{A}, B) \in V_T \times W_T \mid \mathbf{A}|_{t=0} = \mathbf{0}; B|_{t=0} = 0 \,\}. \tag{2.34}$$

We have

$$\begin{aligned} & d_{fs}\Big((\mathbf{u}^{n+1}, p^{n+1}) - (\mathbf{u}^n, p^n) \Big) \\ & \leq \gamma_{fs} d_{fs}\Big((\mathbf{u}^n, p^n) - (\mathbf{u}^{n-1}, p^{n-1}) \Big) \end{aligned} \tag{2.35}$$

With the distance (2.33), the optimal K_{dr}^* from our derivation is $K_{dr}^* = \dfrac{2E\nu}{(1+\nu)(1-2\nu)}$, or $\beta = \dfrac{\alpha^2(1+\nu)(1-2\nu)}{2E\nu}$. Hence $\mathcal{S}_{fs}$, defined as

$$\mathcal{S}_{fs}(\mathbf{u}^n, p^n) = (u^{n+1}, p^{n+1}) \tag{2.36}$$

is a contraction mapping on $\mathcal{Q}_{fs}$, and by the **contraction mapping principle**, it has a unique fixed point in $\mathcal{Q}_{fs}$. This proves the convergence of the fixed-stress split iterative method. And now the contraction factor is $\gamma_{fs} = \dfrac{\alpha^2 M}{\alpha^2 M + \frac{2E\nu}{(1+\nu)(1-2\nu)}} < 1$.

It is obvious that $\gamma_{fs} < \gamma_{ud}$, which means the fixed-stress split has a higher convergence rate than the undrained split. Actually, if we drop the elastic energy term

$$\frac{4E^2\nu}{(1+\nu)^2(1-2\nu)} ||e(\partial_t \mathbf{u})||^2_{L^2(\Omega\times(0,T))^3}$$

in (2.33) to define a weaker distance, following the procedure in [93], we can show that now the optimal $K_{dr}^* = \dfrac{2E(1-\nu)}{(1-2\nu)(1+\nu)}$, or $\beta = \dfrac{\alpha^2(1-2\nu)(1+\nu)}{2E(1-\nu)}$. And the contraction factor under the weaker distance is

$$\gamma_{fs} = \frac{\alpha^2 M}{\alpha^2 M + \frac{2E(1-\nu)}{(1-2\nu)(1+\nu)}} < 1$$

In the following chapters we will also see that we can couple this mechanics module to existing flow simulators without introducing any new terms into flow equations. Therefore it is preferable to develop iteratively coupled poromechanics simulators using the fixed-stress split.

2.5 Numerical Results for Mandel's Problem

We will show converged results from the undrained split and the fixed-stress split for the Mandel's problem. Figure 2.1 illustrates the configuration of the Mandel's problem. From the symmetry of the problem, only a quarter rectangle ($(x, y) \in (0, a) \times (0, b)$) is modeled in the simulation (Figure 2.2). An iteratively coupled 3D single phase flow with linear elasticity model in IPARS is used to simulate the 2D problem. Therefore a plane strain condition ($e_{33} = 0$) is enforced in the simulation. For the quarter rectangle domain, we have the following boundary conditions:

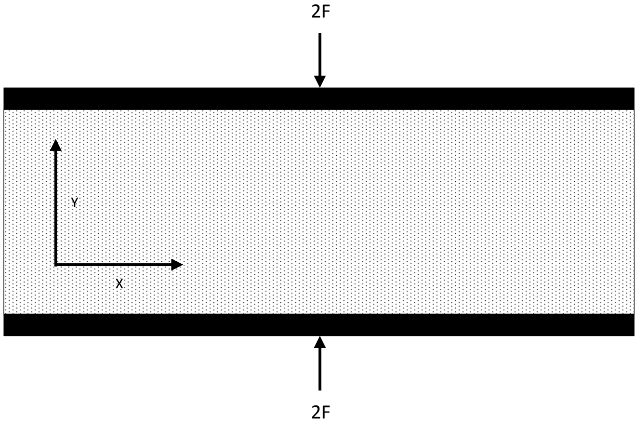

Figure 2.1: Mandel's problem full domain

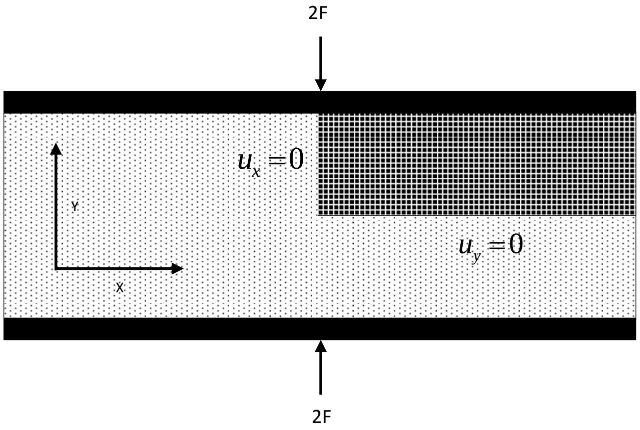

Figure 2.2: Mandel's problem quarter domain

$$p = 0 \text{ and } \boldsymbol{\sigma}\mathbf{n}^1 = 0 \text{ on } x = +a, \tag{2.37}$$

$$v_2^D = 0, \sigma_{12} = 0, u_2 = U_2(b,t) \text{ on } y = b, \tag{2.38}$$

$$v_1^D = 0, u_1 = 0, \sigma_{12} = 0 \text{ on } x = 0, \tag{2.39}$$

$$v_2^D = 0, u_2 = 0, \sigma_{12} = 0 \text{ on } y = 0. \tag{2.40}$$

Abousleiman et al. [3] presents an analytical solution for the pore pressure, displacements, and stresses for the Mandel's problem with transverse isotropic material and compressible pore fluid and solid constituents. For an isotropic material, a simplified analytical solution is shown in [102]. Based on the analytical solution, an instantaneous pressure rise and deformation response should be observed upon the exertion of the compressive load $2F$ [51]:

$$\Delta p(x, y, 0^+) = FB(1+\nu_u)/3a \tag{2.41}$$

$$u_1(a, y, 0^+) = F\nu_u/2G \tag{2.42}$$

$$u_2(x, b, 0^+) = -Fb(1-\nu_u)/2Ga \tag{2.43}$$

where B is the Skempton pore pressure coefficient, defined as

$$B = 1 - \frac{\phi K_{dr}(K_s - K_f)}{K_f(K_s - K_{dr}) + \phi K_{dr}(K_s - K_f)}$$

and ν_u is the undrained Poisson's ratio:

$$\nu_u = \frac{3\nu + B(1-2\nu)(1-K_{dr}/K_s)}{3 - B(1-2\nu)(1-K_{dr}/K_s)}$$

G is the shear modulus. K_s and K_f denote the bulk modulus of solid constituent and fluid, respectively. Another parameter in the analytical solution of Mandel's problem is the diffusivity coefficient c :

$$c = \frac{2kB^2G(1-\nu)(1+\nu_u)^2}{9\mu(1-\nu_u)(\nu_u-\nu)}$$

Input parameters for Mandel's problem are listed in Table 2.1. The solid constituent is assumed to be incompressible ($\alpha = 1.0$) while the fluid is slightly compressible. The coupling strength $\tau_c = \frac{\alpha^2 M}{K_{dr}}$ is 5.0 in our simulation, which is considered as a strong coupling strength in [72]. Our contraction estimates show that the coupling strength controls the convergence rates for both the undrained and the fixed-stress iterative coupling schemes. As the coupling strength increases, convergence rates decrease. Also, for the choice of

SYMBOL	QUANTITY	VALUE
a	dimension in x	100 m
b	dimension in y	10 m
E	Young's modulus	5.94×10^9 Pa
F	force intensity	5.94×10^8 Pa/m
ν	Poisson's ratio	0.2
c_f	fluid compressibility	$3.03 \times 10^{-10}\ /Pa$
α	Biot's constant	1.0
k	permeability	100 md
ϕ	initial porosity	0.2
μ	fluid viscosity	1.0 cp
Δx	grid spacing in x	2.5 m
Δy	grid spacing in y	0.25 m
Δt	time step size	10 s
t_T	total simulation time	50000 s
B	Skempton coefficient	0.83333
ν_u	undrained Poisson's ratio	0.44
M	Biot's modulus	1.65×10^{10} Pa
c	diffusivity coefficient	0.465 $m^2 s^{-1}$

Table 2.1: Input parameters for Mandel's problem

input parameters herein, we calculate that $\gamma_{ud} = 0.9302$ and $\gamma_{fs} = 0.8696$. We expect the fixed-stress splitting to converge faster than the undrained splitting.

We show that numerical solutions from both the undrained and the fixed-stress splits converge to the analytical solution from $t = 0^+$ in Figures 2.3 and 2.4. Curves of the same color in Figures 2.3 and 2.4 are for the same time step. Both iterative coupling schemes are able to catch Mandel-Cryer effect which is a well-known feature of the coupled model (the pressure decay is not monotonic). For the undrained split, the convergence criteria for the iterative coupling are

$$\begin{gathered}\left\| \frac{1}{M}\left(p^{n+1} - p^{n+1/2}\right)/\phi^{*,n+1} \right\|_\infty < TOL1 \\ \|R^{n+2}_{mech}\|_\infty < TOL2 \end{gathered} \tag{2.44}$$

where $\phi^* = m/\rho_{f,0}$ is the reservoir porosity and R^{n+2}_{mech} is the residual of the force equilibrium equation using p^{n+1} and $\mathbf{u}^{n+1}$. For the fixed-stress split, the convergence criteria for the iterative coupling are

$$\begin{aligned} \left\| \left(\alpha \nabla \cdot \mathbf{u}^{n+1} - \beta p^{n+1} \right) / \phi^{*,n+1} \right\|_\infty &< TOL1 \\ \left\| R^{n+2}_{flow} \right\|_\infty &< TOL2 \end{aligned} \tag{2.45}$$

where R^{n+2}_{flow} is the residual of the flow volume conservation equation using p^{n+1} and $\mathbf{u}^{n+1}$. In order to match the analytical solution accurately, we set tolerances $TOL1 = 1.0 \times 10^{-6}$ and $TOL2 = 1.0 \times 10^{-9}$ for both iterative coupling schemes. Figure 2.5 shows the number of iterations of the two splitting schemes for given tolerances at each time step. Due to the discontinuity (lack of regularity) of the solution at $t = 0^+$, the undrained split takes 35 iterations to converge at the first time step whereas the fixed-stress split only takes 5 iterations. The number of iterations of the fixed-stress split decreases to 2 within 10 time steps. As a comparison, the undrained split takes more than 5 iterations for the first 1570 time steps. Since the convergence criteria are not exactly the same for the undrained and the fixed-stress splits, we need to investigate whether the undrained split takes more iterations to converge because its convergence tolerances are tighter. To this end, we set the maximum number of iterations to 5 and compare the numerical results from the two iterative coupling schemes in Figures 2.6–2.7. Figure 2.8 shows the number of iterations of the two splitting schemes when the maximum number of iterations is set to 5. It is clear that for t=10s, the undrained split solution does not converge within 5 iterations. For t=50s, the pressure solution from the undrained split is not accurate either. The horizontal displacement u_1 (or u_x) at y=b from the undrained split within 5 iterations matches the analytical solution quite well except for t=10s and $x/a \geq 0.9$. The reason is that the exact vertical displacement u_2 (or u_y) at y=b is prescribed as the Dirichlet boundary condition. The choice of the displacement boundary condition also prevents the error of the undrained split pressure solution from propagating as time proceeds. Note that the fixed-stress split solution converges to the analytical solution within 5 iterations for all time steps. This result confirms our theoretical proof that the fixed-stress split converges faster than the undrained split when the appropriate K_{dr}^* is selected.

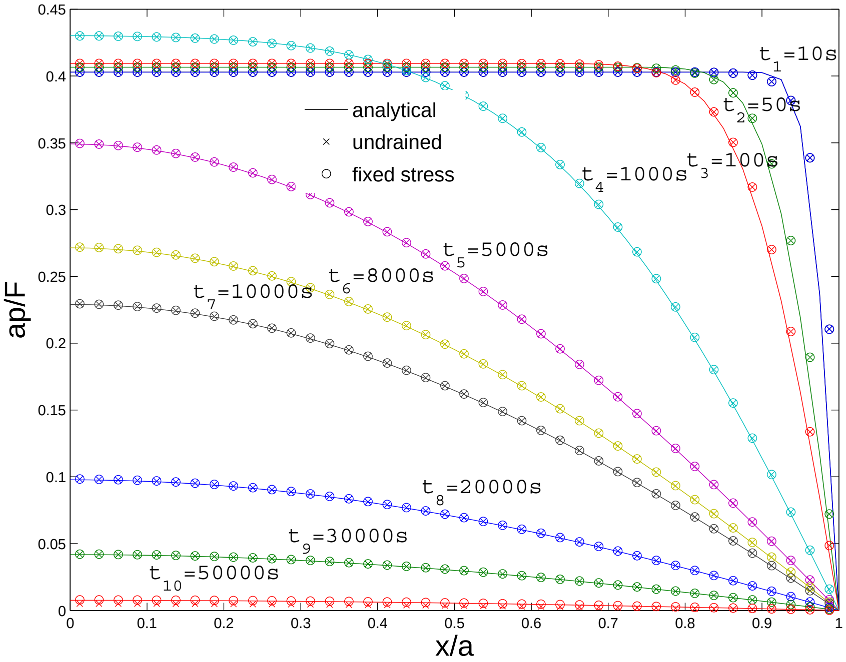

Figure 2.3: Pressure matching result for Mandel's problem

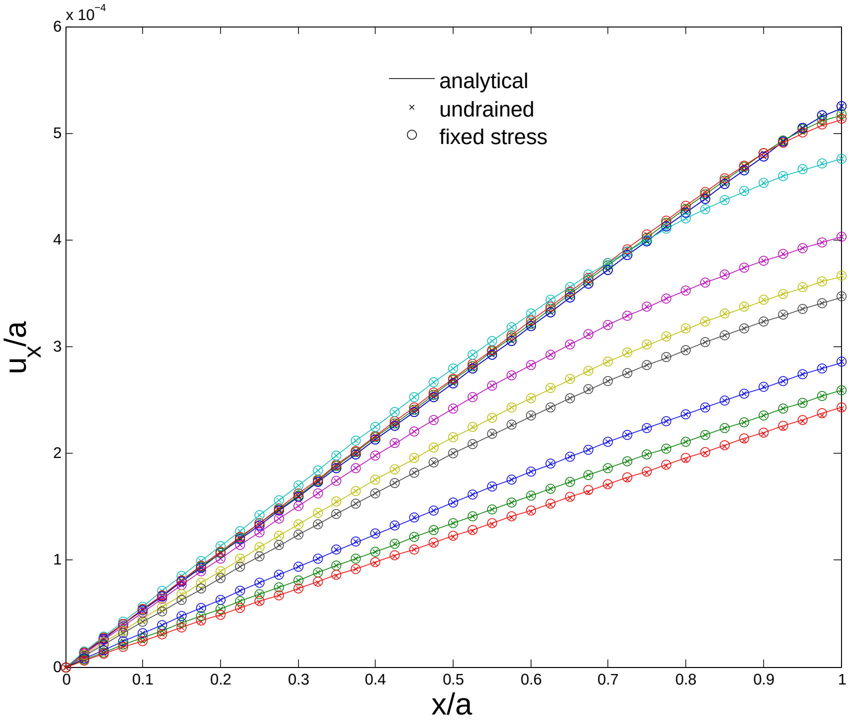

Figure 2.4: X-displacement matching result for Mandel's problem

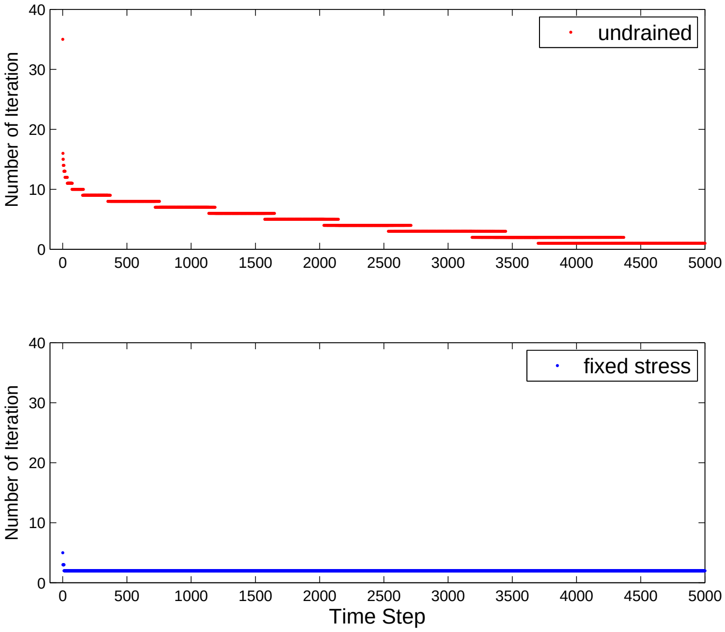

Figure 2.5: Comparison of number of iterations between undrained and fixed-stress schemes

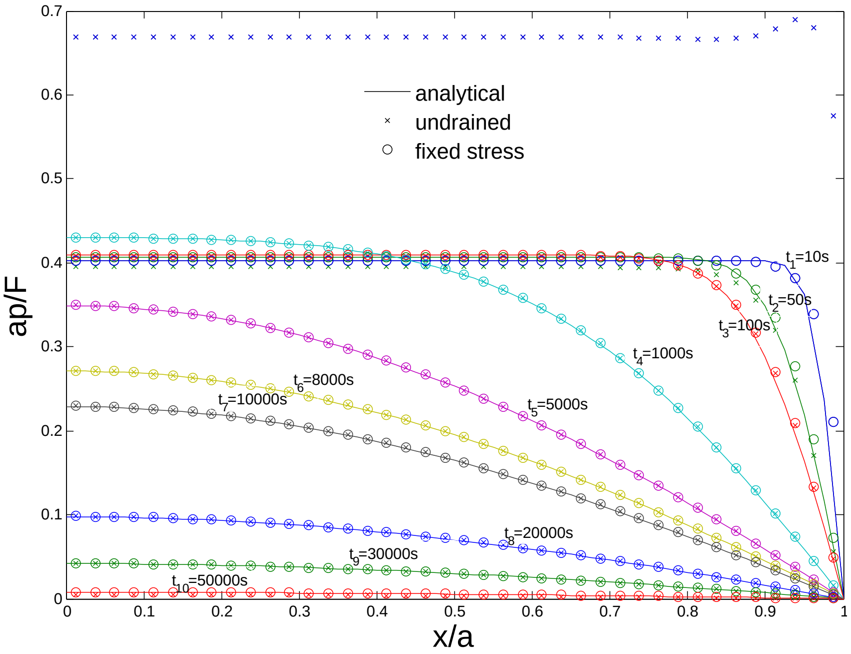

Figure 2.6: Pressure matching result for Mandel's problem (max number of iterations = 5)

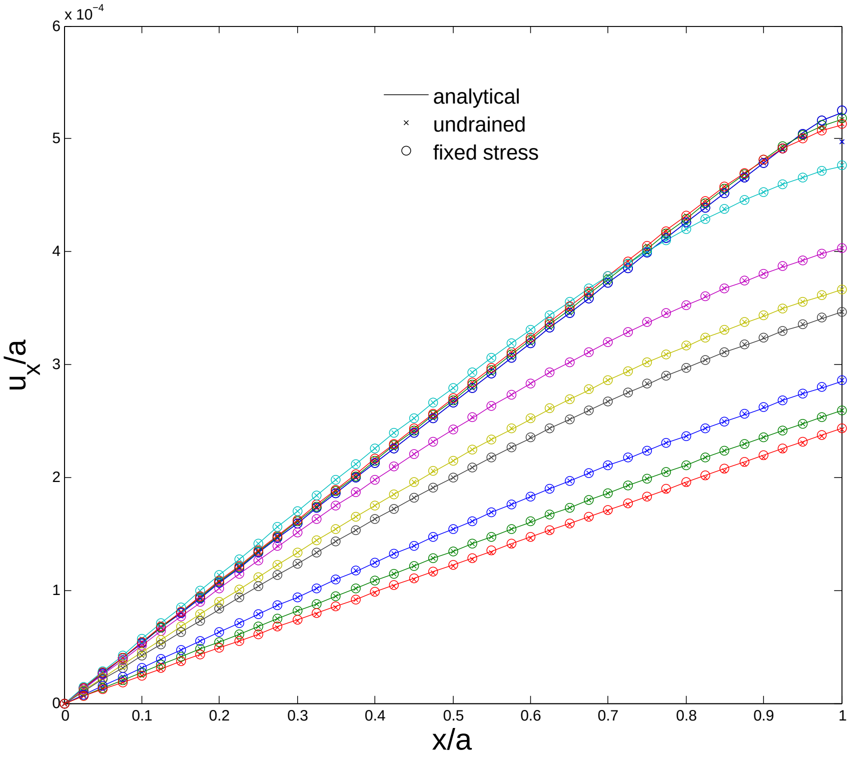

Figure 2.7: X-displacement matching result for Mandel's problem (max number of iterations = 5)

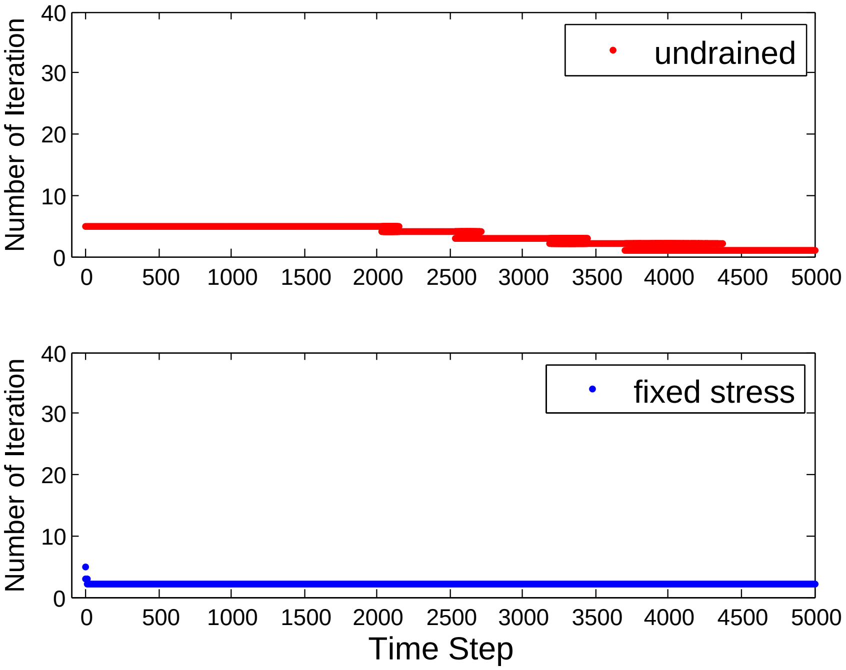

Figure 2.8: Comparison of number of iterations between undrained and fixed-stress schemes (max number of iterations = 5)

Chapter 3

Elasticity Model and Finite Element Formulation

3.1 Introduction

In this chapter, we present the mathematical description of the linear elasticity model and its finite element formulation. Since Biot [13, 14] first introduced his three-dimensional consolidation theory for poroelastic media, many simulators have been developed for coupling between elasticity model with single phase flow [79, 114, 115], multiphase flow [51, 78, 133], and more recently compositional flow [53, 97]. Some authors also consider thermal effects on the poroelasticity model, which is also called thermoporoelasticity coupling [40, 75, 79].

The finite element method was introduced in 1950's as a natural extension of matrix structural analysis. Over the years, it has gained popularity in solving partial differential equations especially in solid mechanics [34, 44, 63, 147]. Most of the existing poromechanics simulators, both from academia and industry, discretize the geomechanics model using the continuous Galerkin (CG) finite element method (FEM) where both test and trial functions defined on the finite element space are continuous functions

[36, 46, 51, 53, 75, 79, 97, 125, 131, 133]. In this work we couple CG for linear elasticity with MFE for compositional flow in Chapter 4 and with MFMFE for single and two-phase flow in Chapter 5. Phillips and Wheeler [102, 103] proved the convergence of CG and MFE coupling for the linear poroelasticity model; Wheeler et al. [144] proved the convergence of CG and MFMFE coupling for the same linear poroelasticity model.

3.2 Mathematical Model

The linear elasticity model used in the coupled poromechanics and/or thermoporomechanics model is derived using Newton's second law with the concept of effective stress [14, 121]. When Newton's second law is applied to the deformation of the solid matrix of porous media, the following assumptions are made [51, 79]:

1. The solid and fluid phase(s) are over-lapping materials, so the macroscopic continuous description of the fluid flow and the solid deformation applies.
2. The solid matrix deformation is assumed to be very small. This is a valid assumption for many problems of practical interests in reservoir engineering, civil engineering, and environmental engineering. As a result, Lagrangian and Eulerian descriptions of the strain tensor are identical. We adopt the Eulerian description of the strain tensor, the Cauchy strain tensor, in subsequent sections.

3. The velocity of the solid matrix is orders of magnitude slower compared to that of the fluid flow. Therefore, the acceleration term for the solid matrix in the force equilibrium equation can be neglected, which results in a simplified quasi-static force equilibrium equation balancing the internal force of the porous material and the external load exerted on it.
4. The isotropic linear elastic stress-strain constitutive equation is assumed. Two material constants, namely, Young's modulus E and Poisson's ratio ν, completely determine the stiffness tensor.
5. The shear stress exerted on the solid matrix by pore fluid pressure is neglected. In other words, pore fluid pressure only contributes to the normal component of the total stress tensor.
6. Temperature changes induce normal strain, and thermal strain is assumed to be linear isotropic, which means that the thermal strain tensor can be depicted with one constant thermal expansion coefficient.
7. No chemical reactions happen between the solid skeleton and the saturating fluids so the strength of the solid matrix does not change.

Consider a body of porous medium occupying a domain Ω in the three-dimensional space whose boundary $\partial\Omega = \Gamma$ can be decomposed into two parts:

$$\Gamma = \bar{\Gamma}_u \bigcup \bar{\Gamma}_t, \quad \Gamma_u \bigcap \Gamma_t = \emptyset, \quad \Gamma_u \neq \emptyset \tag{3.1}$$

The complementary boundaries Γ_u and Γ_t are Dirichlet and Neumann boundaries, respectively.

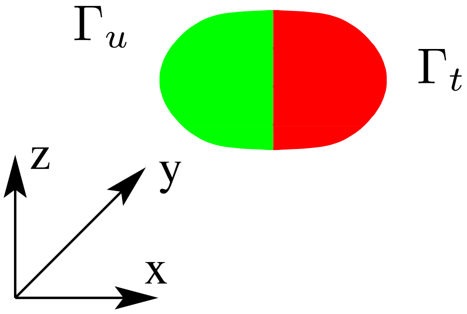

Figure 3.1: Dirichelet and Neumann boundaries for elasticity problem

In the domain Ω, the deformation of solid skeleton (solid matrix) of the porous medium is governed by:

Force Equilibrium Equation:

$$-\nabla \cdot \boldsymbol{\sigma} = \mathbf{f} \tag{3.2}$$

where $\boldsymbol{\sigma}$ is the total (Cauchy) stress tensor whose definition will be given later, and $\mathbf{f}$ is a vector consisting of the body force per unit volume of the solid skeleton and the saturating pore fluids. We should point out here that a consistent set of units is assumed for every equation presented in this dissertation, and we adopt the convention that tensile stresses and strains are positive.

Cauchy Strain Tensor:

$$\varepsilon_{ij} = \frac{1}{2}(\frac{\partial u_i}{\partial x_j} + \frac{\partial u_j}{\partial x_i}) \tag{3.3}$$

where ε_{ij} is Cauchy (total) strain tensor, and $\mathbf{u}$ is the displacement vector.

Hooke's Law:

$$\sigma^e_{ij} = \frac{E\nu}{(1+\nu)(1-2\nu)}\varepsilon^e_{kk}\delta_{ij} + \frac{E}{1+\nu}\varepsilon^e_{ij} \tag{3.4}$$

In equation 3.4, δ_{ij} is the Kronecker delta and the repeated subscript implies summation over the number of dimensions of the space. We adopt this Einstein notation for implied summation unless otherwise noted. ε^e_{ij} is the infinitestimal mechanical elastic strain tensor induced by the effective stress tensor σ^e_{ij} . $\varepsilon^e_v = \varepsilon^e_{kk} = \varepsilon^e_{11} + \varepsilon^e_{22} + \varepsilon^e_{33}$ is the mechanical volumetric strain. For general linear elastic materials, $\boldsymbol{\sigma}^e = \mathbf{C} : \boldsymbol{\varepsilon}^e$ where $\mathbf{C}$ is a fourth-order stiffness tensor with 21 independent components [63] and $\mathbf{A} : \mathbf{B} = A_{ij}B_{ij}$ represents the double-dot contraction operation between two tensors $\mathbf{A}$ and $\mathbf{B}$. With the isotropic material assumption, the elastic symmetries reduce the number of independent components of $\mathbf{C}$ to two. Equation 3.4 can also be expressed in terms of Lamé's parameters λ and G:

$$\sigma^e_{ij} = \lambda\varepsilon^e_{kk}\delta_{ij} + 2G\varepsilon^e_{ij} \tag{3.5}$$

with $\lambda = \frac{E\nu}{(1+\nu)(1-2\nu)}$, Lamé's first parameter, and $G = \frac{E}{2(1+\nu)}$, Lamé's second parameter or shear modulus.

Summation of equation 3.5 over the three normal components gives:

$$\sigma^e_v = \frac{(3\lambda + 2G)}{3}\varepsilon^e_{kk} \tag{3.6}$$

where $\sigma^e_v = 1/3(\sigma^e_{11} + \sigma^e_{22} + \sigma^e_{33})$ is the mean effective stress. Substituting equation 3.6 into 3.5 we get:

$$\varepsilon^e_{ij} = \frac{1}{2G}\sigma^e_{ij} - \frac{\lambda}{2G}\frac{3}{3\lambda + 2G}\sigma^e_v\delta_{ij} \tag{3.7}$$

In Chapter 4, we will consider the coupled thermoporoelasticity problem. When thermal effects are accounted, a temperature change will give rise to normal strains called the thermal strain [114, 115], denoted as ε_{ij}^T :

$$\varepsilon_{ii}^T = \alpha_{ii}^T (T - T_0) \tag{3.8}$$

Note that ε_{ii}^T denotes the normal component of ε_{ij}^T thus no summation is implied. T is the current temperature and T_0 is the reference temperature. α_{ii}^T is solid matrix thermal expansion coefficient for thermal strain component ε_{ii}^T. With the assumption that the thermal strain is linear isotropic, we have:

$$\varepsilon_{ii}^T = \alpha^T (T - T_0) \tag{3.9}$$

and α^T is a constant (which can vary spatially for heterogeneous porous media like E and ν, or λ and G) solid skeleton thermal expansion coefficient. The total strain tensor ε_{ij} given in equation 3.3 is defined as:

$$\varepsilon_{ij} = \varepsilon_{ij}^e + \varepsilon_{ij}^T \tag{3.10}$$

Therefore the total volumetric strain ε_v is:

$$\varepsilon_v = \varepsilon_v^e + 3\alpha^T (T - T_0) \tag{3.11}$$

Use equations 3.7, 3.9, 3.6, and 3.11 in equation 3.10, we obtain:

$$\begin{aligned}
\varepsilon_{ij} &= \varepsilon_{ij}^e + \varepsilon_{ij}^T \\
&= \frac{1}{2G}\sigma_{ij}^e - \frac{\lambda}{2G}\frac{3}{3\lambda + 2G}\sigma_v^e \delta_{ij} + \alpha^T (T - T_0)\delta_{ij} \\
&= \frac{1}{2G}\sigma_{ij}^e - \frac{\lambda}{2G}\varepsilon_v^e \delta_{ij} + \alpha^T (T - T_0)\delta_{ij} \\
&= \frac{1}{2G}\sigma_{ij}^e - \frac{\lambda}{2G}\left(\varepsilon_v - 3\alpha^T (T - T_0)\right) + \alpha^T (T - T_0)\delta_{ij}
\end{aligned} \tag{3.12}$$

Equation 3.12 gives the relation among the effective stress tensor σ_{ij}^e, the total strain tensor ε_{ij}, and the thermal strain tensor ε_{ij}^T as:

$$\sigma_{ij}^e = \lambda\varepsilon_v\delta_{ij} + 2G\varepsilon_{ij} - (3\lambda + 2G)\alpha^T(T - T_0)\delta_{ij} \tag{3.13}$$

In the coupled flow and geomechanics model, the total stress tensor σ_{ij} in equation 3.2 consists of effective stress (which induces the mechanical strain ε_{ij}^e) and pore pressure normal stress [14, 121], which is:

Total Stress Tensor

$$\sigma_{ij} = \sigma_{ij}^0 + \underbrace{\lambda\varepsilon_v\delta_{ij} + 2G\varepsilon_{ij} - (3\lambda + 2G)\alpha^T(T - T_0)\delta_{ij}}_{\text{effective stress}} - \alpha(p - p_0)\delta_{ij} \tag{3.14}$$

σ_{ij}^0 is the initial (in-situ) stress in the solid matrix of the porous media. The deformation of the solid skeleton of the porous media is thus coupled to the thermal energy balance equation through the term T and to the fluid flow equation through the term p. For single phase flow, p is pore fluid pressure, whereas for multiphase flow, p can be the pressure of a reference phase (usually the wetting phase) or a saturation weighted pressure. It is clear from equation 3.14 that the fluid flow in the pore space induces the deformation of the solid matrix through changing the effective stress state. It should be pointed out that since we solve the flow, geomechanics, and thermal energy balance equations in sequence, T and p are known quantities when we solve the equation 3.2 and they are treated as external loads and moved to the right-hand side (RHS) of equation 3.2.

The mathematical model of the quasi-static linear elastic force equilibrium equation is completed with the initial and boundary conditions.

Initial Condition:

$$\boldsymbol{\sigma}|_{t=0} = \boldsymbol{\sigma}_0 \tag{3.15}$$

Boundary Condition:

$$\mathbf{u} = \mathbf{u}_D \quad \text{on} \quad \Gamma_u; \quad \boldsymbol{\sigma}\mathbf{n} = \boldsymbol{\tau} \quad \text{on} \quad \Gamma_t. \tag{3.16}$$

where $\mathbf{u}_D$ is the prescribed displacement boundary condition, $\boldsymbol{\tau}$ is the prescribed traction boundary condition, and $\mathbf{n}$ is the unit outward normal vector of Γ_t.

3.3 Finite Element Formulation

By substituting equations 3.14 and 3.3 into 3.2, the equilibrium equation 3.2 can be formulated using displacement $\mathbf{u}$ as the primary unknown. More specifically, equation 3.2 becomes:

$$-\nabla \cdot \boldsymbol{\sigma}(\mathbf{u}) = \mathbf{f} \tag{3.17}$$

In this section, we will follow the standard finite element procedure [50, 63, 99] to discretize the quasi-static equilibrium equation 3.17.

3.3.1 Galerkin Weak Formulation

Multiplying equation 3.17 with an arbitrary vector-valued function $\mathbf{a}$ and integrating over the domain Ω, we have:

$$-\int_{\Omega} \mathbf{a} \cdot (\nabla \cdot \boldsymbol{\sigma}) d\Omega = \int_{\Omega} \mathbf{f} \cdot \mathbf{a} d\Omega \tag{3.18}$$

Use the identity equation

$$\nabla \cdot (\boldsymbol{\sigma}\mathbf{a}) = \mathbf{a} \cdot (\nabla \cdot \boldsymbol{\sigma}) + \nabla \mathbf{a} : \boldsymbol{\sigma} \tag{3.19}$$

and the divergence theorem (also note that $\boldsymbol{\sigma}$ is a symmetric tensor)

$$\begin{aligned} \int_{\Omega} \nabla \cdot (\boldsymbol{\sigma}\mathbf{a}) d\Omega &= \int_{\Omega} \nabla \cdot (\mathbf{a}\boldsymbol{\sigma}) d\Omega \\ &= \int_{\Gamma} \mathbf{a} \cdot (\boldsymbol{\sigma}\mathbf{n}) d\Gamma \end{aligned} \tag{3.20}$$

equation 3.18 becomes

$$\int_{\Omega} \nabla \mathbf{a} : \boldsymbol{\sigma} d\Omega = \int_{\Omega} \mathbf{f} \cdot \mathbf{a} d\Omega + \int_{\Gamma_t} \mathbf{a} \cdot \boldsymbol{\tau} d\Gamma \tag{3.21}$$

In the derivation of equation 3.21 we use the Neumann boundary condition in equation 3.16 and assume that $\mathbf{a} = 0$ on Γ_u.

We further notice that the contraction of a skew-symmetric tensor and a symmetric tensor is always zero, therefore

$$\begin{aligned} \int_{\Omega} \nabla \mathbf{a} : \boldsymbol{\sigma}(\mathbf{u}) d\Omega &= \int_{\Omega} \frac{1}{2} \left(\nabla \mathbf{a} + (\nabla \mathbf{a})^T\right) : \boldsymbol{\sigma}(\mathbf{u}) + \frac{1}{2} \left(\nabla \mathbf{a} - (\nabla \mathbf{a})^T\right) : \boldsymbol{\sigma}(\mathbf{u}) d\Omega \\ &= \int_{\Omega} \frac{1}{2} \left(\nabla \mathbf{a} + (\nabla \mathbf{a})^T\right) : \boldsymbol{\sigma}(\mathbf{u}) d\Omega \\ &= \int_{\Omega} \boldsymbol{\varepsilon}(\mathbf{a}) : \boldsymbol{\sigma}(\mathbf{u}) d\Omega \end{aligned} \tag{3.22}$$

where $(\cdot)^T$ is the transpose of a tensor.

The Galerkin weak formulation of equation 3.17 then reads:
Find $\mathbf{u} \in U$, such that for $\forall \mathbf{a} \in V$

$$\int_\Omega \boldsymbol{\varepsilon}(\mathbf{a}) : \boldsymbol{\sigma}(\mathbf{u}) d\Omega = \int_\Omega \mathbf{f} \cdot \mathbf{a} d\Omega + \int_{\Gamma_t} \mathbf{a} \cdot \boldsymbol{\tau} d\Gamma \tag{3.23}$$

where U is the trial space and V is the test space:

$$U := \{\mathbf{u} \in H^1(\Omega) \quad | \quad \mathbf{u} = \mathbf{u}_D \quad \text{on} \quad \Gamma_u\} \tag{3.24}$$

$$V := \{\mathbf{a} \in H^1(\Omega) \quad | \quad \mathbf{a} = 0 \quad \text{on} \quad \Gamma_u\} \tag{3.25}$$

and $H^1(\Omega)$ is Hilbert space on Ω:

$$H^1(\Omega) := \{\frac{\partial \mathbf{a}}{\partial x_i} \in L^2(\Omega)^3\} \tag{3.26}$$

Equation 3.23 essentially states the principle of virtual work: for a body originally in equilibrium, the work done by external forces over a virtual displacement $\mathbf{a}$ (the RHS of equation 3.28) is balanced by the work done by internal stress over the virtual strain $\boldsymbol{\varepsilon}(\mathbf{a})$ induced by the virtual displacement $\mathbf{a}$ (the left-hand side of equation 3.23).

3.3.2 Galerkin Approximation Formulation

The trial space U and the test space V are infinite dimensional function spaces. In order to find a numerical (approximate) solution to equation 3.17 with the boundary conditions 3.16, we need to define a finite dimensional space where the approximate solution $\mathbf{u}_h$ lives in. Let $\mathcal{T}_h$ be a finite element partition of the domain Ω consisting of hexahedrons Ω_i^E , such that:

$$\mathcal{T}_h := \bigcup_i \Omega_i^E \approx \Omega \tag{3.27}$$

where $h = \max_i \operatorname{diam}(\Omega_i^E)$ [64].

The Galerkin approximation formulation of equation 3.23 is defined as: Find $\mathbf{u}_h \in U_h$, such that for $\forall \mathbf{a}_h \in V_h$

$$\int_{\mathcal{T}_h} \boldsymbol{\varepsilon}(\mathbf{a}_h) : \boldsymbol{\sigma}(\mathbf{u}_h) d\mathcal{T}_h = \int_{\mathcal{T}_h} \mathbf{f} \cdot \mathbf{a}_h d\mathcal{T}_h + \int_{\bar{\Gamma}_t} \mathbf{a}_h \cdot \boldsymbol{\tau}_h d\bar{\Gamma} \tag{3.28}$$

where $\mathbf{a}_h$ is the test function on the finite element space V_h, $\bar{\Gamma}_t$ is Neumann boundary of $\mathcal{T}_h$, $\boldsymbol{\tau}_h$ is the approximate Neumann boundary condition on $\bar{\Gamma}_t$, U_h is the trial function space and V_h is the test function space on $\mathcal{T}_h$, respectively.

$$U_h \quad := \quad \{\mathbf{u}_h \in H^1(\mathcal{T}_h) \quad | \quad \mathbf{u}_h = \bar{\mathbf{u}}_D \quad \text{on} \quad \bar{\Gamma}_u\} \tag{3.29}$$

$$V_h \quad := \quad \{\mathbf{a}_h \in H^1(\mathcal{T}_h) \quad | \quad \mathbf{a}_h = 0 \quad \text{on} \quad \bar{\Gamma}_u\} \tag{3.30}$$

Likewise, $\bar{\Gamma}_u$ is Dirichlet boundary of $\mathcal{T}_h$ and $\bar{\mathbf{u}}_D$ is the approximate Dirichlet boundary condition prescribed on $\bar{\Gamma}_u$.

3.3.3 Finite Element Integration

Since U_h and V_h are finite dimensional, any function in U_h (or V_h) can be represented using a complete set of basis functions in U_h (or V_h). For example,

$$\mathbf{u}_h = \sum_{i=1}^{nnode} \mathbf{u}_i \psi_i + \sum_{j=1}^{ndbc} \mathbf{u}_D^j \psi_D^j \tag{3.31}$$

The degrees of freedom $\mathbf{u}_i, \quad i = 1, 2, \cdots, nnode$ and the basis functions $\psi_i, \quad i = 1, 2, \cdots, nnode$ are associated with vertices i of finite elements in $\mathcal{T}_h$ whose location vector is denoted as $\mathbf{r}_i$. Note that $nnode$ is the total number of vertices in $\mathcal{T}_h \backslash \bar{\Gamma}_D$, whereas $ndbc$ is the total number of vertices on $\bar{\Gamma}_D$ and $\mathbf{u}_D^j$ is prescribed Dirichlet boundary condition. ψ_D^j is basis function associated with vertex on Dirichlet boundary $\bar{\Gamma}_D$. It is clear from equation 3.31 that

$$V_h = U_h \backslash \mathrm{span}(\psi_D^j, \quad j = 1, 2, \cdots, ndbc) \tag{3.32}$$

We choose U_h and V_h to be piecewise tri-linear function space in R^3 and the basis function satisfies:

$$\psi_i(\mathbf{r}_j) = \delta_{ij} \tag{3.33}$$

We should point out that in practical implementation of the finite element method for equation 3.23, usually ψ_D^j is also used as basis function for test function $\mathbf{a}_h$. After assembling the global stiffness matrix $\mathbf{K}^G$, the three rows of coefficients in K^G resulted from testing equation 3.23 with ψ_D^j are modified with unity in the diagonal and zero in the off-diagonal terms to make $\mathbf{K}^G$ a positive-definite matrix. Terms in $\mathbf{K}^G$ related to the interactions between $\mathbf{u}_D^j \psi_D^j$ and ψ_i are moved to the RHS of the global linear system because $\mathbf{u}_D^j$ are known boundary conditions. Therefore, in integrating the equation 3.23, the test function space V_h is first set to U_h, and then $\mathbf{K}_G$ and RHS of the global linear system are modified to enforce Dirichlet boundary conditions and eliminate extra equations resulted from ψ_D^j being used as bases for test function $\mathbf{a}_h$.

In the finite element implementation, the integration of equation 3.23 over $\mathcal{T}_h$ is divided into integrations over its elements Ω_i^E, namely:

$$\int_{\mathcal{T}_h} \boldsymbol{\varepsilon}(\mathbf{a}_h) : \boldsymbol{\sigma}(\mathbf{u}_h) d\mathcal{T}_h = \int_{\mathcal{T}_h} \mathbf{f} \cdot \mathbf{a}_h d\mathcal{T}_h + \int_{\bar{\Gamma}_t} \mathbf{a}_h \cdot \boldsymbol{\tau}_h d\bar{\Gamma} \Longrightarrow$$
$$\sum_i \left(\int_{\Omega_i^E} \boldsymbol{\varepsilon}(\mathbf{a}_h) : \boldsymbol{\sigma}(\mathbf{u}_h) d\Omega_i^E \right) = \sum_i \left(\int_{\Omega_i^E} \mathbf{f} \cdot \mathbf{a}_h d\Omega_i^E \right)$$
$$+ \sum_i \left(\int_{\partial\Omega_i^E \bigcap \bar{\Gamma}_t} \mathbf{a}_h \cdot \boldsymbol{\tau}_h d\partial\Omega_i^E + \int_{\partial\Omega_i^E \backslash \bar{\Gamma}_t} \mathbf{a}_h \cdot (\boldsymbol{\sigma}\mathbf{n}) d\partial\Omega_i^E \right) \tag{3.34}$$

Since U_h and V_h are continuous function spaces, the third term in the RHS of equation 3.34 vanishes when summed over $\mathcal{T}_h$:

$$\sum_i \big(\int_{\partial\Omega_i^E \backslash \bar{\Gamma}_t} \mathbf{a}_h \cdot (\boldsymbol{\sigma}\mathbf{n}) d\partial\Omega_i^E \big) = 0 \tag{3.35}$$

therefore we omit it when performing element integration in equation 3.34.

We use 8-node hexahedrons in R^3 to partition the domain Ω. This choice is consistent with the finite element partitions adopted by the flow models to which the geomechanics model is coupled. More specifically, the MFE compositional flow model uses 8-node rectangular finite elements and the MFMFE flow models use 8-node general hexahedral finite elements. The U_h and V_h used here are piecewise tri-linear function spaces. The integration of equation 3.34 is performed over a reference element $\Omega^{\hat{E}}$ which is a unit cube in the reference coordinate (ξ, η, ζ). The isoparametric finite element mapping $F_E : \quad \hat{\mathbf{r}} \longmapsto \mathbf{r}$ is defined as:

$$\mathbf{r} = \sum_{i=1}^{8} \hat{N}_i(\hat{\mathbf{r}}) \mathbf{r}_i^j \tag{3.36}$$

where $\hat{\mathbf{r}} = (\xi, \eta, \zeta)^T$ is the location vector in the reference space with $\hat{\mathbf{r}} \in [0,1]^3$, $\mathbf{r}_i^j$ is the location vector of vertex i of the finite element Ω_j^E, $\hat{N}_i$ is the shape function associated with vertex i in the reference cube whose definition is given in equation 3.37. For the simplicity of representation, we drop the superscript j in the following development, implying that the mapping is between the reference cube and a current finite element Ω_j^E in $\mathcal{T}_h$. Figure 3.2 illustrates the mapping F_E from a unit cube in (ξ, η, ζ) coordinate to the finite element Ω_j^E in (x, y, z) coordinate.

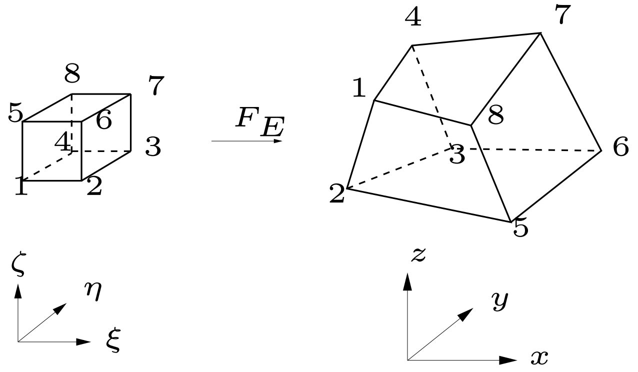

Figure 3.2: Finite element mapping between reference space and physical space

$$\begin{aligned}
\hat{N}_1 &= (1-\xi)(1-\eta)(1-\zeta) \\
\hat{N}_2 &= \xi(1-\eta)(1-\zeta) \\
\hat{N}_3 &= \xi\eta(1-\zeta) \\
\hat{N}_4 &= (1-\xi)\eta(1-\zeta) \\
\hat{N}_5 &= (1-\xi)(1-\eta)\zeta \\
\hat{N}_6 &= \xi(1-\eta)\zeta \\
\hat{N}_7 &= \xi\eta\zeta \\
\hat{N}_8 &= (1-\xi)\eta\zeta \qquad (3.37)
\end{aligned}$$

Note that $\hat{N}_i$ is tri-linear within $\Omega^{\hat{E}}$ and $\hat{N}_i(\hat{\mathbf{r}}_j) = \delta_{ij}$ where $\hat{\mathbf{r}}_j$ is the location vector of vertex j of the reference cube $\Omega^{\hat{E}}$. The Jacobian matrix DF_E of the mapping F_E is defined as:

$$DF_E(\hat{\mathbf{r}}) = \begin{pmatrix} \frac{\partial x}{\partial \xi} & \frac{\partial x}{\partial \eta} & \frac{\partial x}{\partial \zeta} \\ \frac{\partial y}{\partial \xi} & \frac{\partial y}{\partial \eta} & \frac{\partial y}{\partial \zeta} \\ \frac{\partial z}{\partial \xi} & \frac{\partial z}{\partial \eta} & \frac{\partial z}{\partial \zeta} \end{pmatrix} \qquad (3.38)$$

and its determinant is denoted by $J_E = \det(DF_E)$.

Since F_E is isoparametric mapping, within a finite element Ω^E in $\mathcal{T}_h$, $\mathbf{u}_h$ and $\mathbf{a}_h$ can be represented as follows:

$$\mathbf{u}_h(\hat{\mathbf{r}}) = \sum_{j=1}^{8} \hat{N}_j(\hat{\mathbf{r}})\mathbf{u}_j \qquad (3.39)$$

$$\mathbf{a}_h(\hat{\mathbf{r}}) = \sum_{j=1}^{8} \hat{N}_j(\hat{\mathbf{r}})\mathbf{a}_j \qquad (3.40)$$

Equations 3.39 and 3.40 can be written in vector form:

$$\begin{aligned}\mathbf{u}_h &= \left(\hat{N}_1\mathbf{I} \quad \hat{N}_2\mathbf{I} \quad \cdots \quad \hat{N}_8\mathbf{I} \right) \left(\mathbf{u}_1 \quad \mathbf{u}_2 \quad \cdots \quad \mathbf{u}_8 \right)^T \\ &= \mathcal{N}\bar{\mathbf{u}} \qquad (3.41)\\ \mathbf{a}_h &= \left(\hat{N}_1\mathbf{I} \quad \hat{N}_2\mathbf{I} \quad \cdots \quad \hat{N}_8\mathbf{I} \right) \left(\mathbf{a}_1 \quad \mathbf{a}_2 \quad \cdots \quad \mathbf{a}_8 \right)^T \\ &= \mathcal{N}\bar{\mathbf{a}} \qquad (3.42)\end{aligned}$$

$\mathbf{I}$ is the second-order identity tensor in R^3, $\mathcal{N}$ is the 3×24 interpolation matrix consisting of 8 3×3 blocks, $\bar{\mathbf{u}}$ is a 24×1 vector consisting of 8 3-component nodal displacements (displacement degree of freedom or Dirichlet boundary data), and $\bar{\mathbf{a}}$ is a 24×1 vector consisting of 8 3-component nodal values of the test function. With equations 3.41, 3.42, the definition of Cauchy strain tensor 3.3, the linear elastic stress-strain constitutive equation 3.5, and adopting Voigt notation [63], the total strain tensor $\varepsilon_i j$ and the associated stress tensor $\sigma_i^{e+T} j$ (including effective stress and thermal stress) can also be represented in vector form:

$$\begin{aligned}\boldsymbol{\varepsilon}(\hat{\mathbf{r}}) &= \mathcal{B}(\hat{\mathbf{r}})\bar{\mathbf{u}} \qquad (3.43)\\ \boldsymbol{\sigma}^{e+T}(\hat{\mathbf{r}}) &= \mathcal{D}^e\boldsymbol{\varepsilon}(\hat{\mathbf{r}}) = \mathcal{D}^e\mathcal{B}(\hat{\mathbf{r}})\bar{\mathbf{u}} \qquad (3.44)\end{aligned}$$

Note that $\boldsymbol{\varepsilon}$ denotes both tensor and vector forms of Cauchy strain tensor, and $\boldsymbol{\sigma}^{e+T}$ denotes both tensor and vector forms of the associated stress tensor. The vector forms of $\boldsymbol{\varepsilon}$ and $\boldsymbol{\sigma}^{e+T}$, the strain interpolation matrix $\mathcal{B}$, and the elastic constitutive matrix $\mathcal{D}^e$ are given as follows:

$$\boldsymbol{\varepsilon} = \begin{pmatrix} \varepsilon_{11} \\ \varepsilon_{22} \\ \varepsilon_{33} \\ \gamma_{12} \\ \gamma_{23} \\ \gamma_{13} \end{pmatrix} = \begin{pmatrix} \varepsilon_{11} \\ \varepsilon_{22} \\ \varepsilon_{33} \\ 2\varepsilon_{12} \\ 2\varepsilon_{23} \\ 2\varepsilon_{13} \end{pmatrix} \tag{3.45}$$

where $\gamma_{ij}, \quad i \neq j$ is engineering shear strain.

$$\boldsymbol{\sigma}^{e+T} = \begin{pmatrix} \sigma_{11}^{e+T} \\ \sigma_{22}^{e+T} \\ \sigma_{33}^{e+T} \\ \sigma_{12}^{e+T} \\ \sigma_{23}^{e+T} \\ \sigma_{13}^{e+T} \end{pmatrix} \tag{3.46}$$

$$\mathcal{B}(\hat{\mathbf{r}}) = \begin{pmatrix} \mathbf{B}_1(\hat{\mathbf{r}}) & \mathbf{B}_2(\hat{\mathbf{r}}) & \cdots & \mathbf{B}_8(\hat{\mathbf{r}}) \end{pmatrix} \tag{3.47}$$

and $\mathbf{B}_j$ is a 6×3 strain interpolation matrix associated with vertex j in a finite element Ω_i^E.

$$\mathbf{B}_j(\hat{\mathbf{r}}) = \begin{pmatrix} \frac{\partial \hat{N}_j(\hat{\mathbf{r}})}{\partial x} & 0 & \\ 0 & \frac{\partial \hat{N}_j(\hat{\mathbf{r}})}{\partial y} & 0 \\ 0 & 0 & \frac{\partial \hat{N}_j(\hat{\mathbf{r}})}{\partial z} \\ \frac{\partial \hat{N}_j(\hat{\mathbf{r}})}{\partial y} & \frac{\partial \hat{N}_j(\hat{\mathbf{r}})}{\partial x} & 0 \\ 0 & \frac{\partial \hat{N}_j(\hat{\mathbf{r}})}{\partial z} & \frac{\partial \hat{N}_j(\hat{\mathbf{r}})}{\partial y} \\ \frac{\partial \hat{N}_j(\hat{\mathbf{r}})}{\partial z} & 0 & \frac{\partial \hat{N}_j(\hat{\mathbf{r}})}{\partial x} \end{pmatrix} \tag{3.48}$$

$$\mathcal{D}^e = \begin{pmatrix} \lambda + 2\mu & \lambda & \lambda & 0 & 0 & 0 \\ \lambda & \lambda + 2\mu & \lambda & 0 & 0 & 0 \\ \lambda & \lambda & \lambda + 2\mu & 0 & 0 & 0 \\ 0 & 0 & 0 & \mu & 0 & 0 \\ 0 & 0 & 0 & 0 & \mu & 0 \\ 0 & 0 & 0 & 0 & 0 & \mu \end{pmatrix} \tag{3.49}$$

The vector form of total stress σ_{ij} in equation 3.14 reads:

$$\begin{aligned}\boldsymbol{\sigma}(\hat{\mathbf{r}}) &= \boldsymbol{\sigma}_0 + \boldsymbol{\sigma}^{e+T}(\hat{\mathbf{r}}) - (3\lambda + 2\mu)\alpha^T(T - T_0)\mathbf{I} - \alpha(p - p_0)\mathbf{I} \\ &= \boldsymbol{\sigma}_0 + \mathcal{D}^e\mathcal{B}(\hat{\mathbf{r}})\bar{\mathbf{u}} - (3\lambda + 2\mu)\alpha^T(T - T_0)\mathbf{I} - \alpha(p - p_0)\mathbf{I} \qquad (3.50)\end{aligned}$$

$\mathbf{I}$ in equation 3.50 denotes the vector form of the second-order identity tensor:

$$\mathbf{I} = \begin{pmatrix} 1 \\ 1 \\ 1 \\ 0 \\ 0 \\ 0 \end{pmatrix} \qquad (3.51)$$

Note that in the calculation of $\mathbf{B}_i$ in equation 3.48, $\frac{\partial \hat{N}_i(\hat{\mathbf{r}})}{\partial x_j}$ is required. Using the chain rule,

$$\begin{aligned}\frac{\partial \hat{N}_i}{\partial \xi} &= \frac{\partial \hat{N}_i}{\partial x}\frac{\partial x}{\partial \xi} + \frac{\partial \hat{N}_i}{\partial y}\frac{\partial y}{\partial \xi} + \frac{\partial \hat{N}_i}{\partial z}\frac{\partial z}{\partial \xi} \\ \frac{\partial \hat{N}_i}{\partial \eta} &= \frac{\partial \hat{N}_i}{\partial x}\frac{\partial x}{\partial \eta} + \frac{\partial \hat{N}_i}{\partial y}\frac{\partial y}{\partial \eta} + \frac{\partial \hat{N}_i}{\partial z}\frac{\partial z}{\partial \eta} \\ \frac{\partial \hat{N}_i}{\partial \zeta} &= \frac{\partial \hat{N}_i}{\partial x}\frac{\partial x}{\partial \zeta} + \frac{\partial \hat{N}_i}{\partial y}\frac{\partial y}{\partial \zeta} + \frac{\partial \hat{N}_i}{\partial z}\frac{\partial z}{\partial \zeta} \qquad (3.52)\end{aligned}$$

Write equation 3.52 in matrix form

$$\begin{pmatrix} \frac{\partial \hat{N}_i}{\partial \xi} \\ \frac{\partial \hat{N}_i}{\partial \eta} \\ \frac{\partial \hat{N}_i}{\partial \zeta} \end{pmatrix} = \begin{pmatrix} \frac{\partial x}{\partial \xi} & \frac{\partial y}{\partial \xi} & \frac{\partial z}{\partial \xi} \\ \frac{\partial x}{\partial \eta} & \frac{\partial y}{\partial \eta} & \frac{\partial z}{\partial \eta} \\ \frac{\partial x}{\partial \zeta} & \frac{\partial y}{\partial \zeta} & \frac{\partial z}{\partial \zeta} \end{pmatrix} \begin{pmatrix} \frac{\partial \hat{N}_i}{\partial x} \\ \frac{\partial \hat{N}_i}{\partial y} \\ \frac{\partial \hat{N}_i}{\partial z} \end{pmatrix} \qquad (3.53)$$

or

$$\begin{pmatrix} \frac{\partial \hat{N}_i}{\partial \xi} \\ \frac{\partial \hat{N}_i}{\partial \eta} \\ \frac{\partial \hat{N}_i}{\partial \zeta} \end{pmatrix} = DF_E^T \begin{pmatrix} \frac{\partial \hat{N}_i}{\partial x} \\ \frac{\partial \hat{N}_i}{\partial y} \\ \frac{\partial \hat{N}_i}{\partial z} \end{pmatrix} \qquad (3.54)$$

Therefore

$$\begin{pmatrix} \frac{\partial \hat{N}_i}{\partial x} \\ \frac{\partial \hat{N}_i}{\partial y} \\ \frac{\partial \hat{N}_i}{\partial z} \end{pmatrix} = (DF_E^T)^{-1} \begin{pmatrix} \frac{\partial \hat{N}_i}{\partial \xi} \\ \frac{\partial \hat{N}_i}{\partial \eta} \\ \frac{\partial \hat{N}_i}{\partial \zeta} \end{pmatrix} \tag{3.55}$$

And $\mathbf{B}_i$ can be explicitly expressed and calculated as $\mathbf{B}_i(\hat{\mathbf{r}})$.

Substituting equations 3.41, 3.42, 3.43, 3.44, 3.47, 3.49, 3.50 into 3.34 to integrate over the reference unit cube $\Omega^{\hat{E}}$, and after some manipulations, we have:

$$\begin{aligned}
&\bar{\mathbf{a}}^T \left(\int_{\Omega^{\hat{E}}} \mathcal{B}^T \mathcal{D}^e \mathcal{B} J_E d\Omega^{\hat{E}} \right) \bar{\mathbf{u}} = \bar{\mathbf{a}}^T \int_{\Omega^{\hat{E}}} \mathcal{N}^T \mathbf{f} J_E d\Omega^{\hat{E}} \\
&+\bar{\mathbf{a}}^T \int_{\Omega^{\hat{E}}} \big((3\lambda + 2G)\alpha^T (T - T_0) + \alpha(p - p_0)\big) \mathcal{B}^T \mathbf{I} J_E d\Omega^{\hat{E}} \\
&-\bar{\mathbf{a}}^T \int_{\Omega^{\hat{E}}} \mathcal{B}^T \boldsymbol{\sigma}_0 J_E d\Omega^{\hat{E}} \\
&+\bar{\mathbf{a}}^T \int_{\partial\Omega^{\hat{E}} \bigcap DF_E^{-1}(\bar{\Gamma}_t)} \mathcal{N}^T \boldsymbol{\tau}_h J_e d\partial\Omega^{\hat{E}}
\end{aligned} \tag{3.56}$$

It should be pointed out that for the last term in the RHS of equation 3.56, J_e is the determinant of Jacobian of a finite element mapping from a boundary face of $\Omega^{\hat{E}}$ to a boundary face of Ω^E in $\mathcal{T}_h$.

Since the test function $\mathbf{a}_h$ is arbitrary, $\bar{\mathbf{a}}^T$ is arbitrary, which means

$$\begin{aligned}
&\left(\int_{\Omega^{\hat{E}}} \mathcal{B}^T \mathcal{D}^e \mathcal{B} J_E d\Omega^{\hat{E}} \right) \bar{\mathbf{u}} = \int_{\Omega^{\hat{E}}} \mathcal{N}^T \mathbf{f} J_E d\Omega^{\hat{E}} \\
&+ \int_{\Omega^{\hat{E}}} \big((3\lambda + 2G)\alpha^T (T - T_0) + \alpha(p - p_0)\big) \mathcal{B}^T \mathbf{I} J_E d\Omega^{\hat{E}} \\
&- \int_{\Omega^{\hat{E}}} \mathcal{B}^T \boldsymbol{\sigma}_0 J_E d\Omega^{\hat{E}} \\
&+ \int_{\partial\Omega^{\hat{E}} \bigcap DF_E^{-1}(\bar{\Gamma}_t)} \mathcal{N}^T \boldsymbol{\tau}_h J_e d\partial\Omega^{\hat{E}}
\end{aligned} \tag{3.57}$$

always holds.

The volume and face integrations in equation 3.57 are approximated using Gaussian quadrature rule, namely

$$\int_{\Omega^{\hat{E}}} F(\bar{\mathbf{r}}) d\Omega^{\hat{E}} \approx \sum_{i=1}^{vqpt} w_i^v F(\bar{\mathbf{r}}_i^v) \tag{3.58}$$

$$\int_{\partial\Omega^{\hat{E}}} F(\bar{\mathbf{r}}) d\partial\Omega^{\hat{E}} \approx \sum_{i=1}^{fqpt} w_i^f F(\bar{\mathbf{r}}_i^f) \tag{3.59}$$

where $vgpt$ is the total number of Gaussian quadrature points for volume integration and $fgpt$ is the total number of Gaussian quadrature points for face integration. $\bar{\mathbf{r}}_i^v$ is the location vector in $\Omega^{\bar{E}}$ for Gaussian point i for volume integration, w_i^v is the associated weight; $\bar{\mathbf{r}}_i^f$ is the location vector in $\Omega^{\bar{E}}$ for Gaussian point i for face integration, w_i^f is the associated weight. We use the tensor product of a one-dimensional two-point Gaussian quadrature rule for the two-dimensional and the three-dimensional integration. For example, in the three-dimensional case,

$$\begin{aligned}
\bar{\mathbf{r}}_1^v &= \left(\frac{1}{2}\left(1-\frac{\sqrt{3}}{3}\right),\frac{1}{2}\left(1-\frac{\sqrt{3}}{3}\right),\frac{1}{2}\left(1-\frac{\sqrt{3}}{3}\right)\right)^T \\
\bar{\mathbf{r}}_2^v &= \left(\frac{1}{2}\left(1+\frac{\sqrt{3}}{3}\right),\frac{1}{2}\left(1-\frac{\sqrt{3}}{3}\right),\frac{1}{2}\left(1-\frac{\sqrt{3}}{3}\right)\right)^T \\
\bar{\mathbf{r}}_3^v &= \left(\frac{1}{2}\left(1+\frac{\sqrt{3}}{3}\right),\frac{1}{2}\left(1+\frac{\sqrt{3}}{3}\right),\frac{1}{2}\left(1-\frac{\sqrt{3}}{3}\right)\right)^T \\
\bar{\mathbf{r}}_4^v &= \left(\frac{1}{2}\left(1-\frac{\sqrt{3}}{3}\right),\frac{1}{2}\left(1+\frac{\sqrt{3}}{3}\right),\frac{1}{2}\left(1-\frac{\sqrt{3}}{3}\right)\right)^T \\
\bar{\mathbf{r}}_5^v &= \left(\frac{1}{2}\left(1-\frac{\sqrt{3}}{3}\right),\frac{1}{2}\left(1-\frac{\sqrt{3}}{3}\right),\frac{1}{2}\left(1+\frac{\sqrt{3}}{3}\right)\right)^T \\
\bar{\mathbf{r}}_6^v &= \left(\frac{1}{2}\left(1+\frac{\sqrt{3}}{3}\right),\frac{1}{2}\left(1-\frac{\sqrt{3}}{3}\right),\frac{1}{2}\left(1+\frac{\sqrt{3}}{3}\right)\right)^T \\
\bar{\mathbf{r}}_7^v &= \left(\frac{1}{2}\left(1+\frac{\sqrt{3}}{3}\right),\frac{1}{2}\left(1+\frac{\sqrt{3}}{3}\right),\frac{1}{2}\left(1+\frac{\sqrt{3}}{3}\right)\right)^T \\
\bar{\mathbf{r}}_8^v &= \left(\frac{1}{2}\left(1-\frac{\sqrt{3}}{3}\right),\frac{1}{2}\left(1+\frac{\sqrt{3}}{3}\right),\frac{1}{2}\left(1+\frac{\sqrt{3}}{3}\right)\right)^T \qquad (3.60)
\end{aligned}$$

with $w_i^v = \frac{1}{8}, \quad \text{for } i = 1, 8.$

After applying the Gaussian quadrature rule to equation 3.57, we obtain a local linear system for Ω^E in $\mathcal{T}_h$

$$\mathbf{K}^e \bar{\mathbf{u}} = \mathbf{f}^e \qquad (3.61)$$

with $\mathbf{K}^e$ a 24×24 local stiffness matrix and $\mathbf{f}^e$ a 24×1 local load vector which includes thermal stress and fluid pore pressure contributions. Summation of equation 3.57 over $\mathcal{T}_h$ gives rise to the global linear system for the linear elasticity equation:

$$\mathbf{K}^G \bar{\mathbf{u}}^G = \mathbf{F}^G \tag{3.62}$$

where $\bar{\mathbf{u}}^G$ is the global displacement degree of freedom vector and $\mathbf{F}^G$ is the global load vector. As mentioned before, $\mathbf{K}^G$ and $\mathbf{F}^G$ have to be modified to account for prescribed Dirichlet boundary conditions. The resulting global stiffness matrix $\mathbf{K}^G$ is symmetric positive definite (SPD). The global linear system 3.62 can be solved by different linear solvers.

Chapter 4

Geomechanics Coupled with Compositional Flow

4.1 Introduction

For many real world applications like CO_2 flooding as a means of enhanced oil recovery technique [30] or CO_2 injection into saline aquifers as a way of carbon sequestration [48, 76, 126], the fluid flow concerned is not only multiphase but also multi-component, and its properties depend on its compositions. To account for these physics in history matching or forward predictions, a compositional flow simulator is usually required [4, 39, 95].

Reservoir geomechanical responses associated with these flow processes are often not negligible. For example, surface uplift has been detected and measured by satellite based interferometric synthetic aperture radar (InSAR) for the In Salah gas project in Algeria which was the world's first industrial scale CO_2 storage project [110]. This ground surface subsidence/uplift information has been used for estimating rock material properties [107]. For stress sensitive reservoirs [48, 105], permeability changes induced by solid matrix deformation can significantly affect well productivity. To study the complicated interplays between the multi-component multiphase flow and the reservoir solid skeleton, the geomechanics model presented in Chapter 3 is iteratively coupled to the EOS compositional flow model in IPARS. Both porosity and permeability couplings are considered. The iteratively coupled poroelasticity model is then explicitly coupled to a thermal energy balance model to account for thermal effects on reservoir deformation and fluid motion.

4.2 Compositional Flow Model

Several assumptions have been made for the compositional flow model implemented in IPARS [76, 126]:

1. Three phases are considered, namely, an aqueous (water) phase, a non-aqueous liquid phase, and a gaseous phase.
2. No mass transfer between the aqueous phase and the other two phases; hydrocarbon components can transfer between non-aqueous liquid phase and the gas phase.
3. Fluid flow is described by Darcy's law.
4. The principal directions of the permeability tensor are aligned with the coordinate directions, therefore the permeability tensor is diagonal.
5. No-flow boundary conditions are assumed for all of the reservoir boundaries.
6. Well is treated as sink/source terms by Peaceman well model [100].

7. Reservoir solid skeleton deformation is governed by an isotropic linear elasticity model.

4.2.1 Porosity Coupling with Geomechanics Model

In conventional compositional flow simulators which are not coupled to a geomechanics model, reservoir bulk volume (volume of solid skeleton) for each grid block or element in the mesh is assumed to be constant, i.e. $V_b(t) = V_b^0$ for each grid block, where $V_b(t)$ is the bulk volume at the reservoir time t and V_b^0 is the initial (reference) bulk volume. As a result, the porosity term in the flow mass conservation equation is referred to as reservoir porosity [114]. However, when reservoir solid skeleton deformation is considered, the bulk volume varies and the porosity term in the flow equation is the true porosity through which the mass conservation equations for flow and solid skeleton are connected. In this section, we follow a procedure similar to the approach described by Gai [51] and Chen et al. [32] to derive the porosity coupling term for the compositional flow model equation. The stress-dependent permeability coupling will be presented in Section 4.3.

When the compositional flow and solid matrix deformation are coupled, the mass conservation equations for flow and solid phase read:

$$\begin{aligned} \frac{\partial \phi N_i}{\partial t} + \nabla \cdot \sum_j \left(\rho_j \xi_i^j S_j \phi \mathbf{v}_{fj} \right) &= q_i && (4.1) \\ \frac{\partial (1-\phi)\rho_s}{\partial t} + \nabla \cdot ((1-\phi)\rho_s \mathbf{v_s}) &= 0 && (4.2) \end{aligned}$$

Equation 4.1 is the molar mass conservation equation for fluid component i and equation 4.2 is the solid phase mass conservation law. Superscript or subscript j denotes fluid phase ($j = w$ is aqueous phase, $j = l$ is non-aqueous liquid phase, and $j = g$ is non-aquesous gas phase); subscript i denotes component (i=1, $\cdots$, N_c+1. Here i=1 is water component, N_c is the total number of non-aqueous components). ϕ is the true porosity which is defined as the ratio of pore volume to bulk volume in deformed porous media, i.e. $\phi = V_p/V_b$ where V_p is the pore volume. N_i is the component molar concentration, ρ_j is the phase molar density, ξ_i^j is the molar fraction of component i in phase j, S_j is the phase saturation, $\mathbf{v}_{fj}$ is the interstitial velocity of fluid phase j in Eulerian coordinate, q_i is the component source/sink term, ρ_s is the solid phase mass density , and $\mathbf{v}_s$ is the solid phase velocity in Eulerian coordinate. The phase Darcy velocity $\mathbf{v}_j^D$, defined as phase superficial velocity relative to the moving solid skeleton, is connected to $\mathbf{v}_{fj}$ and $\mathbf{v_s}$ as:

$$\mathbf{v}_j^D = \phi S_j(\mathbf{v}_{fj} - \mathbf{v}_s) \tag{4.3}$$

Meanwhile, Darcy's law gives:

$$\mathbf{v}_j^D = -\frac{k_{rj}}{\mu_j}\mathbf{K}(\nabla p_j - \rho_j \mathbf{g}) \tag{4.4}$$

where k_{rj} is the phase relative permeability, μ_j is the phase viscosity, $\mathbf{K}$ is the absolute permeability tensor, and $\mathbf{g}$ is the gravitational acceleration vector. From equation 4.3, $\mathbf{v}_{fj}$ can be expressed as:

$$\phi S_j \mathbf{v}_{fj} = \mathbf{v}_j^D + \phi S_j \mathbf{v}_s \tag{4.5}$$

Substituting equation 4.5 into 4.1 we have:

$$\frac{\partial \phi N_i}{\partial t} + \nabla \cdot \sum_j (\rho_j \xi_i^j \mathbf{v}_j^D) + \nabla \cdot \sum_j (\rho_j \xi_i^j S_j \phi \mathbf{v}_s) = q_i \tag{4.6}$$

Note that by the definition of component molar density, $\sum_j (\rho_j \xi_i^j S_j) = N_i$, therefore equation 4.6 can be rewritten as:

$$\begin{aligned}\frac{\partial \phi N_i}{\partial t} + \nabla \cdot \sum_j (\rho_j \xi_i^j \mathbf{v}_j^D) + \nabla \cdot (\phi N_i \mathbf{v}_s) &= q_i && (4.7)\\ \frac{\partial \phi N_i}{\partial t} + \nabla \cdot \sum_j (\rho_j \xi_i^j \mathbf{v}_j^D) + \mathbf{v}_s \cdot \nabla(\phi N_i) + \phi N_i \nabla \cdot \mathbf{v}_s &= q_i && (4.8)\end{aligned}$$

Using the material time derivative relation

$$\frac{d(\cdot)}{dt} = \frac{\partial (\cdot)}{\partial t} + \mathbf{v}_s \cdot \nabla(\cdot) \tag{4.9}$$

equation 4.8 can be rearranged to:

$$\frac{d(\phi N_i)}{dt} + \nabla \cdot \sum_\alpha (\rho_\alpha \xi_i^\alpha \mathbf{v}_\alpha^D) + \phi N_i \nabla \cdot \mathbf{v}_s = q_i \tag{4.10}$$

Similarly, equation 4.2 can be written with material time derivative as:

$$\frac{d(1-\phi)\rho_s}{dt} + (1-\phi)\rho_s \nabla \cdot \mathbf{v}_s = 0 \tag{4.11}$$

Or

$$\nabla \cdot \mathbf{v}_s = -\frac{1}{(1-\phi)\rho_s} \frac{d(1-\phi)\rho_s}{dt} \tag{4.12}$$

In equation 4.12, $1 - \phi = V_s/V_b$ where $V_s = V_b - V_p$ is the solid grain volume. Note that solid grain mass is conserved in a deformable porous media, i.e.

$\rho_s V_s =$ constant. Use this relation in equation 4.12 we have:

$$\begin{aligned}\nabla \cdot \mathbf{v}_s &= -\frac{V_b}{\rho_s V_s}\frac{d}{dt}\left(\frac{\rho_s V_s}{V_b}\right)\\ &= -V_b\frac{d}{dt}\left(\frac{1}{V_b}\right)\\ &= \frac{1}{V_b}\frac{dV_b}{dt}\\ &= \frac{d\varepsilon_v}{dt} \qquad (4.13)\end{aligned}$$

where $\varepsilon_v = tr(\boldsymbol{\varepsilon})$ is the volumetric strain. Combining equations 4.13 and 4.10, and adding and subtracting $\varepsilon_v \frac{d(\phi N_i)}{dt}$ in the LHS of equation 4.10, it becomes:

$$\frac{d\left(\phi(1+\varepsilon_v)N_i\right)}{dt} + \nabla \cdot \sum_j (\rho_j \xi_i^j \mathbf{v}_j^D) - \varepsilon_v \frac{d(\phi N_i)}{dt} = q_i \qquad (4.14)$$

Assuming small and quasi-static deformation for the linear poroelasticity model, i.e. $\varepsilon_v \ll 1$ and $\mathbf{v}_s \ll 1$, we note that $\varepsilon_v \frac{d(\phi N_i)}{dt} \ll \frac{d(\phi(1+\varepsilon_v)N_i)}{dt}$ and $\mathbf{v}_s \cdot \nabla\left(\phi(1+\varepsilon_v)N_i\right) \ll \frac{\partial(\phi(1+\varepsilon_v)N_i)}{\partial t}$. Thus equation 4.14 can be written in a form analogous to a decoupled fluid flow equation by neglecting the terms $\varepsilon_v \frac{d(\phi N_i)}{dt}$ and $\mathbf{v}_s \cdot \nabla\left(\phi(1+\varepsilon_v)N_i\right)$:

$$\frac{\partial\left(\phi(1+\varepsilon_v)N_i\right)}{\partial t} + \nabla \cdot \sum_j (\rho_j \xi_i^j \mathbf{v}_j^D) = q_i \qquad (4.15)$$

The reservoir geomechanical deformation influences the coupled compositional flow model through the term $\phi(1+\varepsilon_v)$. Using the approximate relation for the relative change of true porosity in a deformable porous media [31, 51, 54], we have

$$\frac{d\phi}{\phi} = \left(\frac{1}{\phi}\left(\frac{1}{K_{dr}} - \frac{1}{K_s}\right) - \frac{1}{K_{dr}}\right)(d\sigma_v + dp) \qquad (4.16)$$

where $K_{dr} = \frac{3\lambda+2G}{3}$ is the drained bulk modulus of solid skeleton, K_s is the solid grain modulus, σ_v is the mean total stress defined in equatinon 3.14. Multiplying both sides of equation 4.16 by *phi* and integrating it from reference state to current state yields [51, 114]

$$\begin{aligned}
\int d\phi &= \int \left(\left(\frac{1}{K_{dr}} - \frac{1}{K_s} \right) - \frac{\phi}{K_{dr}} \right) d(\sigma_v + p) \\
\int d\phi &\approx \left(\left(\frac{1}{K_{dr}} - \frac{1}{K_s} \right) - \frac{\phi_0}{K_{dr}} \right) \int d(\sigma_v + p) \qquad (4.17) \\
\phi &= \phi_0 + \left(\frac{1-\phi_0}{K_{dr}} - \frac{1}{K_s} \right) \big((\sigma_v - \sigma_v^0) + (p - p_0) \big) \qquad (4.18)
\end{aligned}$$

In deriving equation 4.18, the assumption that the solid matrix deformation is linear elastic is used so K_{dr} and K_s are constants; and small deformation is assumed therefore ϕ in the RHS of equation 4.17 is approximated by ϕ_0 for integration. Therefore

$$\phi(1+\varepsilon_v) = \left(\phi_0 + \left(\frac{1-\phi_0}{K_{dr}} - \frac{1}{K_s} \right) \big((\sigma_v - \sigma_v^0) + (p - p_0) \big) \right) (1+\varepsilon_v) \qquad (4.19)$$

Under the small deformation assumption

$$\left(\frac{1-\phi_0}{K_{dr}} - \frac{1}{K_s} \right) \big((\sigma_v - \sigma_v^0) + (p - p_0) \big) = O(\varepsilon_v) = o(1) \qquad (4.20)$$

and

$$\left(\frac{1-\phi_0}{K_{dr}} - \frac{1}{K_s} \right) \big((\sigma_v - \sigma_v^0) + (p - p_0) \big) \varepsilon_v = O\left(\varepsilon_v^2\right) \qquad (4.21)$$

The total stress equation 3.14 gives

$$\sigma_v - \sigma_v^0 = \frac{3\lambda + 2G}{3} \varepsilon_v - (3\lambda + 2G)\alpha^T (T - T_0) - \alpha(p - p_0) \qquad (4.22)$$

By neglecting the $O\left(\varepsilon_v^2\right)$ term in equation 4.19, and using 4.22, 4.19 becomes

$$\begin{aligned}
\phi(1+\varepsilon_v) &\approx \phi_0 + \phi_0\varepsilon_v + \left(\frac{1-\phi_0}{K_{dr}} - \frac{1}{K_s}\right)\big((\sigma_v - \sigma_v^0) + (p - p_0)\big) \\
&= \phi_0 + \frac{\phi_0}{K_{dr}}\big((\sigma_v - \sigma_v^0) + \alpha(p-p_0) + 3K_{dr}\alpha^T(T-T_0)\big) \\
&\quad + \left(\frac{1-\phi_0}{K_{dr}} - \frac{1}{K_s}\right)\big((\sigma_v - \sigma_v^0) + (p - p_0)\big) \\
&= \phi_0 + \left(\frac{1}{K_{dr}} - \frac{1}{K_s}\right)(\sigma_v - \sigma_v^0) \\
&\quad + \left(\frac{1}{K_{dr}} - \frac{1+\phi_0}{K_s}\right)(p-p_0) + 3\phi_0\alpha^T(T-T_0) \qquad (4.23)
\end{aligned}$$

By recognizing the definition of Biot's coefficient α [41]

$$\alpha = 1 - \frac{K_{dr}}{K_s} \qquad (4.24)$$

equation 4.23 can also be written in terms of ε_v, p, and T [114, 115]

$$\begin{aligned}
\phi(1+\varepsilon_v) &\approx \phi_0 + \phi_0\varepsilon_v \\
&\quad + \left(\frac{1-\phi_0}{K_{dr}} - \frac{1}{K_s}\right)\left(K_{dr}\varepsilon_v + \frac{K_{dr}}{K_s}(p-p_0) - 3K_{dr}\alpha^T(T-T_0)\right) \\
&= \phi_0 + \alpha\varepsilon_v + \frac{\alpha-\phi_0}{K_s}(p-p_0) + 3(\phi_0-\alpha)\alpha^T(T-T_0) \\
&= \phi_0 + \alpha\varepsilon_v + \frac{1}{N}(p-p_0) + 3(\phi_0-\alpha)\alpha^T(T-T_0) \qquad (4.25)
\end{aligned}$$

Here N is the modulus relating the pore pressure p linearly to the porosity variation when the volumetric strain ε_v and the temperature variation are zero [41]

$$\frac{1}{N} = \frac{(1-\alpha)(\alpha-\phi^0)}{K_{dr}} = \frac{\alpha-\phi^0}{K_s} \qquad (4.26)$$

By definition of the true porosity ϕ and the volumetric strain ε_v

$$\begin{aligned}\phi(1+\varepsilon_v) &= \frac{V_p}{V_b}\left(1+\frac{V_b-V_b^0}{V_b^0}\right)\\ &= \frac{V_p}{V_b^0}\end{aligned}\tag{4.27}$$

It is clear from equation 4.27 that $\phi(1+\varepsilon_v)$ is the reservoir porosity for deformable reservoir bulk volume [114, 115]. Define ϕ^* as the reservoir porosity in coupled poromechanics/thermoporomechanics model

$$\begin{aligned}\phi^* &= \phi(1+\varepsilon_v)\\ &= \phi_0+\alpha\varepsilon_v+\frac{1}{N}(p-p_0)+3(\phi_0-\alpha)\alpha^T(T-T_0)\end{aligned}\tag{4.28}$$

Different from the reservoir porosity in conventional compositional flow model which assumes the form

$$\phi^* = \phi_0\left(1+c_r(p-p_0)\right)\tag{4.29}$$

where c_r is the constant rock compressibility, the reservoir porosity for coupled compositional flow, geomechanics,and thermal models is a function of pore pressure p, solid matrix volumetric strain ε_v, and temperature T.

4.2.2 Coupled Compositional Flow Model Equations

The coupled compositional flow model equations consist of N_c+1 component molar mass conservation equations, Darcy's law for 3 phase velocities, and a set of constitutive equations relating fluid properties to state variables (p, T, N_i).

Coupled Mass Conservation Equation:

$$\frac{\partial(\phi^* N_i)}{\partial t} + \nabla \cdot \sum_j (\rho_j \xi_i^j \mathbf{v}_j^D) = q_i \tag{4.30}$$

Volume Constraint:

$$\sum_j S_j = 1 \tag{4.31}$$

Thermodynamic Equilibrium Equation:

$$f_i^l = f_i^g \quad \text{for} \quad i = 1, 2, \cdots, N_c \tag{4.32}$$

Darcy's Law:

$$\mathbf{v}_j^D = -\frac{k_{rj}}{\mu_j}\mathbf{K}(\nabla p_j - \rho_j \mathbf{g}) \tag{4.33}$$

Constitutive Equations:

$$\phi^* = \phi_0 + \alpha\varepsilon_v + \frac{1}{N}(p - p_0) + 3(\phi_0 - \alpha)\alpha^T(T - T_0) \tag{4.34}$$

$$\xi_i^j = \xi_i^j(p, T, N_i) \tag{4.35}$$

$$S_j = S_j(p, T, N_i, \xi_i^j) \tag{4.36}$$

$$p_j = p + p_{cj}(S_j) \tag{4.37}$$

$$\mu_j = \mu_j(p, T, \xi_i^j) \tag{4.38}$$

$$\rho_j = \rho_j(p, T, \xi_i^j) \tag{4.39}$$

$$k_{rj} = k_{rj}(S_j) \tag{4.40}$$

$$f_i^j = \Phi_i^j \xi_i^j p \tag{4.41}$$

$$\Phi_i^j = \Phi_i^j(p, T, \xi_i^j, N_i) \tag{4.42}$$

In constitutive equations 4.34–4.42, p_{cj} is the phase capillary pressure, f_i^j is the fugacity of component i in phase j, and Φ_i^j is the fugacity coefficient of component i in phase j. The component phase molar fraction ξ_i^j can be obtained by flash calculation given (p, T, N_i). In IPARS, the cubic Peng-Robinson equation of state [101, 126] is employed for flash calculation. Phase viscosity μ_j is calculated using Lohrenz-Bray-Clark correlation [80].

4.2.3 Fixed-Stress Iterative Coupling

The coupled compositional flow and linear elasticity model (equations 4.30–4.42, 3.2, 3.3, and 3.14) represent a set of equations with unknown reference pore pressure p, component molar concentrations N_i, solid phase displacement vector $\mathbf{u}$, and temperature T when thermal energy balance equation is also coupled. Since this poroelasticity/thermoporoelasticity system is computationally very expensive to solve implicitly [47, 51, 97, 114, 115, 126, 131] and we would like to make minimum changes to the existing compositional flow and thermal energy balance models in IPARS [126], we employ the fixed stress iterative coupling scheme introduced in Chapter 2 to couple the compositional flow and geomechanics models. The coupling of the poroelasticity model to the thermal energy balance model will be presented in Section 4.4.

The fixed-stress split solves the compositional flow equation first with the assumption that the mean total stress of the solid skeleton is fixed. It then solves the linear elasticity equation using the updated pressure solution as an external load. The procedure is iterated until the coupled system converges at each time step.

The compositional flow model in IPARS is solved by an iterative implicit pressure explicit concentration (IMPEC) algorithm [45, 95, 126]. The model equations are discretized in space using MFE on the lowest order Raviart-Thomas element (RT_0), the rectangular element, and in time using backward Euler scheme. The mass conservation equation 4.30 gives

$$\frac{\partial \phi N_i}{\partial t} = -\nabla \cdot \sum_j (\rho_j \xi_i^j \mathbf{v}_j^D) + q_i \tag{4.43}$$

The time derivative on LHS of equation 4.43 is approximated by backward Euler scheme as

$$\begin{aligned} \frac{\partial(\phi^* N_i)}{\partial t} &= \frac{1}{\Delta t}(\phi^{*,m+1,k+1} N_i^{m+1,k+1} - \phi^{*,n} N_i^n) \\ &\approx \frac{1}{\Delta t}\left(\phi^{*,m+1,k} N_i^{m+1,k} + N_i^{m+1,k} \delta\phi^{*,m+1,k+1}\right) \\ &\quad + \frac{1}{\Delta t}\left(\phi^{*,m+1,k} \delta N_i^{m+1,k+1} - \phi^n N_i^n\right) \end{aligned} \tag{4.44}$$

where n denotes n^{th} time level, m denotes m^{th} level coupled flow and geomechanics iteration, k denotes k^{th} flow nonlinear (Newton) iteration at $(n+1)^{th}$ time step and $(m+1)^{th}$ poroelasticity iteration, and $\delta(\cdot)^{k+1} = (\cdot)^{k+1} - (\cdot)^k$ denotes $(k+1)^{th}$ Newton iteration solution at $(n+1)^{th}$ time step and $(m+1)^{th}$ poroelasticity iteration. The IMPEC scheme treats all variables on RHS of equation 4.43 explicitly using k^{th} iteration values at $(n+1)^{th}$ step and $(m+1)^{th}$ poroelasticity iteration except that the reference pressure term p uses p^{k+1}. Note that equation 4.28 leads to

$$\delta\phi^{*,k+1} = \alpha \delta\varepsilon_v^{k+1} + \frac{1}{N}\delta p^{k+1} + 3(\phi_0 - \alpha)\alpha^T \delta T^{k+1} \tag{4.45}$$

and equation 4.22 yields

$$\delta\sigma_v^{k+1} = K_{dr}\delta\varepsilon_v^{k+1} - \alpha\delta p^{k+1} - 3K_{dr}\alpha^T\delta T^{k+1} \tag{4.46}$$

Because the thermal energy balance equation is explicitly coupled to the compositional flow and geomechanics model at the end of each time step (see Section 4.4), during Newton iterations for the compositional flow model, $\delta T^{k+1} = 0$. Furthermore, the fixed-stress assumption implies

$$\delta\sigma_v^{k+1} = K_{dr}\delta\varepsilon_v^{k+1} - \alpha\delta p^{k+1} = 0 \tag{4.47}$$

$$\delta\varepsilon_v^{k+1} = \frac{\alpha}{K_{dr}}\delta p^{k+1} \tag{4.48}$$

Therefore

$$\begin{aligned}\delta\phi^{*,k+1} &= \alpha\delta\varepsilon_v^{k+1} + \frac{1}{N}\delta p^{k+1} + 3(\phi_0 - \alpha)\alpha^T\delta T^{k+1} \\ &\approx \left(\frac{\alpha^2}{K_{dr}} + \frac{1}{N}\right)\delta p^{k+1} \end{aligned} \tag{4.49}$$

With equations 4.44 and 4.49, 4.43 is decoupled from solid skeleton deformation and the compositional flow model can be solved independently. It should be emphasized that only the rock compressibility $c_r = \frac{1}{\phi^{*,k}}\frac{\delta\phi^{*,k+1}}{\delta p^{k+1}}$ in the compositional flow simulator needs to be changed when the geomechanics coupling is considered. This demonstrates the advantage of the fixed-stress iterative coupling scheme in extending the capability of the existing flow simulators to study coupled poromechanics problems by adding a geomechanics module.

By appealing to Newton-Raphson method [126], the component molar mass balance equation 4.43 leads to

$$\delta N_i^{k+1} = \mathcal{F}(\delta p^{k+1}) \tag{4.50}$$

and the thermodynamic equilibrium equation 4.32 yields

$$\delta \ln K_i^{k+1} = \mathcal{G}(\delta p^{k+1}, \delta N_i^{k+1}) \tag{4.51}$$

where K_i is the K-value of component i defined by

$$K_i = \frac{\xi_i^g}{\xi_i^l} \tag{4.52}$$

Taylor expansion of the volume constraint equation 4.31 to the first order terms gives

$$\frac{\partial S_T}{\partial p}\delta p^{k+1} + \sum_i \frac{\partial S_T}{\partial N_i}\delta N_i^{k+1} + \sum_i \frac{\partial S_T}{\partial \ln K_i}\delta \ln K_i^{k+1} = 1 - S_T^k \tag{4.53}$$

Here $S_T = \sum_j S_j$ is the total saturation of all fluid phases. Substituting equations 4.50 and 4.51 into 4.53, a linear system for δ^{k+1} can be formed

$$\mathbf{A}\delta p^{k+1} = \mathbf{b} \tag{4.54}$$

and δp^{k+1} can be solved using a variety of iterative solvers, e.g. Generalized Minimal Residue (GMRES), Biconjugate Gradient Stabilized (BCGS), and Multigrid solvers implemented in IPARS with different preconditioners to accelerate the convergence. Following that, $\delta\phi^{*,k+1}$ and δN_i^{k+1} are updated using equations 4.49 and 4.50, respectively. To preserve mass balance, instead of updating $N_i^{k+1} = N_i^k + \delta N_i^{k+1}$, we update the component molar concentration explicitly [126]

$$N_i^{k+1} = \frac{1}{\phi^{*,k+1}}(\phi^{*,k} N_i^k + N_i^k \delta\phi^{*,k+1} + \phi^{*,k}\delta N_i^{k+1}) \tag{4.55}$$

Then ξ_i^j, S_j, etc, are obtained from flash calculation and mixing rule and the volume constraint equation 4.31 is checked to determine whether to continue pressure iterations 4.54.

After the solution of the compositional flow model converges, $p^{m+1,k+1}$ is substituted into equation 3.17 as pressure load term. If the thermal effect is considered, T^n from the last time step is also used in 3.17 as an external load. The linear equation 3.17 can be solved using CG as described in Section 3.3.3 for $\mathbf{u}^{m+1}$. With $\mathbf{u}^{m+1}$ and p^{m+1}, the exact reservoir porosity $\phi_{mech}^{*,m+1}$ is formed from equation 4.28

$$\begin{aligned} \phi_{mech}^{*,m+1} &= \phi_{mech}^{*,m} + \delta\phi_{mech}^{*,m+1} \\ &= \phi_{mech}^{*,m} + \frac{1}{N}\delta p^{m+1} + \alpha\nabla\cdot\delta\varepsilon_v^{m+1} \end{aligned} \tag{4.56}$$

In equation 4.56, $\delta p^{m+1} = \sum_k \delta p^{m+1,k}$ is the total pressure changes over multiple Newton iterations for the compositional model. On the other hand, the reservoir porosity calculated in the compositional flow model assuming the form

$$\begin{aligned} \phi^{*,m+1} &= \phi^{*,m} + \delta\phi_{flow}^{*,m+1} \\ &= \phi^{*,m} + \left(\frac{1}{N} + \frac{\alpha^2}{K_{dr}}\right)\sum_k \delta p^{m+1,k} \end{aligned} \tag{4.57}$$

The fixed stress assumption in compositional flow update is justified if

$$\begin{aligned} \left\|\phi_{mech}^{*,m+1} - \phi^{*,m+1}\right\|_{L_\infty} &= \left\|\alpha\delta\varepsilon_v^{m+1} - \frac{\alpha^2\delta p^{m+1}}{K_{dr}}\right\|_{L_\infty} \\ &= \left\|\frac{\alpha}{K_{dr}}\delta\sigma_v^{m+1}\right\|_{L_\infty} < TOL \end{aligned} \tag{4.58}$$

However, checking equation 4.58 as the convergence criterion for the coupled poroelasticity model may result in over-solving or under-solving the coupled system, depending on the choice of the tolerance TOL. Instead, we feed the exact reservoir porosity $\phi_{mech}^{*,m+1}$ to the compositional flow simulator, form a new residue for the pressure equation 4.54, and check the convergence of the flow equation. The convergence of the compositional flow equation with the exact reservoir porosity $\phi_{mech}^{*,m+1}$ is equivalent to the convergence of the coupled compositional flow and geomechanics model.

In Figure 4.1 we provide a flow diagram that illustrates the fixed-stress iterative coupling procedure for porosity coupling between the compositional flow and linear elasticity models.

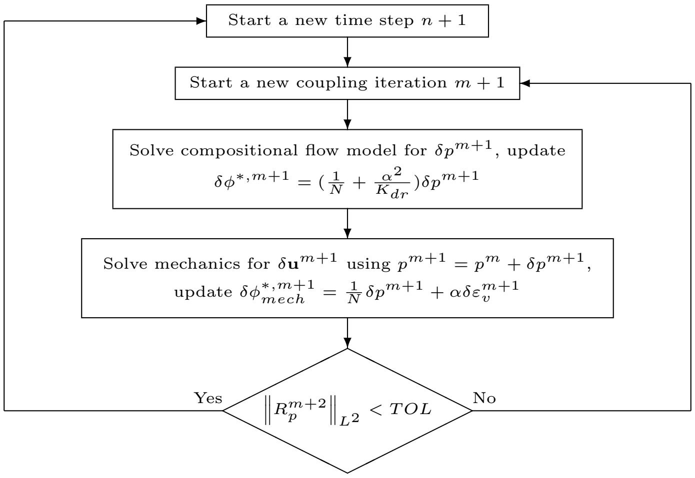

Figure 4.1: Fixed-stress split for porosity coupling procedure

4.2.4 Numerical Example

The iteratively coupled IMPEC MFE compositional flow and CG linear elasticity model in IPARS has been tested against an in-house fully implicit poromechanics simulator from a major oil company. For the test case of multiphase and multi-component flow coupled with linear elasticity, the iteratively coupled solutions match their fully implicit counterparts excellently. However, due to the proprietary concerns, the comparison results can not be published here.

In this section, we present a single well CO_2 injection example to demonstrate the fast convergence of the iteratively coupled compositional flow and linear elasticity model. Table 4.1 elaborates the input parameters and the computational complexity of the problem and Figure 4.2 shows the model mesh. For the compositional flow problem, no-flow boundary conditions are applied on all of the boundary faces; for the geomechanics problem, zero normal displacement and zero shear traction are specified on all of the boundary faces except that on the top surface, a compressive traction is prescribed in the normal direction. An injection well is drilled at the center of the reservoir and is only completed at the bottom of the reservoir. Figure 4.3–4.6 are the computed solutions at 3.0 day for pressure, CO_2 concentration, x-displacement (vertical), and y-displacement, respectively. Solid lines in Figure 4.3–4.6 indicate the grid partitioning for 64 processes. Note that Figure 4.3 and 4.4 are bottom view whereas Figure 4.5 and 4.6 are top view. The unit for the displacements is inch throughout this dissertation.

Figure 4.7 shows the number of iterations at each time step for the coupled model, given a flow Newton iteration tolerance of $TOL2 = 1.0 \times 10^{-5}$. For the highly nonlinear carbon sequestration problem, the fixed-stress split only requires 1 or 2 iteration(s) to converge to the coupled solution, demonstrating the efficiency of the fixed-stress iterative coupling scheme in solving coupled poromechanics system.

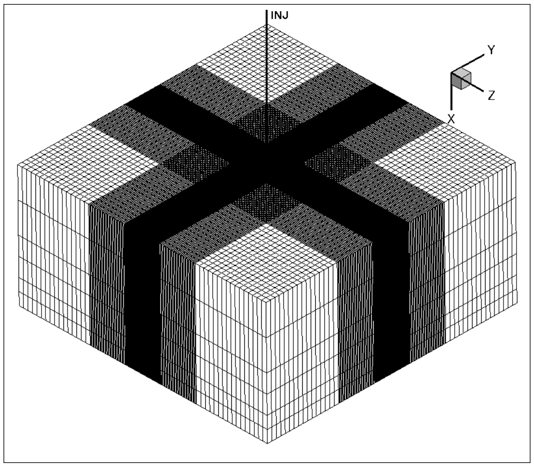

Figure 4.2: Single well CO_2 injection model mesh

4.3 Stress-dependent Permeability

In stress-sensitive or naturally fractured reservoirs, the permeability dependency on reservoir stress state can play an important role in regulating fluid flow motions and well productivity changes. Chin et al. [36] and Raghavan and Chin [105] did extensive studies on stress-dependent permeabilities and their implications on well productivity changes. We implement the three stress-dependent permeability models studied in [105] in IPARS.

SYMBOL	QUANTITY	VALUE
X_L	dimension in x	100 ft
Y_L	dimension in y	3500 ft
Z_L	dimension in z	3500 ft
N_x	number of grid in x	6
N_y, N_z	# grid in y, z	192
N_c	# component	2 (Brine, CO_2)
k_{yy}, k_{zz}	horizontal permeability	50 md
k_{xx}	vertical permeability	5 md
ϕ_0	initial porosity	0.3
ρ_1	brine density at p=0	62.4 lb_m/ft^3
μ_1	brine viscosity	0.7 cp
c_f	brine compressibility	3.3×10^{-6} $/psi$
$N_{1,0}$	initial brine concentration	1.0
p_0	initial pressure	hydrostatic
Q_2	CO_2 injection rate	3000 mscf/day
ρ_s	rock density	165 lb_m/ft^3
E	Young's modulus	1.0×10^5 psi
ν	Poisson's ratio	0.3
α	Biot's constant	1.0
σ_{xx}	stress on top surface	-5200 psi
DoF_{flow}	Number of pressure unknowns	221184
DoF_{mech}	Number of displacement unknowns	782229

Table 4.1: Parameters for single well CO_2 injection example

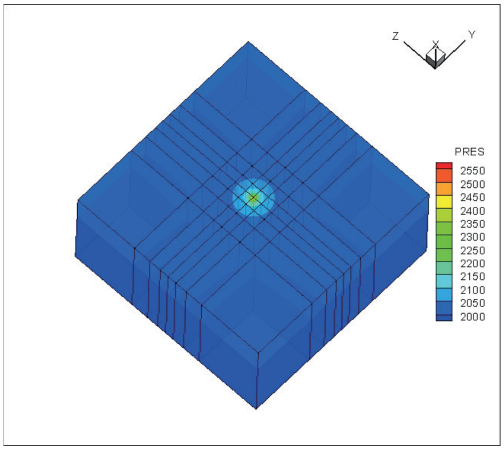

Figure 4.3: CO_2 injection case: pressure at 3.0 days

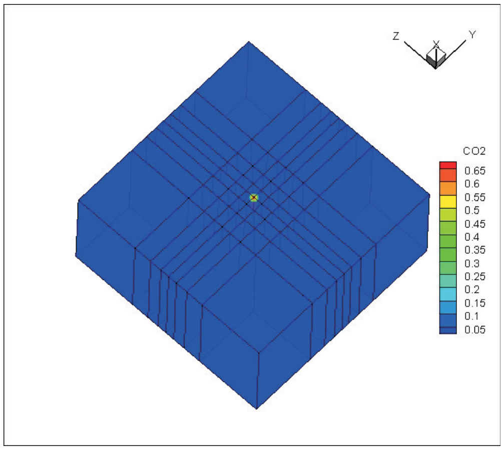

Figure 4.4: CO_2 injection case: CO_2 concentration at 3.0 days

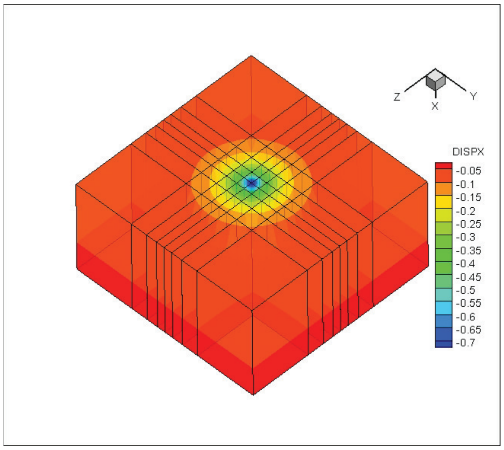

Figure 4.5: CO_2 injection case: x-displacement at 3.0 days

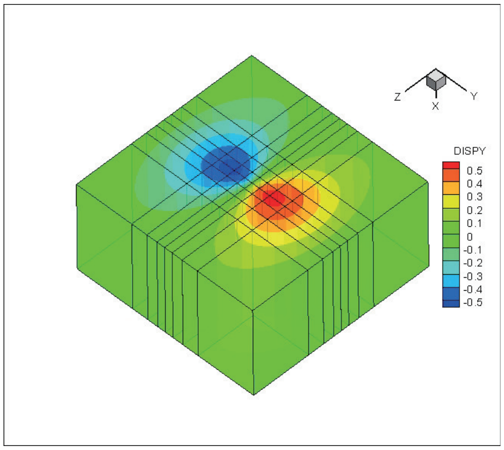

Figure 4.6: CO_2 injection case: y-displacement at 3.0 days

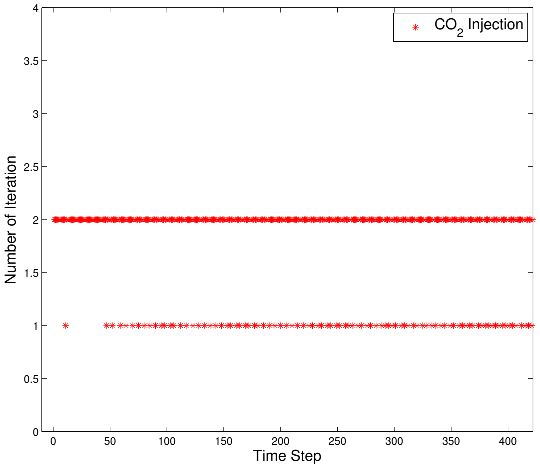

Figure 4.7: CO_2 injection case: number of iterations at each time step

$$
\begin{aligned}
k_i &= k_{i,0} e^{b(\sigma_v^e - \sigma_{v,0}^e)} && (4.59)\\
k_i &= k_{i,0} \frac{1.0 + m\sigma_v^e}{1.0 + m\sigma_{v,0}^e} && (4.60)\\
k_i &= k_{i,0} (\phi^* / \phi_0^*)^n && (4.61)
\end{aligned}
$$

In equations 4.59–4.61, k_i is the magnitude of a component of a diagonal permeability tensor, $k_{i,0}$ is the corresponding reference value. σ_v^e is the mean effective stress defined in 3.13, $\sigma_{v,0}^e$ is the reference mean effective stress. ϕ^* and ϕ_0^* are reservoir porosity and reference reservoir porosity, respectively. b, m, and n are material constants of reservoir rock and can be experimentally determined. In our iteratively coupled poroelasticity simulator, reservoir permeability is updated after the linear elasticity equation 3.17 is solved and the exact reservoir porosity 4.28 is calculated. Transmissibilities for reservoir grid blocks and well element permeabilities are updated accordingly for the next compositional flow solve. Figure 4.8 is the flow chart for both porosity and permeability coupling between the flow and geomechanics models.

4.3.1 Numerical Examples

4.3.1.1 Single Well Drainage Problem

The first numerical example is a single well drainage problem presented in [105]. Figure 4.9 shows the schematic of the model problem. It is a single phase, two-dimensional problem with constant bottom-hole pressure (BHP) in the wellbore and constant external pressure boundary condition p_e at the

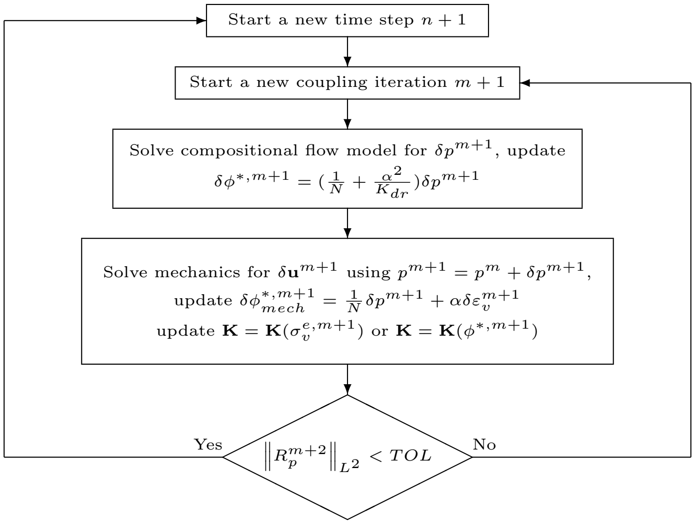

Figure 4.8: Porosity and permeability coupling procedure

drainage radius r_e. We model this 2D problem in IPARS as a 3D one. Because of the symmetry, only one quarter of the circular reservoir is simulated. Figure 4.10 is the model grid set up in IPARS. We use multiple constant BHP injection wells located at the external boundary to approximate the constant external pressure boundary condition p_e. For the geomechanics problem, an overburden (compressive) stress of 7000 *psi* is prescribed on top of the reservoir. All the other boundary faces have zero normal displacement and zero shear traction boundary conditions.

Based on extensive numerical simulations, Raghavan and Chin [105] concluded that the well productivity reduction as a result of reservoir permeability changes due to solid skeleton deformation can be quantified as a skin

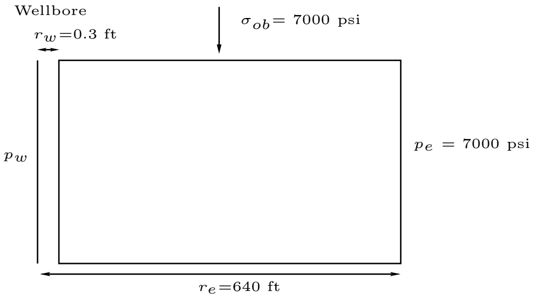

Figure 4.9: Schematic of single well drainage problem

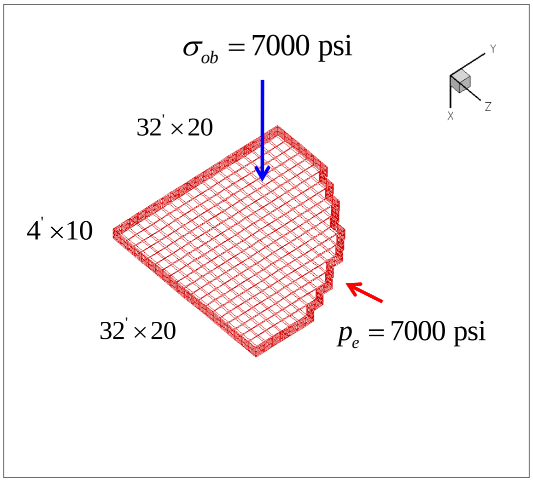

Figure 4.10: Grid of single well drainage problem in IPARS

factor s

$$\frac{q}{q_{id}} = \frac{\ln(r_e/r_w)}{\ln(r_e/r_w) + s} \tag{4.62}$$

where r_w is the wellbore radius, q is the steady state oil production rate, and q_{id} is the ideal (without stress-dependent permeability) steady state oil production rate. This skin factor is affected by rock mechanical properties such as Poisson's ratio, operation conditions such as the BHP for the production well, and the parameter of the stress-dependent permeability model for different rock types. For example, for the stress-dependent permeability model 4.59, they obtained a relation for the skin factor by curve-fitting the data from their numerical experiments

$$s/\ln(r_e/r_w) = 0.15278 \cdot b \cdot (p_e - p_w) \cdot (2 + \nu)/(1 + \nu) \tag{4.63}$$

In equation 4.63, p_w is the BHP of the production well. We ran six numerical simulations using the model grid in Figure 4.10 and the stress-dependent permeability model 4.59 with different b, production well BHP, and Poisson's ratio. Table 4.2 lists the input parameters common to the six numerical simulations. Note that permeability tensor is assumed to be isotropic for this case and its reference magnitude k_0 is given at a reference effective mean stress state $\sigma^e_{v,0}$. Since a geomechanics model initialization step at the beginning of the simulation typically generates non-zero initial mean effective stress, the magnitude of the permeability k is usually not equal to k_0 at the beginning of the simulation.

SYMBOL	QUANTITY	VALUE
r_e	drainage radius	640 ft
r_w	wellbore radius	0.3 ft
H	reservoir thickness	40 ft
NX	number of grids in x	10
NY, NZ	number of grids in y, z	20
k_0	reference permeability	60 md
$\sigma^e_{v,0}$	reference effective mean stress	0 psi
ϕ_0	initial porosity	0.2
μ	oil viscosity	3.7 cp
p_e	pressure boundary condition	7000 psi
E	Young's modulus	1.0×10^7 psi
α	Biot's constant	1.0
σ_{ob}	compressive overburden stress	7000 psi

Table 4.2: Common parameters for single well drainage problem

Case No.	b, 1/psi	BHP, psi	Poisson's Ratio
1	1.E-4	3000	0.3
2	5.E-4	1000	0.3
3	5.E-4	3000	0.3
4	5.E-4	5000	0.3
5	1.E-3	3000	0.1
6	1.E-4	3000	0.3

Table 4.3: Test matrix for single well drainage problem

Table 4.3 gives the different parameters for the six simulations we ran. Each case has a different combination of b, BHP, and Poisson's ratio.

We report our simulation results in Figure 4.11. Linear fit between $s/\ln(r_e/r_w)$ and $b(p_e - p_w)(2 + nu)/(1 - \nu)$ from the six experiments gives a slope of 0.159 with $R^2 = 0.973$. Our result matches Raghavan and Chin's (equation 4.63) reasonably. The difference could result from two factors:

1. We use Peaceman's well model whereas Raghavan and Chin used an explicit well model; they also applied p_w as traction boundary condition

at the wellbore for the geomechanics model.

2. We use rectangular grid blocks to approximate the circular reservoir; constant BHP injection wells are employed to approximate the pressure boundary condition at the drainage radius; boundary condition for geomechanics model at the drainage radius is also an approximation of what Raghavan and Chin prescribed in their 2D model.

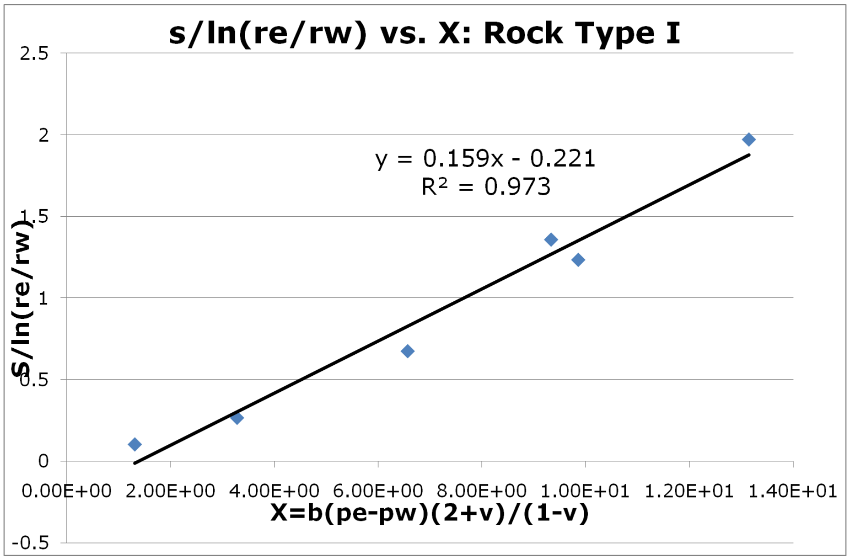

Figure 4.11: Well productivity reduction in single well drainage problem

Figures 4.12 and 4.13 are the x-displacement (vertical displacement) field and the x-permeability field at the steady state for test case 6, respectively. The boundary effect can be clearly seen from the two figures. The permeability reduction from the reference value 60 md is significant because of the exponential relation 4.59 and the fact that the initial mean effective stress is not zero.

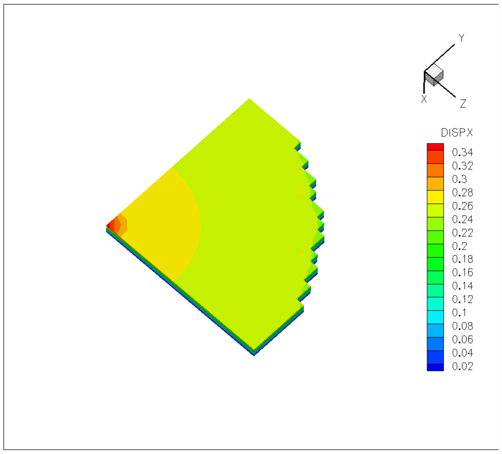

Figure 4.12: Steady state x-displacement for single well drainage problem

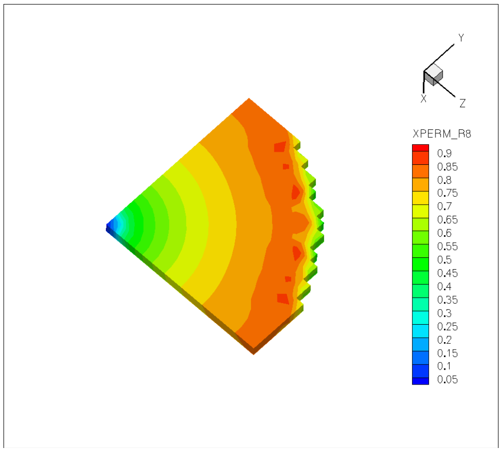

Figure 4.13: Steady state x-permeability for single well drainage problem

4.3.1.2 Cranfield CO_2 Sequestration Simulation

The second numerical example is a field scale CO_2 sequestration simulation. A depleted sandstone oil reservoir, the Cranfield in Natchez, Mississippi [76, 85], was chosen for the pilot CO_2 sequestration project. Kong et al. [48, 76] did a detailed study using IPARS compositional flow model on matching the pressure history of a CO_2 injection well monitored by the Texas Bureau of Economic Geology (BEG). He obtained a good pressure history match for the initial phase of the CO_2 injection. However, the pressure curve from the simulation deviated from the field data when the injection well rate abruptly increased. Kong [48, 76] hypothesized that the formation around the injection well was fractured due to the sudden injection rate increase, leading to a lower injection well BHP compared to the simulation result. By adding a high permeability high porosity channel to mimic a fracture initialized from the injection well, he matched the pressure history when the injection rate is high.

In this study, we simulate the CO_2 sequestration process using the coupled compositional flow and linear elasticity simulator with stress-dependent permeability developed in this work. Because no information of rock mechanical properties and mechanical boundary conditions is available to us at this point and the linear poroelasticity model aforementioned cannot model fracture initialization and propagation, the main objective of this numerical study is not to history match the pressure curve. Instead, we are more interested in seeing how the porosity and permeability changes induced by the (elastic) solid skeleton deformation can affect the reservoir flow field.

Some of the Cranfield simulation model parameters are listed in Table 4.4. CO_2 and brine PVT data, the capillary pressure curve, and relative permeability curves for the Cranfield sandstone formation can be found in Kong [76]. As the first step attempting to account for the geomechanical effect in the numerical model, we use a homogeneous Young's modulus $E = 1.45 \times 10^6$ psi and Poisson's ratio $\nu = 0.3$ for the sandstone. For the elasticity problem, a compressive overburden stress of 10200 psi is prescribed on the top surface of the reservoir; all other boundary surfaces assume zero normal displacement and zero shear stress boundary conditions.

As mentioned in Kong [76], one injection well (CFU 31-F1) and two observation wells (CFU 31-F2 and CFU 31-F3) are located in the detailed area of study (DAS). The computational domain is larger than the DAS. There are

SYMBOL	QUANTITY	VALUE
t^T	total simulation time	595 days
LX	reservoir dimension in x	80 ft
LY	reservoir dimension in y	9400 ft
LZ	reservoir dimension in z	8800 ft
NX	number of grids in x	20
NY	number of grids in y	188
NZ	number of grids in z	176
d	depth of reservoir top surface	9901 ft
T	reservoir temperature	257 °F
p_0	initial pressure	4653.575 psi
s	brine salinity	150000 ppm
S_s^0	initial brine saturation	1.0
N_c	number of non-aqueous components	2: CO_2, brine
c_r	rock compressibility in decoupled flow simulation	5.0×10^{-6}
E	Young's modulus	1.45×10^6 psi
ν	Poisson's ratio	0.3
α	Biot's constant	1.0
σ_{ob}	compressive overburden stress	10200 psi
DoF_{flow}	Number of pressure unknowns	661760
DoF_{mech}	Number of displacement unknowns	2107539

Table 4.4: Cranfield model parameters

another four CO_2 injection wells for enhanced oil recovery (EOR) included in the computational domain, but they are far away from the DAS. Seven constant BHP production wells are employed to approximate pressure boundary conditions. CFU 31-F1 is a rate-specified well which starts to inject CO_2 at day 193. Figure 4.14 illustrates the injection rate schedule for well CFU 31-F1.

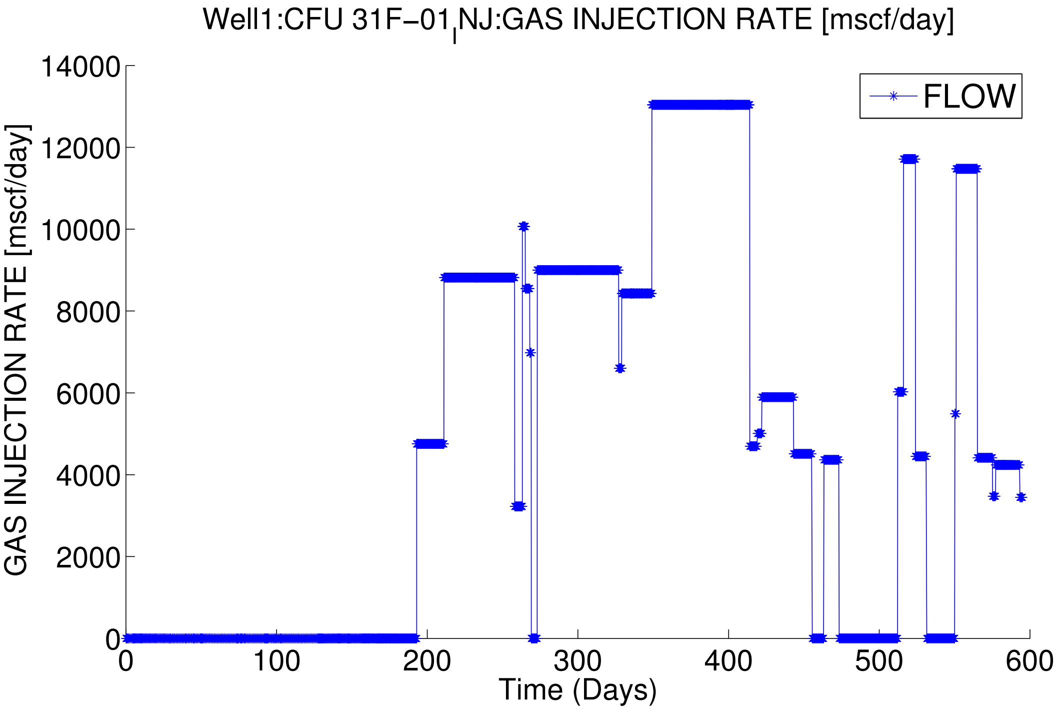

Figure 4.14: Injection well CFU 31-F1 rate schedule

We have run different simulations to compare the BHP history of the injection well CFU 31-F1 between simulation results and field measurement data [76]. All simulations were run with 128 processes. A decoupled compositional flow simulation and a coupled poroelasticity simulation without stress-dependent permeability serve as the base cases. Note that in Figures 4.15–4.17, the connected red circles are field BHP monitoring data. Figure 4.15 shows the pressure history from a simulation with stress-dependent permeability model equation 4.59 and $b = 1.0 \times 10^{-3}\ 1/psi$. For a coupled compositional flow and elasticity simulation without permeability coupling, the BHP curve is consistently higher than that from a decoupled flow simulation. This is reasonable because the reservoir is undergoing compaction and the porosity reduction results in an increase in the BHP of a rate-specified injector. On the other hand, the permeability enhancement due to an increase in mean effective stress or reservoir porosity tends to lower the BHP of a rate-specified injector. The simulation with type I stress-dependent permeability generates the lowest BHP curve in Figure 4.15 which matches the field data satisfactorily when the injector reaches the highest rate (13000 mscf/day in Figure 4.14). But unlike the decoupled flow simulation, it does not match the field BHP data for the initial phase of the injection.

Figure 4.16 shows the pressure history from a simulation with stress-dependent permeability model equation 4.60 and $m = 1.0 \times 10^{-4}\ 1/psi$. The pressure curve is very close to the one from decoupled flow simulation. This implies that the pressure increase induced by reservoir compaction is offset by the pressure decrease as a result of permeability enhancement.

For a simulation with stress-dependent permeability model equation 4.61 and $n = 10$, the pressure history is very close to the one from poroelasticity coupling without stress-dependent permeability (see Figure 4.17). The reason is that the compaction induced pressure increase is the dominant effect in this

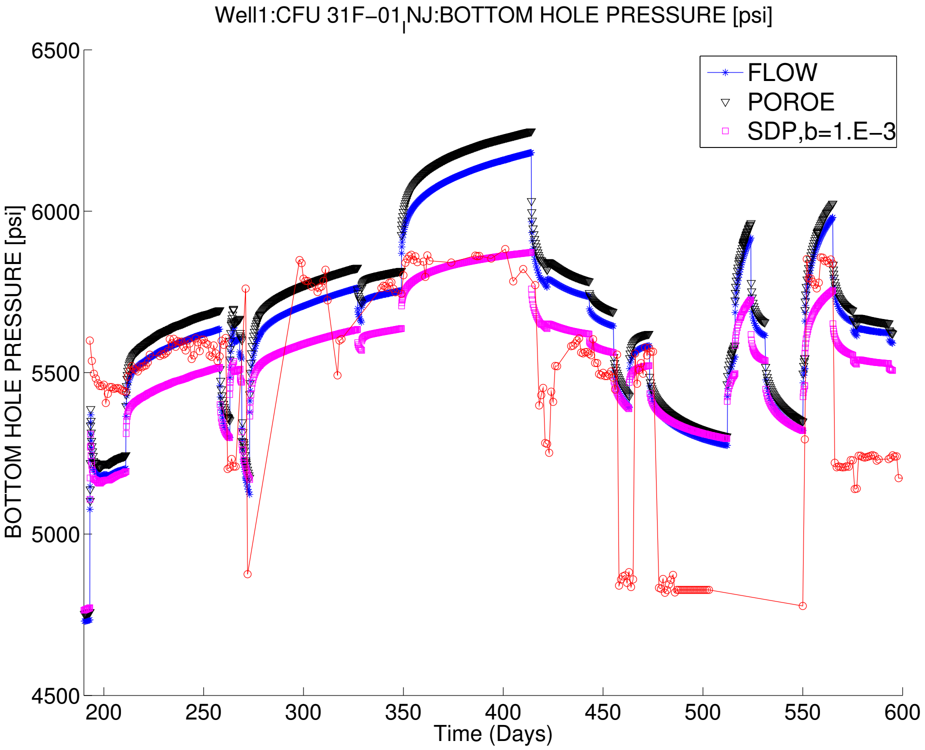

Figure 4.15: CFU 31-F1 pressure history comparison: Type I stress-dependent permeability

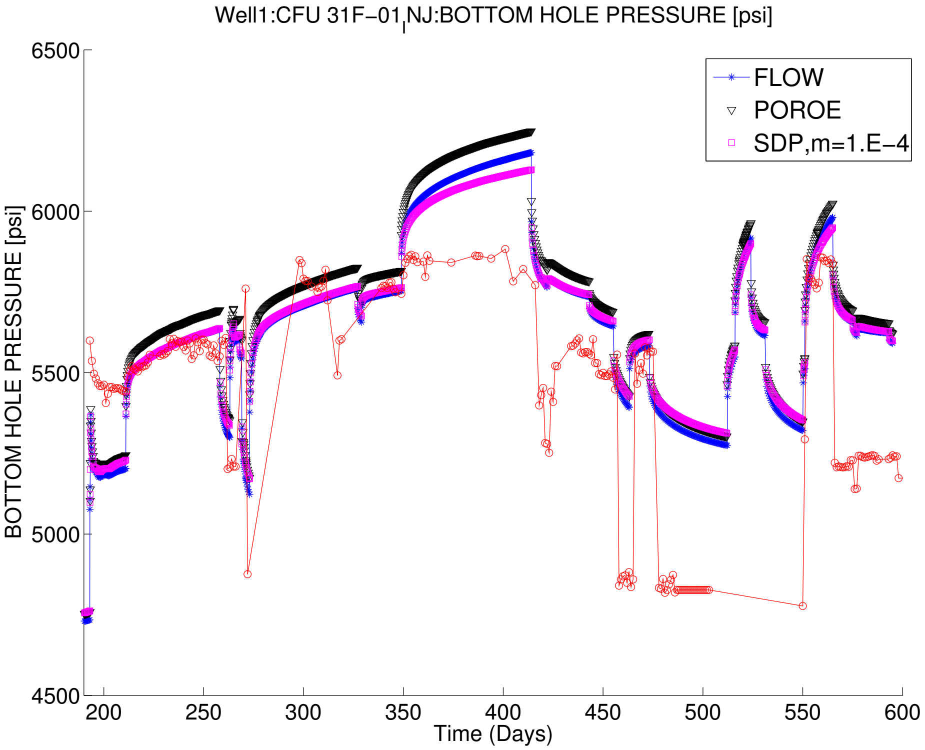

Figure 4.16: CFU 31-F1 pressure history comparison: Type II stress-dependent permeability

scenario.

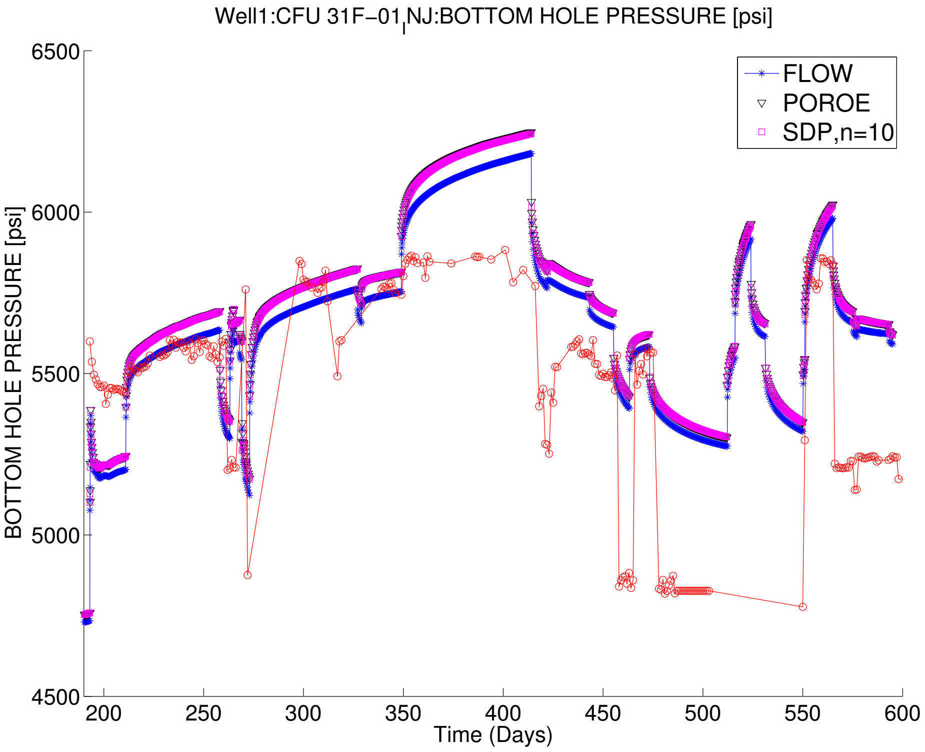

Figure 4.17: CFU 31-F1 pressure history comparison: Type III stress-dependent permeability

Figures 4.18, 4.19, 4.20, and 4.21 show the mean effective stress and y-permeability fields at 0.1 days and 595 days with Type I stress-dependent permeability model, respectively. It is clear that the reservoir mean effective stress increases (tensile stress is positive) due to the CO_2 injection, and so does the reservoir permeability. The exponential stress-dependent permeability relation 4.59 leads to the highest permeability enhancement among the three equations 4.59–4.61 and it lowers the BHP of the rate-specified injector the most.

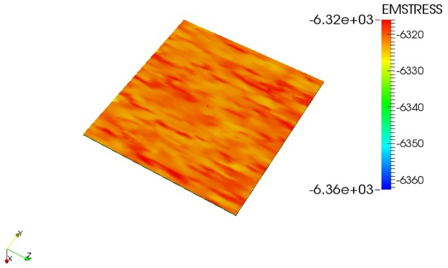

Figure 4.18: Mean effective stress at 0.1 days for Type I rock

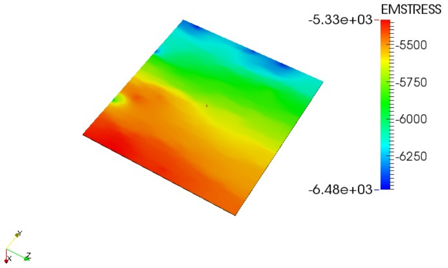

Figure 4.19: Mean effective stress at 595 days for Type I rock

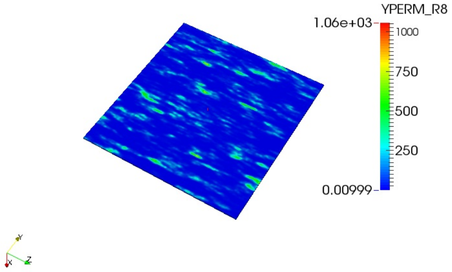

Figure 4.20: Y-permeability at 0.1 days for Type I rock

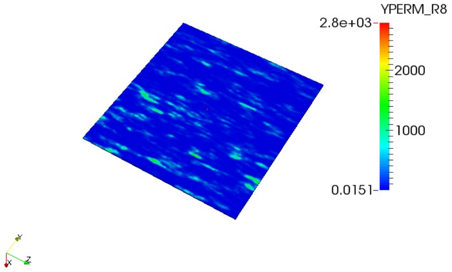

Figure 4.21: Y-permeability at 595 days for Type I rock

4.4 Coupling of Thermoporoelasticity Model

4.4.1 Thermal Energy Balance Model

Thomas [126] implemented a simplified thermal energy balance model [41, 79, 126] in IPARS and explicitly coupled it to the compositional flow model.

In his model fluid flow and solid skeleton mechanical work, phase transition heat, and chemical reaction heat are ignored. This explicitly coupled compositional flow and thermal energy balance model is suitable for simulating subsurface processes like CO_2 sequestration and hot water injection where temperature changes accounted are relatively small [126]. In this section, we explicitly couple the same thermal energy balance model in [126] to the iteratively coupled compositional flow and linear elasticity model developed in this work.

$$\frac{\partial C_{v,res}T}{\partial t} + \nabla \cdot \left(\sum_j \rho_j C_{pj} T \mathbf{v}_j^D - \lambda_T \nabla T \right) = q_H \tag{4.64}$$

Equation 4.64 is the thermal energy balance model equation. Temperature T is the primary unknown, $C_{v,res}$ is the effective isochoric specific heat capacity defined as

$$C_{v,res} = (1 - \phi^*)\rho_s C_{vs} + \phi^* \sum_j \rho_j S_j C_{vj} \tag{4.65}$$

C_{vs} is the isochoric mass specific heat capacity of solid phase, C_{pj} is the isobaric molar specific heat capacity of fluid phase j, C_{vj} is the isochoric molar specific heat capacity of fluid phase j, λ_T is the effective reservoir thermal conductivity, and q_H is the heat source/sink term given by

$$q_H = \sum_j C_{pj} q_j T_{src} \tag{4.66}$$

where T_{src} is the temperature of the injected fluid or at the production well and q_j is the molar injection or production rate per unit volume of phase j.

The thermal energy balance equation 4.64 is solved by a time-split scheme [43, 126] which solves heat convection and conduction successively. Several temperature steps can be nested in a compositional flow step, i.e. $[t^l, t^{l+1}] \in [t^n, t^{n+1}]$. To solve for T^{l+1}, the heat convection equation

$$\frac{\partial C_{v,res}T}{\partial t} + \nabla \cdot \left(\sum_j \rho_j C_{pj} T \mathbf{v}_j^D \right) = q_H \tag{4.67}$$

is first tested against an arbitrary piecewise constant function w and integrated over $\mathcal{T}_h$, which gives

$$\begin{aligned} \sum_E \frac{\partial}{\partial t} \int_{\Omega_E} C_{v,res} T d\Omega_E + \sum_E \int_{\Omega_E} \left(\nabla \cdot \left(\sum_j \rho_j C_{pj} T \mathbf{v}_j^D \right) \right) w d\Omega_E \\ = \sum_E \int_{\Omega_E} q_H w d\Omega_E \end{aligned} \tag{4.68}$$

Integration by parts and using divergence theorem and observing that $\nabla w = 0$ in each Ω_E because w is an arbitrary piecewise constant, equation 4.68 can be rewritten as

$$\begin{aligned} \sum_E \frac{\partial}{\partial t} \int_{\Omega_E} C_{v,res} T d\Omega_E + \sum_E \int_{\partial\Omega_E} \left(\sum_j \rho_j C_{pj} T \mathbf{v}_j^D \cdot \mathbf{n} \right) d\partial\Omega_E \\ = \sum_E \int_{\Omega_E} q_H d\Omega_E \end{aligned} \tag{4.69}$$

On each finite element Ω_E, approximating the time derivative by finite difference leads to [126]

$$\begin{aligned} \bar{H}_E &= H_E^l - \Delta t^{l+1} \int_{\Omega_E} \sum_j \left(C_{pj} T \right)^{l,HG} \rho_j^{l+1/2,HG} \mathbf{v}_j^{D,l+1/2} \cdot \mathbf{n} d\partial\Omega_E \\ &+ \Delta t^{l+1} \int_{\Omega_E} q_H^{l+1/2} d\Omega_E \end{aligned} \tag{4.70}$$

where $H_E = \int_{\Omega_E} C_{v,res} T d\Omega_E$ is the total thermal energy in Ω_E, $\bar{H}_E$ is the intermediate value for H_E^{l+1} obtained from the convection step,

$$(C_{pj}T)^{l,HG} \rho_j^{l+1/2,HG} \mathbf{v}_j^{D,l+1/2} \cdot \mathbf{n}$$

is the numerical flux approximation obtained from the higher-order Godunov scheme, and $\Delta t^{l+1} = t^{l+1} - t^l$. Following the heat convection solve, the heat conduction step solves

$$H_E^{l+1} - \Delta t^{l+1} \int_{\partial\Omega^E} \lambda_T \nabla T^{l+1} \cdot \mathbf{n} d\partial\Omega_E = \Delta t^{l+1} \bar{H}_E \tag{4.71}$$

Equation 4.71 is discretized by MFE on RT_0 element in space, the same one used for solving the compositional flow pressure equation in Section 4.2. Backward Euler scheme is used for implicit time stepping.

The procedure for solving the thermal energy balance equation is repeated until T^{n+1} is obtained. The updated temperature solution T^{n+1} is then used for coupled compositional flow and geomechanics calculation for t^{n+2}, the next time step. More specifically, flash and fluid property calculation for t^{n+2} is based on T^{n+1} in compositional flow model; for the linear elasticity model to solve $\mathbf{u}^{n+2}$, T^{n+1} is applied as an external load through the total stress relation in equation 3.14. Note that because of the explicit coupling between the thermal energy model and the poroelasticity model, T is kept constant during the fixed-stress iterative coupling update between the compositional flow and the elasticity models. Figure 4.22 illustrates the procedure of the iterative-explicit coupling between the compositional flow, linear elasticity, and thermal energy balance models in IPARS.

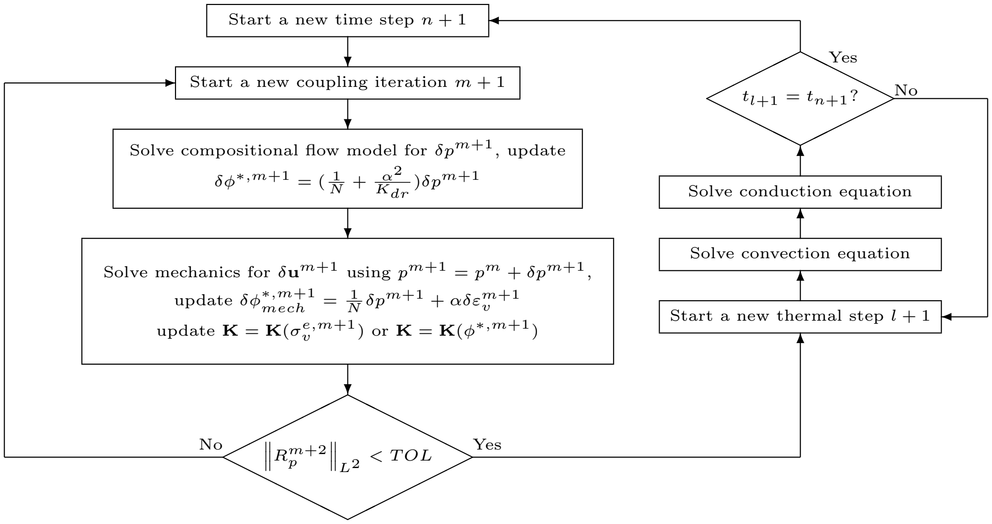

Figure 4.22: Thermoporoelasticity coupling procedure

4.4.2 Numerical Example

In this section we present a synthetic case of a thermoporoelastic process to illustrate the thermal effect on the reservoir skeleton deformation. The model is a quarter of a 5-spot injection-production problem, with the injector continuously injecting cold water into a hot water aquifer. The problem is set up in this way to study the competition between the compression and the dilation of the reservoir matrix due to the cooling effect of the injected cold water and the pressure load from the injection, respectively. No-flow and zero heat loss boundary conditions are assumed for compositional flow and thermal energy balance models, respectively. A compressive overburden stress of 8500 psi is prescribed on the top surface for the geomechanics model. Zero normal displacement and zero shear traction boundary conditions are enforced on all other surfaces. Parameters for the numerical model are summarized in Table

SYMBOL	QUANTITY	VALUE
t^T	total simulation time	1000.1 days
LX	reservoir dimension in x	100 ft
LY	reservoir dimension in y	3500 ft
LZ	reservoir dimension in z	3500 ft
NX	number of grids in x	6 (2×10, 2×15, 2×25)
NY	number of grids in y	35
NZ	number of grids in z	35
d	depth of reservoir top surface	8225 ft
T	initial reservoir temperature	160 °F
p_0	initial pressure	4000.0 psi
k	permeability in x,y, and z directions	1000 md
ϕ_0	initial porosity	0.38
E	Young's modulus	1.45 $\times 10^6$ psi
ν	Poisson's ratio	0.28
ρ_s	rock mass density	2.65 g/cm^3
$C_{v,s}$	rock isochoric specific heat capacity	0.2 BTU/LB-°F
α	Biot's constant	1.0
σ_{ob}	compressive overburden stress	8500 psi
α^T	solid skeleton thermal expansion coefficient	1.667×10^{-5} 1/°F
Q_{inj}	constant water injection rate	10000 BBL/day
T_{src}	temperature of the injected water	60 °F
Q_{prod}	constant water production rate	8000 BBL/day

Table 4.5: Parameters for cold water injection case

4.5.

Results from three simulations, one with isothermal condition, one with higher-order Godunov for heat convection, and one with first-order Godunov for heat convection, are compared. Heat conduction is ignored in all of the three cases. Figures 4.23–4.26 are vertical displacement fields at 0.1 day and 1000.1 day for the isothermal case and the thermal case with higher-order Godunov method, respectively. At 0.1 day, the vertical displacement fields from the two simulations are almost identical (Figures 4.23–4.24), whereas at 1000.1 day, they differ from each other (Figures 4.25–4.26). For the isothermal case, the near uniform vertical displacement at the top surface at 1000.1 day indicates that the vertical displacement of the reservoir is mostly driven by the overburden compressive stress but not the pressure gradient inside the reservoir. This is verified in Figures 4.27 and 4.28 that the pressure gradients at 1000.1 day are small for both cases, due to the high permeability (1000 md) in the reservoir. Larger vertical displacement (subsidence) around the injection well at 1000.1 day in Figure 4.26 is caused by the injected cold water which cools the solid skeleton and induces compressive thermal strain. The dominance of the thermal effect in inducing reservoir deformation is evident by comparing the displacement and the temperature fields at 1000.1 day in Figures 4.26 and 4.29.

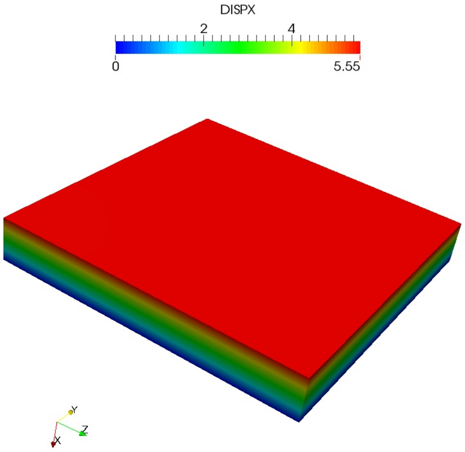

Figure 4.23: X-displacement at 0.1 days for isothermal case

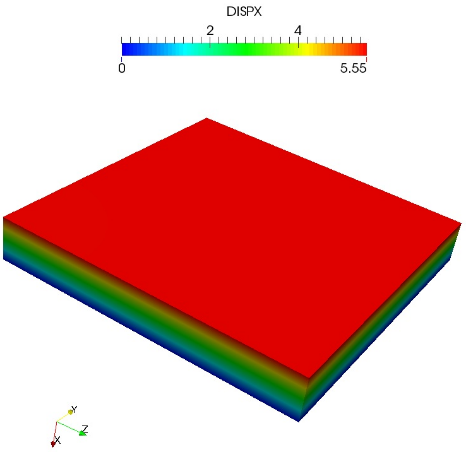

Figure 4.24: X-displacement at 0.1 days for thermal case with higher-order Godunov method

The advantage of using the higher-order Godunov method over the

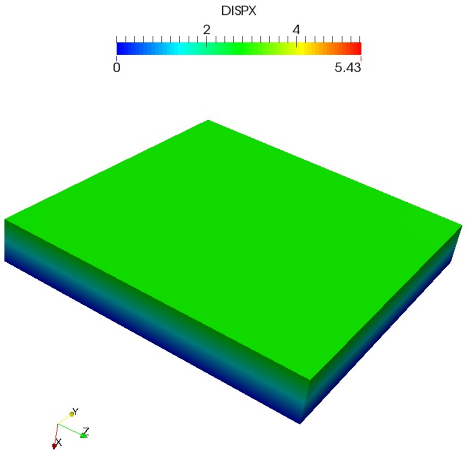

Figure 4.25: X-displacement at 1000.1 days for isothermal case

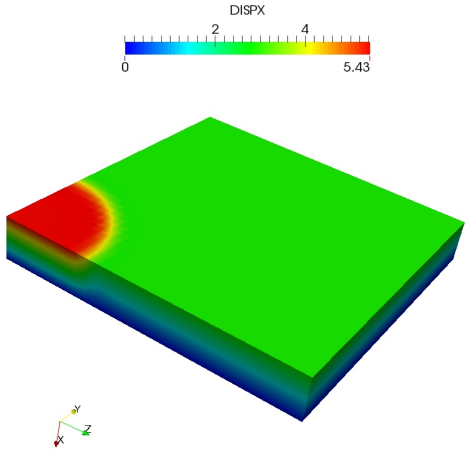

Figure 4.26: X-displacement at 1000.1 days for thermal case with higher-order Godunov method

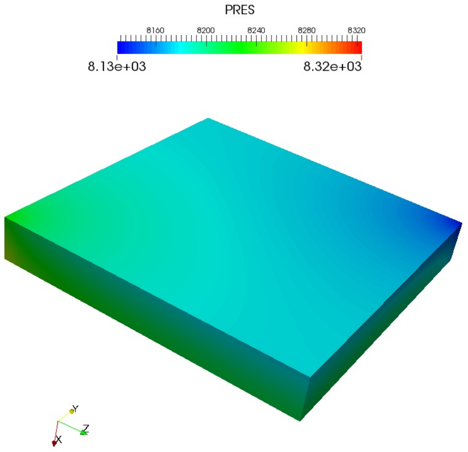

Figure 4.27: Pressure at 1000.1 days for isothermal case

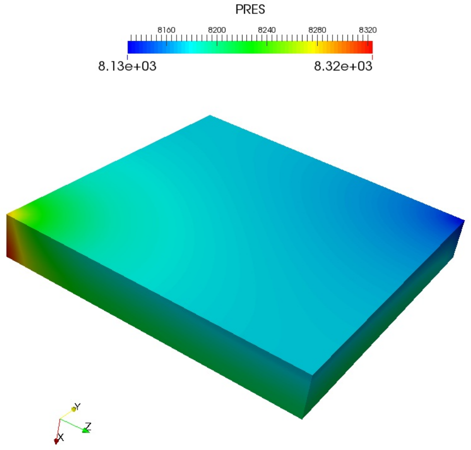

Figure 4.28: Pressure at 1000.1 days for thermal case with higher-order Godunov method

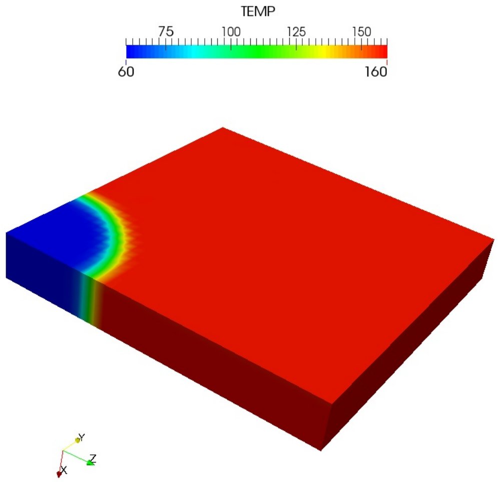

Figure 4.29: Temperature field at 1000.1 days for thermal case with higher-order Godunov method

first-order Godunov method to capture the sharp temperature front is illustrated in Figures 4.30 and 4.31. With the higher-order Godunov method, the temperature front is less smeared (diffused) than its counterpart from the first-order Godunov method. It should also be pointed out that the cell-centered temperature field is first interpolated to a node-based temperature field and then visualized. Therefore an artificial diffusive zone about the size of a grid cell is seen for the simulation with the higher-order Godunov method.

It is worthwhile to point out that the thermal energy balance model using Godunov methods for heat convection does not work well in multiphase flow scenarios where the concentration/saturation is solved by MFE on rectangular elements with a special quadrature rule, or equivalently, the CCFD method. In other words, solving the flow of mass (concentration/saturation)

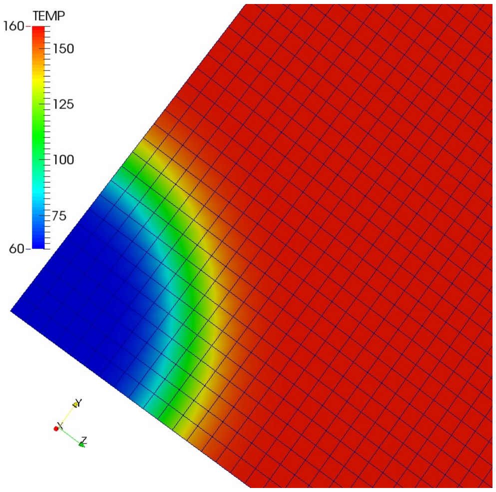

Figure 4.30: Temperature at 1000.1 days with first-order Godunov method

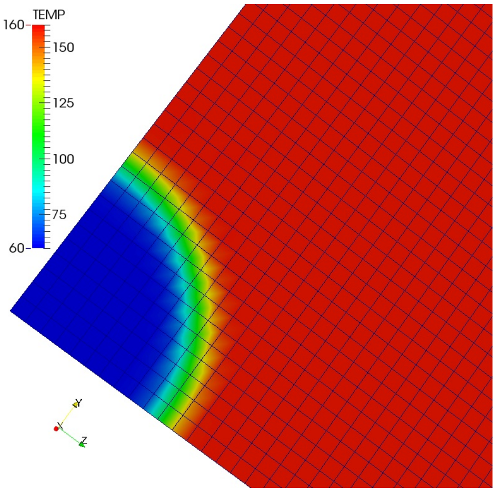

Figure 4.31: Temperature at 1000.1 days with higher-order Godunov method

using CCFD and the flow of thermal energy (temperature) using Godunov methods may yield non-physical numerical solutions. To see this clearly, we reran the thermoporoelasticity case assuming that the reservoir is initially saturated with 100% oil and from $t = 0^+$ cold water is injected into the reservoir. Ten thermal steps are taken within each flow step. The total fluid rate of the production well is 8000 BBL/day. All other parameters are the same as those in Table 4.5.

Figures 4.32–4.33 show water saturation and temperature profiles at 1000.1 days from the simulation with the first-order Godunov method for heat convection. The saturation front is smeared over a large domain. In the zone with the smeared saturation front, the fluid temperature is above 160 °F which is non-physical. Figures 4.34–4.35 are water saturation and temperature profiles at 1000.1 days from the simulation with a higher-order Godunov method for heat convection. The fluid temperature in the zone of the smeared saturation front is also above 160 °F. The maximum temperature is about 173 °F for the simulation with a higher-order Godunov method, which is higher than the maximum temperature of about 168 °F from the simulation with the first-order Godunov method. The fact that both first-order Godunov and higher-order Godunov methods for heat convection produce non-physical temperature in the zone with the smeared saturation front indicates that we need also use Godunov methods to solve the concentration/saturation equation when the thermal energy balance model is coupled to multiphase flows.

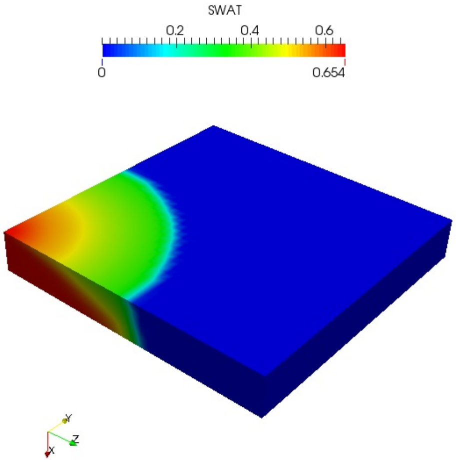

Figure 4.32: Water saturation at 1000.1 days with first-order Godunov method

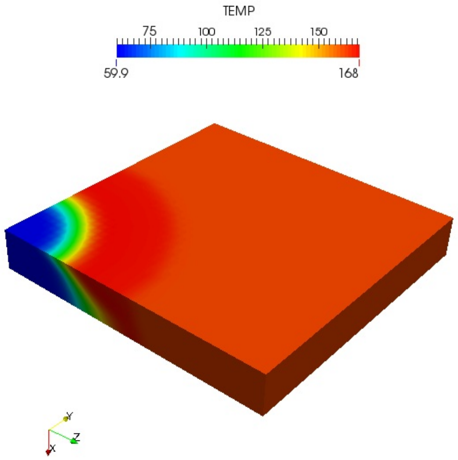

Figure 4.33: Two-phase temperature at 1000.1 days with first-order Godunov method

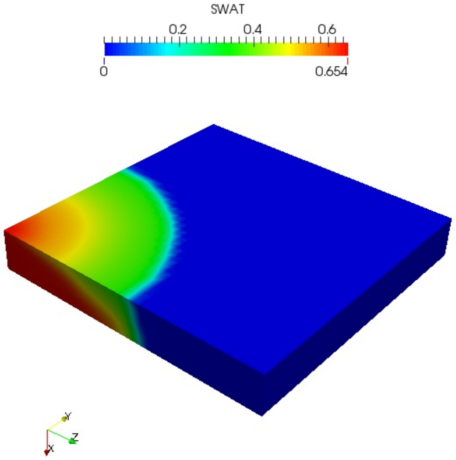

Figure 4.34: Water saturation at 1000.1 days with higher-order Godunov method

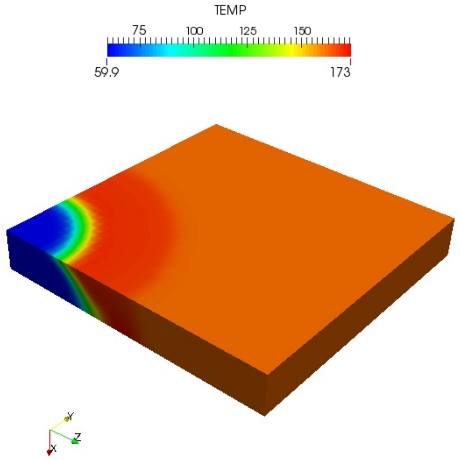

Figure 4.35: Two-phase temperature at 1000.1 days with higher-order Godunov method

4.5 Geomechanics Coupled with DOECO2

In this section, we discuss the coupling of the linear elasticity model with DOECO2, a compositional gas reservoir simulator developed at the Department of Petroleum and Geosystems Engineering at the University of Texas at Austin. DOECO2 is an isothermal compositional simulator for miscible gas flooding [30, 96]. It is based on the Acs compositional flow formulation [4] which is a non-iterative implicit pressure explicit saturation (IMPES) type formulation. DOECO2 is capable of three-phase (a non-aqueous gas phase and two non-aqueous liquid phases) flash calculation [30]. It includes general three-phase relative permeability models with hysteresis [12] and two foam models for foam flooding simulation [11]. We add the linear elasticity model presented in Chapter 3 (without the thermal effect) as a module to DOECO2 to account for geomechanical effects in EOR or CO_2 sequestration processes.

Define $\bar{N}_i = V_b \phi \sum_j \rho_j S_j \xi_i^j$ as the total number of moles for component i in a grid block/element. Multiplying the component molar mass conservation equation 4.15 by the reference bulk volume V_b^0 and noticing $V_b = V_b^0(1 + \varepsilon_v)$ yields the component mass conservation equation in the coupled poroelasticity model used by DOECO2

$$\frac{\partial \bar{N}_i}{\partial t} + V_b^0 \nabla \cdot \sum_j (\rho_j \xi_i^j \mathbf{v}_j^D) = V_b^0 q_i \tag{4.72}$$

As mentioned before, DOECO2 uses the non-iterative IMPES type Acs formulation to solve the compositional flow equation. Following the procedure outlined by Chang [30], we can derive a single pressure equation from the N_c+1 mass conservation equations by assuming that the pore volume is always fully saturated by fluids, i.e.

$$V_t(p,\ \bar{N}_1,\ \cdots,\ \bar{N}_{N_c+1}) = V_p(p) \tag{4.73}$$

where V_t is the total fluid volume and V_p is the pore volume at the deformed configuration. Defining $\bar{V}_{ti} = \left(\frac{\partial V_t}{\partial \bar{N}_i}\right)_{p, \bar{N}_{k(k \neq i)}}$, differentiating equation 4.73 with respect to time gives

$$\left(\frac{\partial V_t}{\partial p}\right)_{\bar{N}_i} \left(\frac{\partial p}{\partial t}\right) + \sum_i \bar{V}_{ti} \left(\frac{\partial \bar{N}_i}{\partial t}\right) = \frac{\partial V_p}{\partial t} \tag{4.74}$$

Then the pressure equation can be obtained by substituting equation 4.72 into

4.74 and using $p_j = p + p_{cj}$

$$\begin{aligned} & \frac{\partial V_p}{\partial t} - \frac{\partial V_t}{\partial p}\frac{\partial p}{\partial t} - V_b^0 \sum_i \bar{V}_{ti} \nabla \cdot \sum_j \mathbf{K} \frac{k_{rj}}{\mu_j} \rho_j \xi_i^j \nabla p \\ = \quad & V_b^0 \sum_i \bar{V}_{ti} \nabla \cdot \sum_j \mathbf{K} \frac{k_{rj}}{\mu_j} \rho_j \xi_i^j \left(\nabla p_{cj} - \rho_j \mathbf{g} \right) + V_b^0 \sum_i \bar{V}_{ti} q_i \end{aligned} \quad (4.75)$$

DOECO2 solves the pressure equation 4.75 by treating pressure related terms in the LHS of 4.75 implicitly and saturation related terms in the LHS of 4.75 explicitly [30]. All terms except the source/sink terms in the RHS of 4.75 are treated explicitly. The solution of the pressure equation 4.75 is non-iterative which means 4.75 is solved only once at each time step. The volume error from n^{th} time step is supplied as a source/sink term in the RHS of 4.75 for $(n+1)^{th}$ time step. In other words, the volume error from 4.75 is corrected at the next time step. Due to the non-iterative solution procedure, smaller time steps are usually required by the Acs formulation to produce similarly accurate solutions compared to the iterative IMPES or IMPEC formulations. We adopt the fixed-stress split to solve the compositional flow and linear elasticity models in DOECO2 sequentially, but not iteratively. Since

$$V_p = V_b^0 \phi^* = V_b^0 \left(\phi^0 + \alpha \varepsilon_v + \frac{1}{N} p \right), \quad (4.76)$$

with the fixed-stress assumption 4.47, the pressure equation 4.75 can be written as

$$
\begin{aligned}
& \left(V_p^0\left(\frac{1}{N\phi^0}+\frac{3\alpha^2}{\phi^0(3\lambda+2G)}\right)-\frac{\partial V_t}{\partial p}\right)^n \frac{\partial p^{n+1}}{\partial t} \\
& -V_b^0\left(\sum_i \bar{V}_{ti}\nabla\cdot\sum_j \mathbf{K}\frac{k_{rj}}{\mu_j}\rho_j\xi_i^j\right)^n \nabla p^{n+1} \\
= \quad & V_b^0\left(\sum_i \bar{V}_{ti}\nabla\cdot\sum_j \mathbf{K}\frac{k_{rj}}{\mu_j}\rho_j\xi_i^j\right)^n \left(\nabla p_{cj}^n-\rho_j^n\mathbf{g}\right) \\
& +V_b^0\sum_i \bar{V}_{ti}^n q_i^{n+1}-V_b^0\frac{3\alpha}{3\lambda+2G}\frac{\partial {\sigma_v}^n}{\partial t} \qquad (4.77)
\end{aligned}
$$

Equation 4.77 does not depend on the displacement solution $\mathbf{u}^{n+1}$ so p^{n+1} is solved. Subsequently the linear elasticity model (equations 3.2, 3.3, and 3.14 for the isothermal condition) is solved for $\mathbf{u}^{n+1}$ using p^{n+1}. The volume error results from the fixed-stress assumption is

$$
V_b^0\left(\phi_{mech}^{*,n+1}-\phi^{*,n+1}\right)=V_b^0\frac{\alpha}{K_{dr}}\delta\sigma_v^{n+1} \qquad (4.78)
$$

and it is corrected at $(n+2)^{th}$ time step.

4.5.1 Numerical Examples

The first numerical example is a single well production problem. It is used to verify the coupled poroelasticity model in DOECO2 by comparing the simulation results with IPARS and CMG GEM [82]. The reservoir is square and saturated with single phase C_{10}. One BHP specified production well is drilled through the center of the reservoir. The compositional flow model adopts no-flow boundary conditions on all of the six boundary faces. For the linear elasticity model, zero normal displacement and zero shear traction

SYMBOL	QUANTITY	VALUE
X_L	dimension in x	1680 ft
Y_L	dimension in y	1680 ft
Z_L	dimension in z	60 ft
DX	grid size in x	80 ft
DY	grid size in y	80 ft
DZ	grid size in z	20 ft
N_c	number of hydrocarbon component	1: C_{10}
k_{xx}	permeability in x	10 md
k_{yy}	permeability in y	10 md
k_{zz}	permeability in z	10 md
ϕ_0	initial porosity	0.2
c_r (decoupled flow model)	formation compressibility	3.0×10^{-6} 1/psi
p_0	initial pressure	1500 psi
N_w	number of well	1: production well
r_w	well radius	1 ft
BHP	BHP of production well	1200 psi
E	Young's modulus	1.0×10^6 psi
ν	Poisson's ratio	0.3
α	Biot's constant	1.0
ρ_s	rock density	165 lb_m/ft^3
D_{top}	depth of reservoir top surface	0 ft
t^T	total simulation time	500 days

Table 4.6: Parameters for single well production example

boundary conditions are applied on all of the four lateral boundary faces and the bottom boundary face. Zero shear traction and a compressive normal stress of 13.88 psi are applied on the top boundary face of the reservoir. Model parameters for the single well production problem are summarized in Table 4.6. For the comparison between DOECO2 and IPARS, the oil phase viscosity is calculated in the programs using the Lohrenz-Bray-Clark correlation [80]; for the comparison between DOECO2 and CMG GEM, the oil phase viscosity is set to a constant $\mu = 4.3492$ cp. Note that in DOECO2, z-direction is the vertical direction.

Figures 4.36 and 4.37 are the comparison results of oil production rates between DOECO2 and IPARS, and between DOECO2 and CMG GEM, respectively. We see that for the decoupled compositional flow problem, the oil production rate curve from DOECO2 matches its counterparts from both IPARS and CMG GEM. When the geomechanics coupling is considered, the oil production rate curve from DOECO2 still matches the IPARS result very well because the same linearized reservoir porosity expression 4.28 (with the isothermal condition) is used in these two simulators. However, the oil production rate curves from DOECO2 and CMG GEM do not match each other when geomechanical effects are accounted. The reason is that CMG GEM uses a different reservoir porosity formula [82, 131]. With the isothermal assumption, it is written as

$$\phi^{*,m+1} = \phi^{*,m} + (c_0 + c_1 a_1)(p^{m+1} - p^m) \tag{4.79}$$

where

$$c_0 = \frac{1}{V_b^0}\left(\frac{dV_p}{dp} + \frac{V_b \alpha}{K_{dr}}\frac{d\sigma_v}{dp}\right) \tag{4.80}$$

$$c_1 = -\frac{V_b}{V_b^0}\frac{\alpha}{K_{dr}} \tag{4.81}$$

$$a_1 = \text{factor}\left\{\frac{2}{9}\frac{E}{(1-\nu)}\frac{\alpha}{K_{dr}}\right\} \tag{4.82}$$

The second example is a field scale CO_2 flooding EOR simulation. The reservoir is of size 39600 ft × 4150 ft × 12.32 ft. Eight non-aqueous components exist in the reservoir. Twenty two wells are drilled to simulate five horizontal wells, out of which three are injection wells and two are production

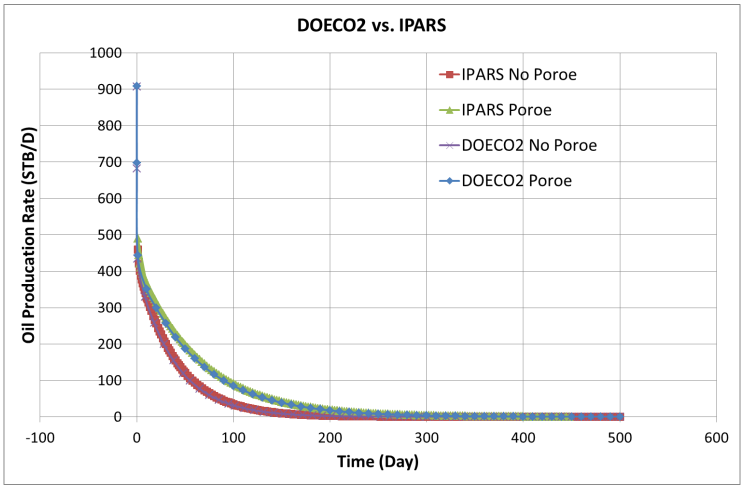

Figure 4.36: Oil production rate comparison between DOECO2 and IPARS

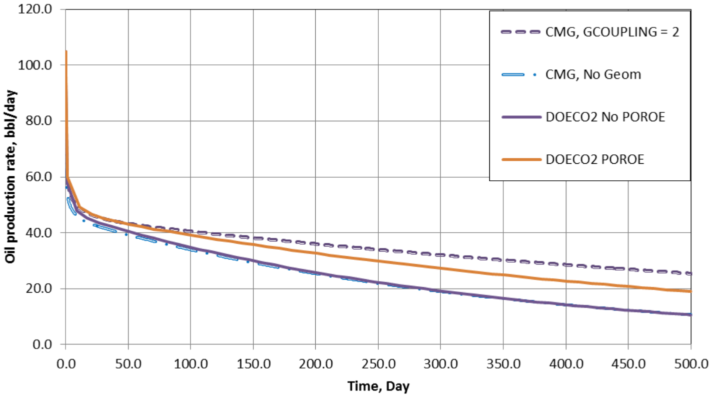

Figure 4.37: Oil production rate comparison between DOECO2 and CMG

SYMBOL	QUANTITY	VALUE
X_L	dimension in x	39600 ft
Y_L	dimension in y	4150 ft
Z_L	dimension in z	12.32 ft
DX	grid size in x	200 ft
DY	grid size in y	50 ft
DZ	grid size in z	2×2.04 ft, 2×4.12 ft
N_c	# non-aqueous components	8: CO_2, N_2O_1, C_{2+}, C_{4+}, C_{7+}, C_{10+}, C_{14+}, C_{20+}
N_w	# horizontal wells	5: 3 injection wells and 2 production wells
ϕ_0	initial porosity	0.2
E	Young's modulus	1.0×10^6 psi
ν	Poisson's ratio	0.3
α	Biot's constant	1.0
ρ_s	rock density	165 lb_m/ft^3
D_{top}	depth of reservoir top surface	about 6000 ft
t^T	total simulation time	1825 days

Table 4.7: Parameters for CO_2 flooding EOR simulation

wells. No-flow boundary conditions are prescribed on all of the six boundary faces for the compositional flow model. Zero shear traction and a compressive normal stress of 6500 psi are applied on the top boundary face of the reservoir. All the other five boundary faces have zero normal displacement and zero shear traction boundary conditions for the linear elasticity model. Table 4.7 lists model parameters for the CO_2 flooding EOR simulation.

Figures 4.38–4.41 show the profiles of pressure, CO_2 concentration, and effective horizontal stresses σ^e_{xx} and σ^e_{yy} at 1825 days, respectively. Comparing the pressure profile with the effective horizontal stresses profiles, it is clear that the rock surrounding the injection wells is experiencing tensile effective stresses whereas the rock surrounding the production wells is experiencing compressive effective stresses. The magnitude of the tensile effective stresses can be employed to indicate where is most likely the zone a fracture is going to initiate. Figures 4.42 and 4.43 compare the gas and oil production rates with and without geomechanics coupling for Well 22 which is a section of the horizontal production well in the upper right part of the reservoir in Figure 4.38. With the geomechanics coupling, the compaction-driven productivity enhancement is significant for the gas phase but not for the oil phase.

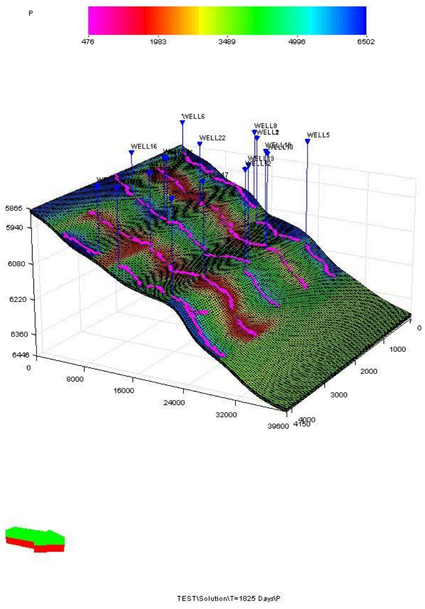

Figure 4.38: CO_2 flooding EOR simulation: pressure at 1825 days

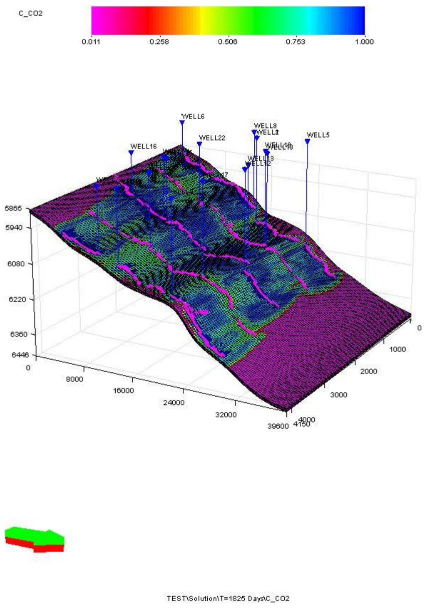

Figure 4.39: CO_2 flooding EOR simulation: CO_2 concentration at 1825 days

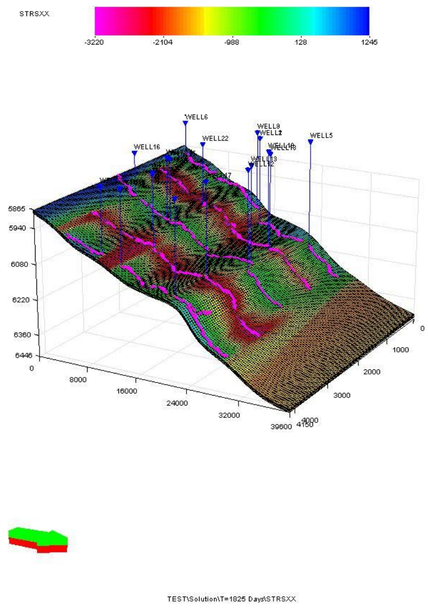

Figure 4.40: CO_2 flooding EOR simulation: σ^e_{xx} at 1825 days

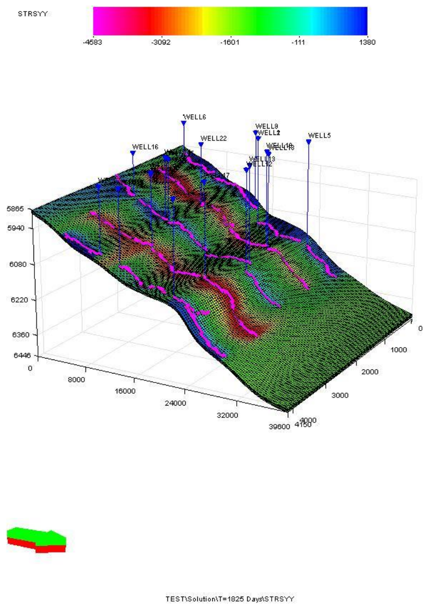

Figure 4.41: CO_2 flooding EOR simulation: σ^e_{yy} at 1825 days

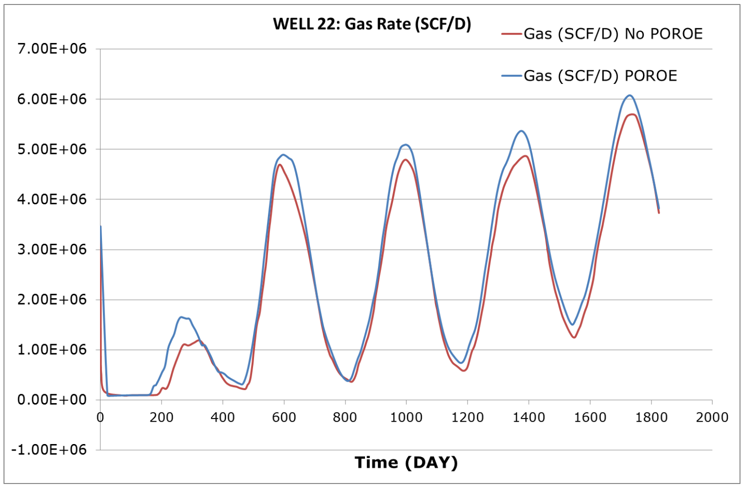

Figure 4.42: CO_2 flooding EOR simulation: gas production rate for Well 22

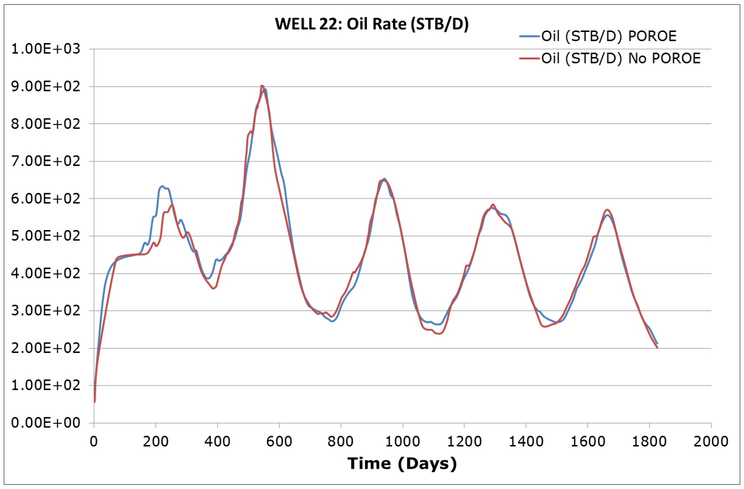

Figure 4.43: CO_2 flooding EOR simulation: oil production rate for Well 22

Chapter 5

Geomechanics Coupled with Multipoint Flux Mixed Finite Element Flow Model

5.1 Introduction

Wheeler and Yotov [145, 146] introduced the multipoint flux mixed finite element method (MFMFE) for solving second order elliptic Darcy flow problems on quadrilateral and simplicial grids in 2006. The development of MFMFE was motivated by the multipoint flux approximation method (MPFA) [1] in which the sub-edge fluxes are eliminated to form a cell-centered pressure system. Using the lowest order Brezzi-Douglas-Marini (BDM) [24] approximating space and a special symmetric quadrature rule, MFMFE also eliminates the sub-edge velocities and generates a symmetric and positive definite (SPD) cell-centered pressure system. Under the variational MFE framework, Wheeler and Yotov [146] also proved first order convergence for pressure and velocity using MFMFE.

Following their work, Ingram et al. [64] extended MFMFE to h^2-perturbed hexahedral elements by employing an enhanced lowest order Brezzi-Douglas-Durán-Fortin (BDDF) approximating space with a similar symmetric quadrature rule in [146] and provided a-priori error estimates of first order convergence for pressure and velocity. A special non-symmetric quadrature rule was then developed by Wheeler et al. [142] for MFMFE to be applicable to general distorted hexahedra and quadrilaterals and first order convergence of pressure and velocity was also obtained. Furthermore, Wheeler et al. [144] theoretically showed first order convergence in space and time for pressure, velocity, and displacement for a coupled MFMFE flow with CG linear elasticity model on distorted quadrilaterals and hexahedra and provided numerical verifications on quadrilateral grids.

MFMFE has several appealing merits for modeling fluid flow in porous media. As an MFE method, MFMFE is locally mass conservative. It can handle full permeability tensors which is desirable because in practical problems the principal directions of permeability tensors are not always aligned with the coordinate axes. Discontinuous permeabilities can be well treated due to the harmonic averaging of the permeability coefficient in the formulation. The flexibility of MFMFE in handling general distorted hexahedra and boundary conditions make it suitable for modeling realistic reservoirs with complex geometry and faults. Moreover, MFMFE reduces the mixed formulation to a cell-centered pressure system which is easier to solve than the saddle-point type pressure-velocity system. Since the introduction of the MFMFE method, it has been applied to solving single phase slightly compressible flow and two-phase oil-water flow [137, 138] and has been coupled with CG linear elasticity on general hexahedral grids in IPARS [90]. Fracture flow models using mimetic finite difference (MFD) [5] and MFMFE [117] have been coupled to the MFMFE reservoir flow model by adding extra velocity degree of freedom on the internal cell interfaces.

In this chapter we briefly introduce the MFMFE formulation for a steady Darcy flow model equation and apply it to solve the two-phase oil-water model [137, 138, 142]. The coupling of MFMFE flow model to the linear elasticity model presented in Chapter 3 is discussed. Numerical examples illustrating the poroelasticity model on distorted hexahedral grids are provided.

5.2 Multipoint Flux Mixed Finite Element Method

In this section we summarize the key ingredients of the MFMFE method developed by Wheeler and Yotov [146], Ingram et al. [64], and Wheeler et al. [142, 144]. Our focus is the MFMFE method on distorted hexahedra which is coupled to the CG linear elasticity model for three-dimensional reservoir simulation.

Consider the same domain Ω as defined in Chapter 3. For the flow problem, the boundary $\partial\Omega = \Gamma$ is decomposed into two parts:

$$\Gamma = \bar{\Gamma}_D \bigcup \bar{\Gamma}_N, \quad \Gamma_D \bigcap \Gamma_N = \emptyset, \quad \Gamma_D \neq \emptyset \tag{5.1}$$

The model equations consist of Darcy's law, mass conservation equation for steady state and incompressible fluid flow, and boundary conditions:

Model Equation:

$$\begin{aligned}
\mathbf{v}^D &= -\mathbf{K}\left(\nabla p - \rho\mathbf{g}\right) \quad \text{in } \Omega, && (5.2)\\
\nabla\cdot\mathbf{v}^D &= q \quad \text{in } \Omega, && (5.3)\\
p &= p_D \quad \text{on } \Gamma_D, && (5.4)\\
\mathbf{v}^D\cdot\mathbf{n} &= 0 \quad \text{on } \Gamma_N. && (5.5)
\end{aligned}$$

where $\mathbf{K}$ can be a symmetric full tensor, p_D is the prescribed pressure boundary condition, and ρ is fluid mass density.

The weak formulation of the model problem reads: find $\mathbf{v}^D \in H(div;\Omega)$ and $p \in L^2(\Omega)$ such that

$$\begin{aligned}
(\mathbf{K}^{-1}\mathbf{v}^D,\mathbf{v}) - (p,\nabla\cdot\mathbf{v}) &= (\rho\mathbf{g},\mathbf{v}) && (5.6)\\
(\nabla\cdot\mathbf{v}^D, w) &= (q,w) && (5.7)
\end{aligned}$$

hold for $\forall\mathbf{v} \in H(div;\Omega)$ and $\mathbf{v} = 0$ on Γ_N, and $\forall w \in L^2(\Omega)$, where

$$H(div;\Omega) = \left\{\mathbf{v} \in (L^2(\Omega))^3 : \nabla\cdot\mathbf{v} \in L^2(G)\right\} \tag{5.8}$$

and $(\cdot,\cdot)$ represents the L^2 inner product. The divergence theorem is used in the derivation of equation 5.6.

Mixed Finite Element Space:

We assume the finite element partition of domain Ω is also $\mathcal{T}_h$, the same one for the linear elasticity model in Chapter 3. For each finite element $E \in \mathcal{T}_h$, the same trilinear finite element mapping F_E defined in Chapter 3 is used to map a unit cube $\hat{E}$ in the reference space to the physical element E. By the definition of the mapping F_E, a relation between the face unit outward normals for the physical element and the reference element can be obtained [64, 142]

$$\mathbf{n}_i = \frac{1}{J_{e_i}} J_E (DF_E^{-1})^T \hat{\mathbf{n}}_i, \quad J_{e_i} = |J_E (DF_E^{-1})^T \hat{\mathbf{n}}_i| \tag{5.9}$$

where $\mathbf{n}_i$ is the unit outward normal for face $e_i \subset E$ and $\hat{\mathbf{n}}_i$ is the unit outward normal for $\hat{e}_i \subset \hat{E}$. Note that $\hat{\cdot}$ denotes a quantity in the reference space. On the reference cube $\hat{E}$, the velocity space $\hat{\mathbf{V}}(\hat{E})$ and the pressure space $\hat{W}(\hat{E})$ are defined as [64]

$$\begin{aligned} \hat{\mathbf{V}}(\hat{E}) = \mathrm{BDDF}_1(\hat{E}) &+ r_2 \mathrm{curl}(0, 0, \xi^2\zeta)^T + r_3 \mathrm{curl}(0, 0, \xi^2\eta\zeta)^T \\ &+ s_2 \mathrm{curl}(\xi\eta^2, 0, 0)^T + s_3 \mathrm{curl}(\xi\eta^2\zeta, 0, 0)^T \\ &+ t_2 \mathrm{curl}(0, \eta\zeta^2, 0)^T + t_3 \mathrm{curl}(0, \xi\eta\zeta^2, 0)^T, \\ \hat{W}(\hat{E}) &= P_0(\hat{E}). \end{aligned} \tag{5.10}$$

And the BDDF_1 space on $\hat{E}$ is given by [23]

$$\begin{aligned} \mathrm{BDDF}_1(\hat{E}) = (P_1(\hat{E}))^3 &+ r_0 \mathrm{curl}(0, 0, \xi\eta\zeta)^T + r_1 \mathrm{curl}(0, 0, \xi\eta^2)^T \\ &+ s_0 \mathrm{curl}(\xi\eta\zeta, 0, 0)^T + s_1 \mathrm{curl}(\eta\zeta^2, 0, 0)^T \\ &+ t_0 \mathrm{curl}(0, \xi\eta\zeta, 0)^T + t_1 \mathrm{curl}(0, \xi^2\zeta, 0)^T. \end{aligned} \tag{5.11}$$

In 5.10 and 5.11, $(P_n(\hat{E}))^3$ is the space of three-dimensional polynomials of degree $\leq n$ on $\hat{E}$, and r_j, s_j, and t_j for $j = 0, 1, 2, 3$ are real constants. $\mathrm{curl}\hat{\mathbf{a}} = \hat{\nabla} \times \hat{\mathbf{a}}$. From the identity

$$\hat{\nabla} \cdot \hat{\nabla} \times \hat{\mathbf{a}} = 0 \tag{5.12}$$

we have

$$\hat{\nabla} \cdot \hat{\mathbf{V}}(\hat{E}) = \hat{\nabla} \cdot (P_1(\hat{E}))^3 = P_0(\hat{E}) = \hat{W}(\hat{E}) \tag{5.13}$$

The dimension of the enhanced BDDF$_1$ space in equation 5.10 is 24. A hexahedron (or the unit cube in the reference space) has six faces and each face has four vertices. Normal flux at each vertex of each face in $\hat{E}$ is chosen to be the degree of freedom of the velocity function in $\hat{\mathbf{V}}(\hat{E})$. See Figure 5.1 for a schematic of the velocity shape functions associated with each vertex in the unit cube $\hat{E}$ and the physical element E. $\hat{\mathbf{v}}_{ij}$ is the velocity shape function associated with vertex $\hat{\mathbf{r}}_i$ and in the direction of $\hat{\mathbf{n}}_j$. Note that by definition

$$\hat{\mathbf{v}}_{ij}(\hat{\mathbf{r}}_i) = \hat{\mathbf{n}}_j \text{ for } i = 1, \cdots, 8 \text{ and j=1,2,3 and } \hat{\mathbf{v}}_{ij}(\hat{\mathbf{r}}_k) = 0 \text{ for } i \neq k \tag{5.14}$$

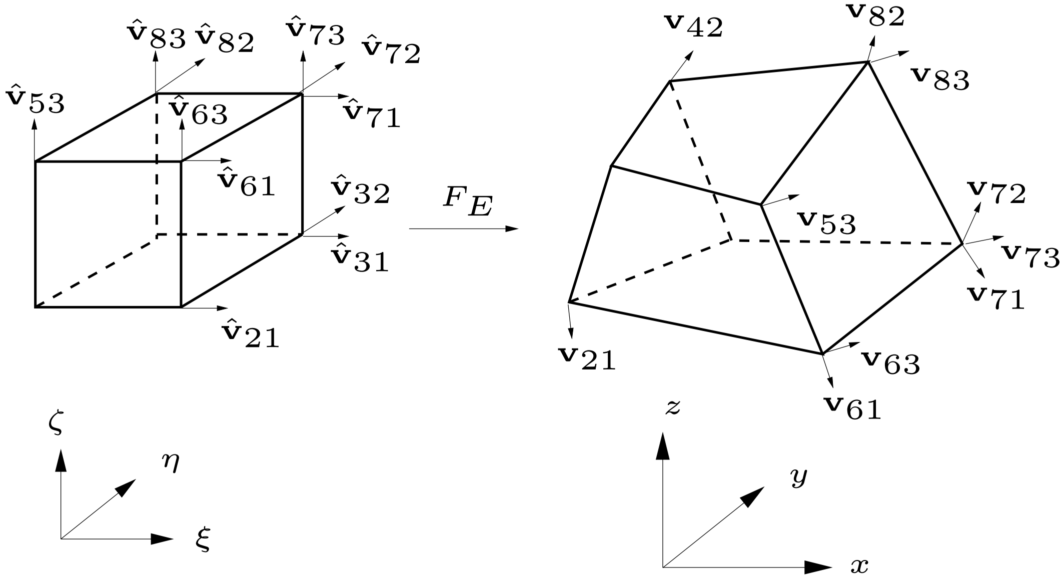

Figure 5.1: Velocity shape functions on a hexahedron

Velocity on a physical element is defined via the Piola transformation:

$$\mathbf{v} \leftrightarrow \hat{\mathbf{v}} : \mathbf{v} = \frac{1}{J_E} DF_E \hat{\mathbf{v}} \circ F_E^{-1}, \tag{5.15}$$

and pressure is defined by

$$w \leftrightarrow \hat{w} : w = \hat{w} \circ F_E^{-1}. \tag{5.16}$$

where F_E^{-1} is the inverse mapping of F_E. Several important relations derived from the definition of the transformation and the finite element mapping F_E are:

$$
\begin{aligned}
(\nabla \cdot \mathbf{v}, w)_E &= (\hat{\nabla} \cdot \hat{\mathbf{v}}, \hat{w})_{\hat{E}} && (5.17)\\
\langle \mathbf{v} \cdot \mathbf{n}_e, w \rangle_e &= \langle \hat{\mathbf{v}} \cdot \hat{\mathbf{n}}_{\hat{e}}, \hat{w} \rangle_{\hat{e}} && (5.18)\\
\mathbf{v} \cdot \mathbf{n}_e &= \frac{1}{J_e} \hat{\mathbf{v}} \cdot \hat{\mathbf{n}}_{\hat{e}} \circ F_E^{-1}(\mathbf{x}) && (5.19)\\
\nabla \cdot \mathbf{v} &= \left(\frac{1}{J_E} \hat{\nabla} \cdot \hat{\mathbf{v}} \right) \circ F_E^{-1}(\mathbf{x}) && (5.20)
\end{aligned}
$$

In equation 5.18, $\langle \cdot, \cdot \rangle$ is the L^2 inner product on a face of either the physical or the reference element.

The finite element spaces $\mathbf{V}_h$ and W_h on physical domain $\mathcal{T}_h$ are given by

$$
\begin{aligned}
\mathbf{V}_h &= \left\{ \mathbf{v} \in H(div; \Omega) : \quad \mathbf{v}|_E \leftrightarrow \hat{\mathbf{v}},\ \hat{\mathbf{v}} \in \hat{\mathbf{V}}(\hat{E}), \quad \forall E \in \mathcal{T}_h \right\} \\
W_h &= \left\{ w \in L^2(\Omega) : \quad w|_E \leftrightarrow \hat{w},\ \hat{w} \in \hat{W}(\hat{E}), \quad \forall E \in \mathcal{T}_h \right\}
\end{aligned} \tag{5.21}
$$

The mixed finite element formulation of the model equations 5.2–5.50 reads: find $\mathbf{v}_h^D \in \mathbf{V}_h$ and $p_h \in W_h$ such that

$$
\begin{aligned}
(\mathbf{K}^{-1} \mathbf{v}_h^D, \mathbf{v})_Q - (p_h, \nabla \cdot \mathbf{v}) &= (\rho \mathbf{g}, \mathbf{v}) && (5.22)\\
(\nabla \cdot \mathbf{v}_h^D, w) &= (q, w) && (5.23)
\end{aligned}
$$

hold for $\forall \mathbf{v} \in \mathbf{V}_h$ and $\mathbf{v} = 0$ on Γ_N, and $\forall w \in W_h$. The choice of the quadrature rule $(\mathbf{K}^{-1}\mathbf{v}_h^D, \mathbf{v})_Q$ is a key element in the design of the MFMFE method.

Quadrature Rule

For $\forall \mathbf{a},\ \mathbf{v} \in V_h$, the global quadrature rule is defined as

$$(\mathbf{K}^{-1}\mathbf{a}, \mathbf{v})_Q \equiv \sum_{E \in \mathcal{T}_h} (\mathbf{K}^{-1}\mathbf{a}, \mathbf{v})_{Q,E} \tag{5.24}$$

Using Piola transformation in equation 5.15, the integration on the physical element E can be transformed to an integration on the reference element $\hat{E}$ [142]

$$(\mathbf{K}^{-1}\mathbf{a}, \mathbf{v})_{Q,E} = \left(\frac{1}{J_E} DF_E^T \mathbf{K}^{-1}(F_E(\hat{\mathbf{x}})) DF_E \hat{\mathbf{a}}, \hat{\mathbf{v}} \right)_{\hat{E}} \equiv (\mathcal{M}_E \hat{\mathbf{a}}, \hat{\mathbf{v}})_{\hat{Q},\hat{E}} \tag{5.25}$$

where

$$\mathcal{M}_E(\hat{\mathbf{x}}) = \frac{1}{J_E(\hat{\mathbf{x}})} DF_E^T(\hat{\mathbf{x}}) \mathbf{K}^{-1}(F_E(\hat{\mathbf{x}})) DF_E(\hat{\mathbf{x}}) \tag{5.26}$$

is a symmetric matrix and equation 5.25 is called the symmetric quadrature rule which is accurate for h^2-perturbed hexahedra [64]. In their later paper [142], Wheeler et al. introduced a non-symmetric quadrature rule for accurate pressure and velocity approximation on distorted hexahedra. In the non-symmetric formulation, $\mathcal{M}_E$ is replaced by [142]

$$\widetilde{\mathcal{M}}_E(\hat{\mathbf{x}}) = \frac{1}{J_E(\hat{\mathbf{x}})} DF_E^T(\hat{\mathbf{r}}_{c,\hat{E}}) \overline{\mathbf{K}}_E^{-1} DF_E(\hat{\mathbf{x}}) \tag{5.27}$$

where DF_E^T is evaluated at $\hat{\mathbf{r}}_{c,\hat{E}}$, the center of mass of $\hat{E}$, and $\overline{\mathbf{K}}$ is the mean of $\mathbf{K}$ on physical element E. Generally $\widetilde{\mathcal{M}}_E(\hat{\mathbf{x}})$ is a non-symmetric matrix unless

DF_E is constant over $\hat{E}$. Trapezoidal rule is employed to calculate $(\mathcal{M}_E \hat{\mathbf{a}}, \hat{\mathbf{v}})_{\hat{Q},\hat{E}}$ or $(\widetilde{\mathcal{M}}_E \hat{\mathbf{a}}, \hat{\mathbf{v}})_{\hat{Q},\hat{E}}$. Let $\mathbf{M}_E$ denote either $\mathcal{M}_E$ or $\widetilde{\mathcal{M}}_E$, the trapezoidal quadrature rule reads

$$(\mathbf{M}_E \hat{\mathbf{a}}, \hat{\mathbf{v}})_{\hat{Q},\hat{E}} = \frac{1}{8} \sum_{i=1}^{8} \mathbf{M}_E(\hat{\mathbf{r}}_i) \hat{a}(\hat{\mathbf{r}}_i) \cdot \hat{\mathbf{v}}(\hat{\mathbf{r}}_i) \tag{5.28}$$

From equations 5.14 and 5.28, it is clear that for velocity shape function $\hat{\mathbf{v}}_{ij}$ and $\hat{\mathbf{v}}_{kl}$

$$\begin{aligned} (\mathbf{M}_E \hat{\mathbf{v}}_{ij}, \hat{\mathbf{v}}_{kl})_{\hat{Q},\hat{E}} &= \frac{1}{8} \mathbf{M}_E^{lj}(\hat{\mathbf{r}}_i) \quad \text{if} \quad i = k \\ (\mathbf{M}_E \hat{\mathbf{v}}_{ij}, \hat{\mathbf{v}}_{kl})_{\hat{Q},\hat{E}} &= 0 \quad \text{if} \quad i \neq k \end{aligned} \tag{5.29}$$

where $\mathbf{M}_E^{lj}$ is the l^{th} row, j^{th} column component of the matrix $\mathbf{M}_E$.

Cell-Centered Stencil for Pressure

Because the velocity degrees of freedom are defined at grid vertices in $\mathcal{T}_h$ and the quadrature rule 5.24, 5.28, and 5.29 localizes the interactions between the velocity degrees of freedom to the vertex they are associated, the MFMFE formulation 5.22–5.23 leads to a cell-centered pressure system [64, 142]. To see this more clearly, consider the case that the velocity test functions in equation 5.22 are the velocity basis functions associated with a general vertex (the solid black dot in Figure 5.2) in $\mathcal{T}_h$.

Assume eight hexahedra share the vertex of interest. Twelve velocity basis functions are associated with the vertex on twelve cell interfaces (see Figures 5.3–5.5). For better presentation, the velocity basis functions are

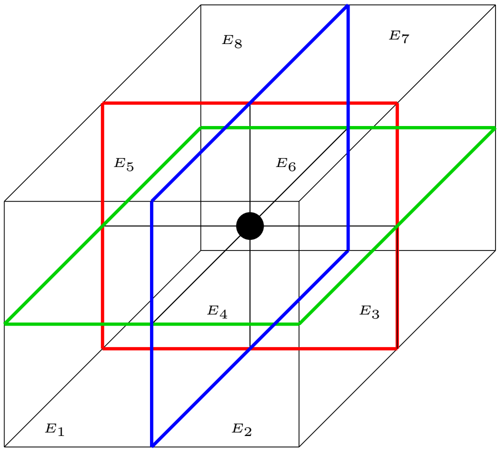

Figure 5.2: Logically structured hexahedral mesh

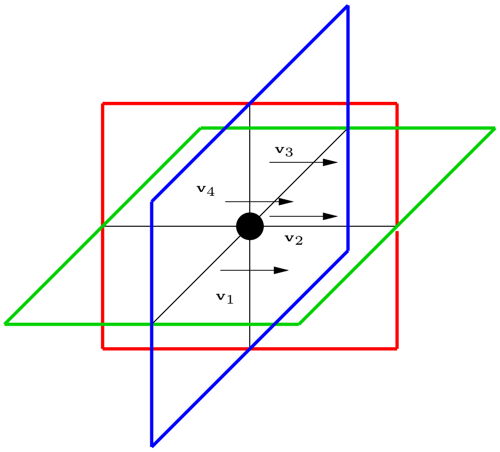

Figure 5.3: $\mathbf{v}_1$–$\mathbf{v}_4$ associated with a vertex

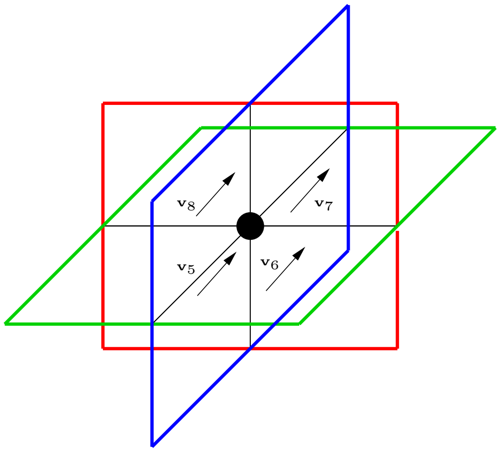

Figure 5.4: $\mathbf{v}_5$–$\mathbf{v}_8$ associated with a vertex

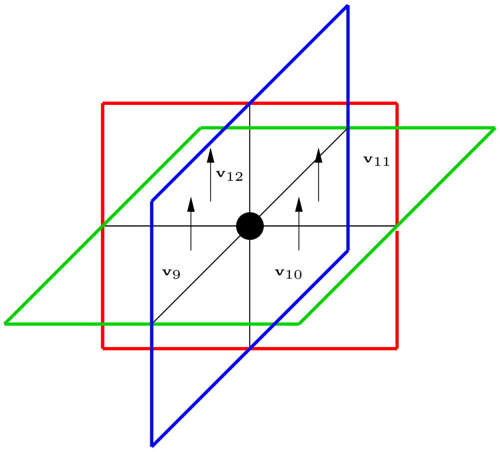

Figure 5.5: $\mathbf{v}_9$–$\mathbf{v}_{12}$ associated with a vertex

plotted away from the vertex. Note that $\mathbf{v}_1$, $\mathbf{v}_2$, $\cdots$, $\mathbf{v}_{12}$ are velocity basis functions in the physical space.

The unknown velocity function $\mathbf{v}_h^D$ can be expressed as

$$\mathbf{v}_h^D = \sum_{i=1}^{nvel} v_{hi}^D \mathbf{v}_i \tag{5.30}$$

and the unknown pressure function p_h as

$$p_h = \sum_{i=1}^{npres} p_{hi} w_i \tag{5.31}$$

where *nvel* is the total number of velocity degrees of freedom and *npres* is the total number of pressure degrees of freedom. Taking $\mathbf{v} = \mathbf{v}_1$ in equation 5.22, and using the quadrature rule 5.24, 5.25, 5.28, and 5.29, we obtain

$$\begin{aligned}
& (\mathbf{K}^{-1}\mathbf{v}_h^D, \mathbf{v}_1)_Q \\
= \; & \sum_E (\mathbf{K}^{-1}\mathbf{v}_h^D, \mathbf{v}_1)_{E,Q} \\
= \; & (\mathbf{K}^{-1}\mathbf{v}_h^D, \mathbf{v}_1)_{E_1,Q} + (\mathbf{K}^{-1}\mathbf{v}_h^D, \mathbf{v}_1)_{E_2,Q} \\
= \; & v_{h1}^D(\mathbf{M}_{E_1}\hat{\mathbf{v}}_1, \hat{\mathbf{v}}_1)_{\hat{Q},\hat{E}} + v_{h5}^D(\mathbf{M}_{E_1}\hat{\mathbf{v}}_5, \hat{\mathbf{v}}_1)_{\hat{Q},\hat{E}} + v_{h9}^D(\mathbf{M}_{E_1}\hat{\mathbf{v}}_9, \hat{\mathbf{v}}_1)_{\hat{Q},\hat{E}} \\
& + v_{h1}^D(\mathbf{M}_{E_2}\hat{\mathbf{v}}_1, \hat{\mathbf{v}}_1)_{\hat{Q},\hat{E}} + v_{h6}^D(\mathbf{M}_{E_1}\hat{\mathbf{v}}_6, \hat{\mathbf{v}}_1)_{\hat{Q},\hat{E}} + v_{h10}^D(\mathbf{M}_{E_1}\hat{\mathbf{v}}_{10}, \hat{\mathbf{v}}_1)_{\hat{Q},\hat{E}} \\
= \; & \frac{1}{8}|e_1| \left(|e_1|\mathbf{M}_{E_1}^{11} v_{h1}^D + |e_5|\mathbf{M}_{E_1}^{12} v_{h5}^D + |e_9|\mathbf{M}_{E_1}^{13} v_{h9}^D \right) \\
& + \frac{1}{8}|e_1| \left(|e_1|\mathbf{M}_{E_2}^{11} v_{h1}^D + |e_6|\mathbf{M}_{E_2}^{12} v_{h6}^D + |e_{10}|\mathbf{M}_{E_2}^{13} v_{h10}^D \right)
\end{aligned} \tag{5.32}$$

$$\begin{aligned}
& (p_h, \nabla \cdot \mathbf{v}_1) \\
= & \sum_E (p_h, \nabla \cdot \mathbf{v}_1)_E \\
= & (p_h, \nabla \cdot \mathbf{v}_1)_{E_1} + (p_h, \nabla \cdot \mathbf{v}_1)_{E_2} \\
= & \langle \mathbf{v}_1 \cdot \mathbf{n}, 1 \rangle_{e_1} p_{h1} + \langle \mathbf{v}_1 \cdot \mathbf{n}, 1 \rangle_{e_2} p_{h2} \\
= & \langle \hat{\mathbf{v}}_1 \cdot \hat{\mathbf{n}}_{e_1}, 1 \rangle_{\hat{e}_1} p_{h1} - \langle \hat{\mathbf{v}}_1 \cdot \hat{\mathbf{n}}_{e_2}, 1 \rangle_{\hat{e}_2} p_{h2} \\
= & \frac{1}{4} |e_1| (p_{h1} - p_{h2}) \qquad (5.33)
\end{aligned}$$

$$\begin{aligned}
& (\rho \mathbf{g}, \mathbf{v}_1) \\
= & \sum_E (\rho \mathbf{g}, \mathbf{v}_1)_E \\
= & (\rho \mathbf{g}, \mathbf{v}_1)_{E_1} + (\rho \mathbf{g}, \mathbf{v}_1)_{E_2} \\
= & \left(\rho \mathbf{g}, \frac{1}{J_{E_1}} DF_{E_1} J_{E_1} \hat{\mathbf{v}}_1 \right)_{\hat{E}} + \left(\rho \mathbf{g}, \frac{1}{J_{E_2}} DF_{E_2} J_{E_2} \hat{\mathbf{v}}_1 \right)_{\hat{E}} \\
= & \frac{1}{8} \rho_{E_1} DF_{E_1}^T \mathbf{g} \cdot \hat{\mathbf{v}}_1 + \frac{1}{8} \rho_{E_2} DF_{E_2}^T \mathbf{g} \cdot \hat{\mathbf{v}}_1 \qquad (5.34)
\end{aligned}$$

Note that $\mathbf{v}_i$ is a unit vector in the physical space. But from equation 5.19, $\hat{\mathbf{v}}_i$ is not a unit vector and its length is $J_e = |e_i|$ which is the area of the face i. $\mathbf{M}_{E_i}^{jk}$ and $DF_{E_i}^T$ are evaluated at the vertex of interest in E_i. And in the derivation of equation 5.33, the trapezoidal rule is used for face integration. It is exact because $\hat{\mathbf{v}}_i \cdot \hat{\mathbf{n}}_{e_i}$ is bilinear on each cell face.

Further taking $\mathbf{v} = \mathbf{v}_2$, $\mathbf{v}_3$, $\cdots$, $\mathbf{v}_{12}$ in equation 5.22, twelve equations relating the twelve velocity degrees of freedom associated with the vertex of interest and the eight pressure degrees of freedom associated with the eight cells sharing the vertex of interest can be formed and written in matrix form

$$\mathbf{A} \mathbf{v}_{h,c}^D = \mathbf{B} \mathbf{p}_{h,c} + \mathbf{H}_c \qquad (5.35)$$

In equation 5.35, $\mathbf{A}$ is a 12×12 local mass matrix with $A_{ij} = (\mathbf{K}^{-1}\mathbf{v}_j, \mathbf{v}_i)_Q$, $\mathbf{v}_{h,c}^D = (v_{h1}^D,\ v_{h2}^D, \cdots,\ v_{h12}^D)^T$, $\mathbf{B}$ is a 12×8 pressure difference matrix with $B_{ik} = (w_k, \nabla \cdot \mathbf{v}_i)$, $\mathbf{p}_{h,c} = (p_{h1},\ p_{h2}, \cdots,\ p_{h8})^T$, and $\mathbf{H}_c$ is a 12×1 vector from the density term. If a Dirichlet pressure boundary condition is prescribed on any of the twelve cell faces intersecting at the vertex of interest, its contribution needs to be separated from $\mathbf{B}$ and $\mathbf{p}_{h,c}$ and accounted for in $\mathbf{H}_c$. Because the quadrature rule localizes the interactions among the velocity basis functions to those associated with the same vertex, $\mathbf{v}_{h,c}^D$ can be solved from equation 5.35

$$\mathbf{v}_{h,c}^D = \mathbf{A}^{-1}\mathbf{B}\mathbf{p}_{h,c} + \mathbf{A}^{-1}\mathbf{H} \tag{5.36}$$

Taking $w = w_1,\ w_2,\ \cdots,\ w_{npres}$ in the mass balance equation 5.23 and using the divergence theorem, we get

$$\begin{aligned}
(\nabla \cdot \mathbf{v}_h^D, w_i) &= (q, w_i) \\
\sum_{j=1}^{nvel} (\nabla \cdot \mathbf{v}_j, w_i)\mathbf{v}_{hj}^D &= (q, w_i) \\
\sum_{j=1}^{nvel} \langle \mathbf{v}_j \cdot \mathbf{n}_e, w_i \rangle_{\partial E_i} \mathbf{v}_{hj}^D &= (q, w_i)_{E_i} \\
\sum_{j=1}^{nvel} \langle \hat{\mathbf{v}}_j \cdot \hat{\mathbf{n}}_{\hat{e}}, \hat{w}_i \rangle_{\partial \hat{E}} \mathbf{v}_{hj}^D &= (\hat{q}, \hat{w}_i J_{E_i})_{\hat{E}} \qquad (5.37)
\end{aligned}$$

In equation 5.37, the face integration can be evaluated exactly by trapezoidal rule as in equation 5.33. Also note that for scalar quantities, $\hat{q} = q$ and $\hat{w}_i = w_i$. A global linear system for velocity degrees of freedom can be formed from the integration of equation 5.23

$$\tilde{\mathcal{B}}^T \mathbf{v}_{h,vector}^D = Q \tag{5.38}$$

where $\tilde{\mathcal{B}}^T_{ij} = (\nabla \cdot \mathbf{v}_j, w_i)$, $Q_i = (q, w_i)$, and

$$\mathbf{v}^D_{h,vector} = (\mathbf{v}^D_{h1},\ \mathbf{v}^D_{h2}, \cdots,\ \mathbf{v}^D_{h,nvec})^T \tag{5.39}$$

Substituting equation 5.36 for each vertex in $\mathcal{T}_h$ into 5.38 and moving the density terms and Dirichlet pressure boundary condition contributions to the RHS yields a global linear system for cell-centered pressure degrees of freedom

$$\tilde{\mathcal{B}}^T \mathcal{A}^{-1} \tilde{\mathcal{B}} \mathbf{p}_{h,vector} = Q - \tilde{\mathcal{B}}^T \mathcal{A}^{-1} \mathcal{H} \tag{5.40}$$

Here $\mathcal{A}$ is the global mass matrix with $\mathcal{A}^{-1}_{ij} = (\mathbf{K}^{-1}\mathbf{v}_j, \mathbf{v}_i)_Q$. It is a block diagonal matrix with each block $\mathbf{A}$ associated to a vertex in $\mathcal{T}_h$ (see equation 5.35). The inversion of $\mathcal{A}$ is done by inverting the local mass matrix $\mathbf{A}$ at each vertex. $\tilde{\mathcal{B}}$ is the global pressure difference matrix. For the vertex in Figure 5.2, $\mathbf{B}$ in equation 5.35 forms a consecutive 12-row in $\tilde{\mathcal{B}}$. In the implementation of the MFMFE method, $\mathbf{B}^T\mathbf{A}^{-1}\mathbf{B}$ is formed at each vertex and its surrounding elements and assembled to the global pressure matrix by resorting to the mapping from the local element number to the global element number. $\mathcal{H}$ denotes the global vector consisting of the contributions from density terms and any prescribed Dirichlet pressure boundary condition. It should be pointed out that in IPARS, a logical rectangular mesh is assumed. Therefore an element can have at most 26 neighboring elements. From the structure of $\mathbf{B}^T\mathbf{A}^{-1}\mathbf{B}$, it is clear that a pressure degree of freedom is related to another one if their elements share a vertex. As a result equation 5.40 leads to a 27-point stencil for cell-centered pressure degrees of freedom in logical rectangular mesh. Also note that with the choice of the enhanced BDDF_1 mixed finite element space and the special quadrature rule (5.24, 5.25, 5.28, and 5.29), $\tilde{\mathcal{B}}^T\mathcal{A}^{-1}\tilde{\mathcal{B}}$ is positive definite and no saddle-point type of velocity-pressure linear system needs to be solved [64, 142, 146].

5.3 Geomechanics Coupled with Two-phase MFMFE Flow Model

The derivation of the single phase and two-phase flow equations in the coupled poroelasticity model follows the same procedure described in Chapter 4. An isothermal assumption is made in this chapter, therefore the temperature contribution in reservoir porosity 4.28 vanishes. We present the equations for the two-phase flow [138] coupled with the linear elasticity model. Because the single phase slightly compressible flow can be viewed as a special case of the two-phase flow, the model equations and the solution strategy using MFMFE are analogous to what is presented in this section for the two-phase flow model.

Mass Conservation Equation:

$$\frac{\partial \rho_j S_j \phi^*}{\partial t} + \nabla \cdot \left(\rho_j \mathbf{v}_j^D\right) = q_j \tag{5.41}$$

Darcy's Law:

$$\mathbf{v}_j^D = -\frac{\mathbf{K} k_{rj}}{\mu_j}(\nabla p_j - \rho_j \mathbf{g}) \tag{5.42}$$

Constitutive Equations:

$$\phi^* = \phi_0 + \alpha\varepsilon_v + \frac{1}{N}(p - p_0) \tag{5.43}$$

$$\rho_j = \rho_j^0(1 + c_j(p_j - p_0)) \tag{5.44}$$

$$p_o = p_w + p_{cow}(S_w) \tag{5.45}$$

$$k_{rj} = k_{rj}(S_w) \tag{5.46}$$

$$S_w + S_o = 1 \tag{5.47}$$

Boundary and Initial Conditions:

$$p_w = p_D \quad \text{on } \Gamma_D \tag{5.48}$$

$$S_w = S_D \quad \text{on } \Gamma_D \tag{5.49}$$

$$\mathbf{v}_j^D \cdot \mathbf{n} = 0 \quad \text{on } \Gamma_N \tag{5.50}$$

$$p_w = p_w^0 \quad \text{at } t = 0 \tag{5.51}$$

$$S_w = S_w^0 \quad \text{at } t = 0 \tag{5.52}$$

In equations 5.41–5.52, subscript w denotes the water phase and o denotes the oil phase, capillary pressure p_{cow} is a function of water saturation S_w, ρ_j^0 is reference density of phase j at reference pressure p_0, and c_j is fluid compressibility of phase j. Note that water phase pressure p_w and saturation S_w are chosen as the primary unknowns for the two-phase flow model.

The linear elasticity model equations comprise the quasi-static force equilibrium equation 3.2, strain-displacement relation 3.3, total stress relation 3.14, boundary conditions 3.16, and initial conditions 3.15. It is discretized by the CG method on distorted hexahedra as described in Chapter 3 and the fluid pressure is applied as an external load. Note that under the isothermal assumption, the thermal stress $(3\lambda + 2G)\alpha^T(T - T_0)\delta_{ij}$ in 3.14 is ignored. The same fixed-stress iterative coupling scheme presented in Section 4.2.3 is utilized to solve the coupled two-phase flow and linear elasticity model. The procedure is similar to that outlined in Figure 4.1, with the compositional flow model replaced by the two-phase flow model.

In IPARS, the two-phase oil-water flow model is solved by an iterative implicit pressure explicit saturation (IMPES) scheme for the MFMFE method to be applicable [117, 138]. Dividing equation 5.41 by the reference density ρ_j^0 for each fluid phase j and summing up the resulting volume balance equation for both water and oil phases leads to

$$\frac{\partial \phi^* \left(\bar{\rho}_w S_w + \bar{\rho}_o(1 - S_w)\right)}{\partial t} + \nabla \cdot \left(\bar{\rho}_w \mathbf{v}_w^D + \bar{\rho}_o \mathbf{v}_o^D\right) = \bar{q}_w + \bar{q}_o \tag{5.53}$$

where $\bar{\rho}_j = \frac{\rho_j}{\rho_j^0}$ is the normalized density for phase j and $\bar{q}_j = \frac{q_j}{\rho_j^0}$ is the normalized source/sink term for phase j . Define $\mathbf{v}_t^D$, the total velocity, by

$$\mathbf{v}_t^D = \bar{\rho}_w \mathbf{v}_w^D + \bar{\rho}_o \mathbf{v}_o^D \tag{5.54}$$

Substituting Darcy's law 5.42 into equation 5.54 yields

$$\begin{aligned} \mathbf{v}_t^D &= -\bar{\rho}_w \frac{\mathbf{K} k_{rw}}{\mu_w}(\nabla p_w - \rho_w \mathbf{g}) - \bar{\rho}_o \frac{\mathbf{K} k_{ro}}{\mu_o}(\nabla p_w + \nabla p_{cow} - \rho_o \mathbf{g}) \\ &= -\mathbf{K}\left(\bar{\rho}_w \frac{k_{rw}}{\mu_w} + \bar{\rho}_o \frac{k_{ro}}{\mu_o}\right)(\nabla p_w - \rho_w \mathbf{g}) \\ &\quad -\mathbf{K}\bar{\rho}_o \frac{k_{ro}}{\mu_o}\left(\nabla p_{cow} - (\rho_o - \rho_w)\mathbf{g}\right) \end{aligned} \tag{5.55}$$

Define the normalized total mobility λ_t by

$$\lambda_t = \bar{\rho}_w \frac{k_{rw}}{\mu_w} + \bar{\rho}_o \frac{k_{ro}}{\mu_o} \tag{5.56}$$

Equation 5.55 is simplified as [137]

$$\mathbf{v}_t^D = -\mathbf{K}\lambda_t(\nabla p_w - \rho_w \mathbf{g}) - \mathbf{K}\lambda_o\left(\nabla p_{cow} - (\rho_o - \rho_w)\mathbf{g}\right) \tag{5.57}$$

The IMPES scheme solves equation 5.53 by treating p_w implicitly in 5.57 and other terms in 5.57 explicitly. That is

$$\begin{aligned} & \frac{(\phi^*\bar{\rho}_w)^{k+1}S_w^k + (\phi^*\bar{\rho}_o)^{k+1}(1-S_w^k) - (\phi^*\bar{\rho}_w S_w + \phi^*\bar{\rho}_o(1-S_w))^n}{\Delta t^{n+1}} \\ = \quad & \nabla\cdot\mathbf{K}\lambda_t^k\left((\nabla p_w^{k+1} - \rho_w^k\mathbf{g}) + \frac{\lambda_o^k}{\lambda_t^k}(\nabla p_{cow}^k - (\rho_o^k - \rho_w^k))\mathbf{g}\right) \\ & + \bar{q}_w^k + \bar{q}_o^k \end{aligned} \tag{5.58}$$

where $\lambda_o = \bar{\rho}_o \frac{k_{ro}}{\mu_o}$ is the normalized mobility for oil phase. Expanding the implicit terms in equation 5.58 to the first order terms in Taylor series, and recognizing equations 5.43 and 5.44, equation 5.58 becomes

$$\begin{aligned} & \frac{S_w^k\left(\bar{\rho}_w^k\left(\frac{1}{N} + \frac{\alpha^2}{K_{dr}}\right) + \phi^{*,k}c_w\right)\delta p^{k+1}}{\Delta t^{n+1}} \\ & + \frac{(1-S_w)^k\left(\bar{\rho}_o^k\left(\frac{1}{N} + \frac{\alpha^2}{K_{dr}}\right) + \phi^{*,k}c_o\right)\delta p^{k+1}}{\Delta t^{n+1}} + \nabla\cdot\delta\mathbf{v}_t^{D,k+1} \\ = \quad & \frac{(\phi^*\bar{\rho}_w S_w)^n + (\phi^*\bar{\rho}_o(1-S_w))^n}{\Delta t^{n+1}} - \frac{(\phi^*\bar{\rho}_w S_w)^k + (\phi^*\bar{\rho}_o(1-S_w))^k}{\Delta t^{n+1}} \\ & + \bar{q}_w^k + \bar{q}_o^k - \nabla\cdot\mathbf{v}_t^{D,k} \end{aligned} \tag{5.59}$$

where

$$\delta\mathbf{v}_t^{D,k+1} = -\mathbf{K}\lambda_t^k\nabla\delta p^{k+1} \tag{5.60}$$

and

$$\mathbf{v}_t^{D,k} = -\mathbf{K}\lambda_t^k(\nabla p_w^k - \rho_w^k\mathbf{g}) - \mathbf{K}\lambda_o^k\left(\nabla p_{cow}^k - (\rho_o^k - \rho_w^k)\mathbf{g}\right) \tag{5.61}$$

Equations 5.60 and 5.61 are different from the single phase incompressible Darcy velocity equation 5.2 due to the mobility terms and that 5.61 contains contributions from two fluid phases. In the following we will show how the total velocity $\mathbf{v}_t^D$ and the normalized mobility terms λ_t and λ_o in equation 5.61 are treated under the MFMFE framework [117, 138]. The treatment of the normalized total mobility term in equation 5.60 is similar so it is omitted here.

Let $\mathbf{v}_t^{D,k} = \mathbf{v}_{tw}^{D,k} + \mathbf{v}_{to}^{D,k}$, where

$$\begin{aligned} \mathbf{v}_{tw}^{D,k} &= -\mathbf{K}\lambda_t^k(\nabla p_w^k - \rho_w^k\mathbf{g}) && (5.62) \\ \mathbf{v}_{to}^{D,k} &= -\mathbf{K}\lambda_o^k\left(\nabla p_{cow}^k - (\rho_o^k - \rho_w^k)\mathbf{g}\right) && (5.63) \end{aligned}$$

Multiplying equation 5.62 by $\frac{\mathbf{K}^{-1}}{\lambda_t^k}$ yields

$$\mathbf{K}^{-1}\frac{\mathbf{v}_{tw}^{D,k}}{\lambda_t^k} = -(\nabla p_w^k - \rho_w^k\mathbf{g}) \tag{5.64}$$

Similar to equation 5.30, the velocity function $\mathbf{v}_{tw}^{D,k}$ divided by λ_t^k can be expressed as

$$\frac{\mathbf{v}_{tw}^{D,k}}{\lambda_t^k} = \sum_{i=1}^{nvel}\frac{v_{tw,hi}^{D,k}}{\lambda_{t,hi}^k}\mathbf{v}_i \tag{5.65}$$

where $v_{tw,hi}^{D,k}$ is the degree of freedom for partial velocity $\mathbf{v}_{tw}^{D,k}$ and $\lambda_{t,hi}^k$ is the normalized total mobility defined at the same location as the velocity basis function $\mathbf{v}_i$. Assuming c is an arbitrary internal vertex in the finite element partition $\mathcal{T}_h$ (see Figures 5.2–5.5), testing equation 5.64 with $\mathbf{v}_1,\ \mathbf{v}_2,\ \cdots,\ \mathbf{v}_{12}$ and using the quadrature rule defined in Section 5.2, we obtain

$$\mathbf{A}\Lambda_t^{-1,k}\mathbf{v}_{tw,hc}^{D,k} = \mathbf{B}\mathbf{p}_{w,hc}^k + \mathbf{H}_{w,c}^k \tag{5.66}$$

In equation 5.66, $\mathbf{v}_{tw,hc}^{D,k} = (v_{tw,h1}^{D,k},\ v_{tw,h2}^{D,k}, \cdots,\ v_{tw,h12}^{D,k})^T$, $\mathbf{p}_{w,hc}^k = (p_{w,h1}^k,\ p_{w,h2}^k, \cdots,\ p_{w,h8}^k)^T$, $\mathbf{H}_{w,c}^k$ is a 12×1 vector consisting of contributions from density and Dirichlet pressure boundary conditions for the water phase, and $\Lambda_t^{-1,k} = (\Lambda_t^k)^{-1}$ is a 12×12 diagonal matrix defined by

$$\Lambda_t^k = diag(\lambda_{t,h1}^k,\ \lambda_{t,h2}^k,\ \cdots,\ \lambda_{t,h12}^k). \tag{5.67}$$

$\lambda_{t,hi}^k$ is the upwinded or averaged normalized total mobility on i^{th} cell interface intersected at vertex c. For example, if the upwinded mobility is used,

$$\lambda_{t,h1}^k = \begin{cases} \lambda_{t,E_1}^k & \text{if} \quad v_{tw,h1}^{D,k} \geq 0 \\ \lambda_{t,E_2}^k & \text{if} \quad v_{tw,h1}^{D,k} < 0 \end{cases}; \tag{5.68}$$

if the averaged mobility is used,

$$\lambda_{t,h1}^k = \frac{1}{2}(\lambda_{t,E_1}^k + \lambda_{t,E_2}^k). \tag{5.69}$$

In equations 5.68 and 5.69, λ_{t,E_1}^k and λ_{t,E_2}^k are the normalized total mobilities defined in cells E_1 and E_2, respectively.

From equation 5.66, $\mathbf{v}_{tw,hc}^{D,k}$ can be solved

$$\mathbf{v}_{tw,hc}^{D,k} = \Lambda_t^k\mathbf{A}^{-1}\mathbf{B}\mathbf{p}_{w,hc}^k + \Lambda_t^k\mathbf{A}^{-1}\mathbf{H}_{w,c}^k \tag{5.70}$$

Similarly, the partial velocity degrees of freedom vector $\mathbf{v}_{to,hc}^{D,k}$ associated with vertex c can be expressed as

$$\mathbf{v}_{to,hc}^{D,k} = \Lambda_o^k\mathbf{A}^{-1}\mathbf{B}\mathbf{p}_{cow,hc}^k + \Lambda_o^k\mathbf{A}^{-1}\mathbf{H}_{ow,c}^k \tag{5.71}$$

where

$$\Lambda_o^k = diag(\lambda_{o,h1}^k,\ \lambda_{o,h2}^k,\ \cdots,\ \lambda_{o,h12}^k) \tag{5.72}$$

is the 12 × 12 diagonal oil mobility matrix associated with vertex c whose diagonal element $\lambda_{o,hi}^k$ is the upwinded or averaged normalized oil mobility on i^{th} cell interface intersected at vertex c. $\mathbf{H}_{ow,c}^k$ consists of contributions from density term $(\rho_o^k - \rho_w^k)\mathbf{g}$ and Dirichlet boundary conditions for capillary pressure p_{cow}^k.

Therefore, applying the MFMFE method on equations 5.59, 5.57, and 5.60 leads to a global linear system for $\delta\mathbf{p}_{w,h,vector}^{k+1}$

$$\begin{aligned}(\mathcal{C}^k + \Delta t^{n+1}\tilde{\mathcal{B}}^T\mathbf{\Lambda}_t^k\mathcal{A}^{-1}\tilde{\mathcal{B}})\delta\mathbf{p}_{w,h,vector}^{k+1} &= -\Delta t^{n+1}\tilde{\mathcal{B}}^T\mathbf{\Lambda}_t^k\mathcal{A}^{-1}\tilde{\mathcal{B}}\mathbf{p}_{w,h,vector}^k \\ -\Delta t^{n+1}\tilde{\mathcal{B}}^T\mathbf{\Lambda}_o^k\mathcal{A}^{-1}\tilde{\mathcal{B}}\mathbf{p}_{cow,h,vector}^k + \Delta t^{n+1}\tilde{Q}^k\end{aligned} \tag{5.73}$$

In equation 5.73, $\mathcal{C}^k$ is the matrix related to the first two terms in the LHS of equation 5.59. $\mathbf{\Lambda}_t^k$ and $\mathbf{\Lambda}_o^k$ are the global normalized total mobility and oil mobility matrices whose diagonal block associated with vertex c are Λ_t^k and Λ_o^k, respectively. $\tilde{Q}^k$ contains contributions from density terms, Dirichlet pressure boundary conditions, source/sink terms, and volume accumulation terms from previous (k^{th}) Newton iteration.

After $p_{w,h}^{k+1}$ is solved, water phase saturation is updated explicitly from the mass balance equation 5.41 for $j = w$

$$\frac{\rho_w^{k+1}S_w^{k+1}\phi^{*,k+1} - \rho_w^n S_w^n \phi^{*,n}}{\Delta t^{n+1}} = -\nabla \cdot \rho_w^{k+1}\mathbf{v}_w^{D,k+1} + q_w^{k+1} \tag{5.74}$$

Note that in the RHS of equation 5.74, terms related to S_w still uses S_w^k. Several explicit saturation update steps can be nested within one pressure step [137]. Iterations between pressure solve and saturation update continues until volume conservation equation 5.53 is satisfied for $p_{w,h}^{k+1}$ and S_w^{k+1}.

We should also point out that the inverse of the local mass matrix $\mathbf{A}$ defined in equation 5.35 is needed in calculating both the pressure matrix and the RHS of equation 5.73, updating saturation in 5.74, and checking the volume balance equation 5.53. Instead of building $\mathbf{A}^{-1}$ every time when it is needed, we store it for all vertices in $\mathcal{T}_h$ in the compressed storage format (CSR) to improve the efficiency of the MFMFE flow simulator.

5.4 Numerical Examples

5.4.1 Quarter Wellbore Model

The first numerical example in this section is a quarter wellbore model to demonstrate that the coupled MFMFE flow and CG linear elasticity model can handle complex geometry and realistic boundary conditions. The model domain is a 250 ft × 250 ft × 250 ft cube with a quarter of a cylindrical wellbore centered along an edge of the cube. The mesh contains 400000 non-uniform hexahedra, with 160 elements in the radial direction, 50 elements in the hoop direction, and 50 elements in the vertical direction. Fine grids are used near the wellbore and they coarsen as their distances from the wellbore increase. Figure 5.6 shows the model geometry in 2D with boundary conditions whereas Figure 5.7 illustrates the model geometry in 3D space. The single phase flow model is used in this example. For the flow problem, a constant pressure of 800 psi is enforced on the wellbore surface while a transient pressure boundary condition, $p(t) = 2000 - 500 \cdot t$, is prescribed on the two boundary faces far away from the wellbore. The other four faces are no-flow boundaries. For the geomechanics problem, zero normal displacement and zero shear traction boundary conditions are applied on faces y=0, z=0, and x=0. A compressive normal stress of 2400 psi is assigned for faces y=250 ft and z=250 ft. On the face x=250 ft, a compressive normal stress of 3000 psi is prescribed. The pressure boundary condition on the wellbore for the flow problem is also supplied as a compressive traction boundary condition for the geomechanics problem. Note that the traction is in the direction normal to the wellbore surface. Therefore its direction varies along the hoop direction. The magnitude of the traction is 800 psi. Gravity is ignored in the simulation. Input parameters for the numerical model in IPARS are summarized in Table 5.1.

The simulation was run using 64 processes. Figures 5.8–5.15 are profiles of pressure, x-displacement, y-displacement, and z-displacement at 0.1 days and 2.0 days, respectively. From 0.1 days to 2.0 days, as the pressure in the domain drops and its gradient decreases, the top surface (x=250 ft) subsides and the top side of the wellbore experiences the largest vertical subsidence in the domain. The evolution of horizontal displacements, i.e. y-displacement and z-displacement, demonstrate that the domain is also compacted horizontally as a result of the fluid production. The symmetry of the y-displacement and the z-displacement is expected because the geometry and boundary conditions are symmetric. Note that the unit of displacements for the linear

SYMBOL	QUANTITY	VALUE
t^T	total simulation time	2.0 days
Δt	time step size	0.1 days
X_L	dimension in x	250 ft
Y_L	dimension in y	250 ft
Z_L	dimension in z	250 ft
r_w	wellbore radius	5 ft
N_x	number of grids in x direction	50
N_θ	number of grids in hoop direction	50
N_r	number of grids in radial direction	160
k_{xx}	vertical permeability	5 md
k_{yy}, k_{zz}	horizontal permeability	20 md
ϕ_0	initial porosity	0.2
μ_w	water viscosity	1.0 cp
c_f	water compressibility	4.0×10^{-5} $1/psi$
p_0	initial pressure	2000 psi
p_w	constant wellbore pressure	800 psi
p_t	transient pressure B.C. on y=250 ft and z=250 ft	2000-500·t psi
E	Young's modulus	2.3×10^6 psi
ν	Poisson's ratio	0.18125
α	Biot's constant	0.98
σ_{ob}	overburden normal stress on x=250 ft	-3000 psi
σ_h	horizontal normal stress on y=250 ft and z=250 ft	-2400 psi
DoF_{flow}	Number of pressure unknowns	400000
DoF_{mech}	Number of displacement unknowns	1256283

Table 5.1: Parameters for quarter wellbore model

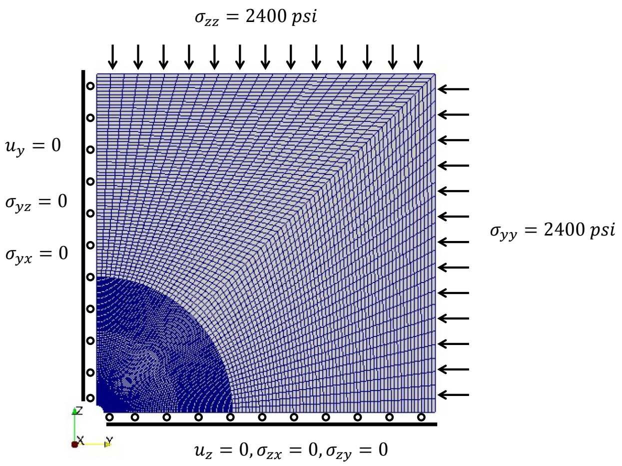

Figure 5.6: Quarter wellbore model geometry in 2D and boundary conditions

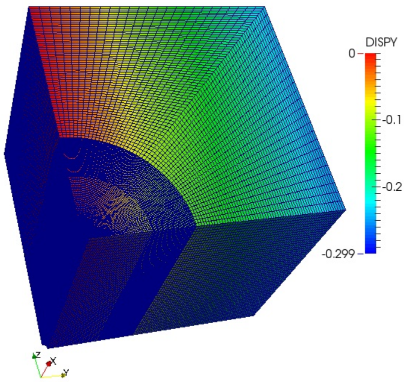

Figure 5.7: Quarter wellbore model geometry in 3D

elasticity model on hexahedra grids is foot, different from inch used for the geomechanics model on rectangular grids in Chapter 4.

5.4.2 Coupled Hexahedral Mesh

The second numerical example is a quarter of a 5-spot injection-production problem on a coupled mesh. The mesh is a 3D extension of the 2D mesh presented in [142]. It consists of four zones which can be seen in Figures 5.16 and 5.17. The lower right quadrant contains a smooth h^2-perturbed hexahedral mesh whereas the lower left and upper right zones comprise h-perturbed hexahedral elements. The upper left quadrant has rectangular elements. The non-symmetric quadrature rule 5.27 is employed in h-perturbed (distorted) hexahedra for accurate approximation and the symmetric quadrature rule 5.26 is used

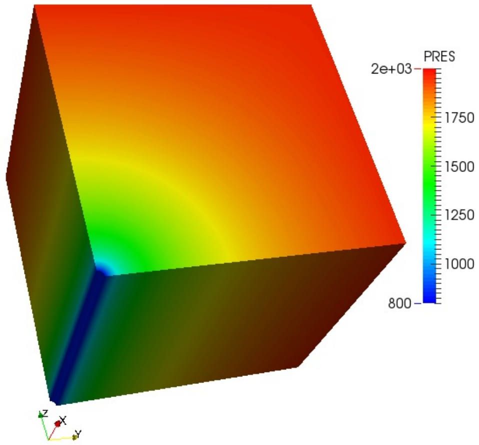

Figure 5.8: Quarter wellbore model: pressure at 0.1 days

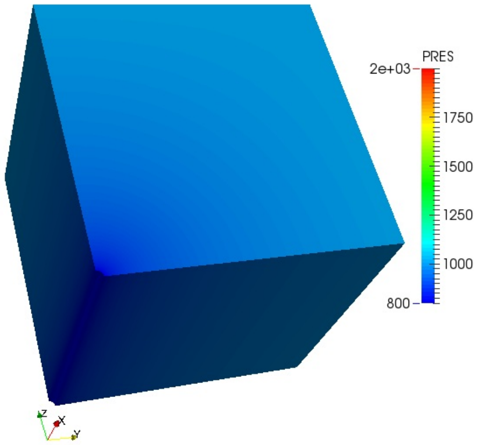

Figure 5.9: Quarter wellbore model: pressure at 2.0 days

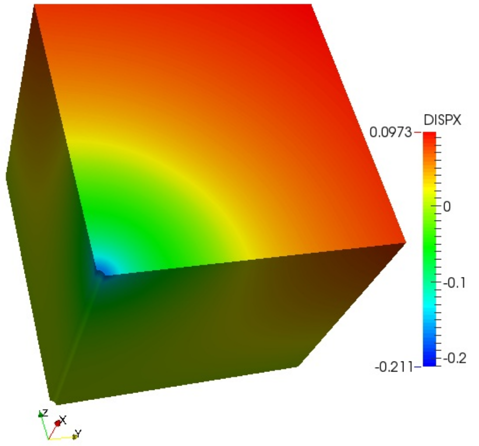

Figure 5.10: Quarter wellbore model: x-displacement at 0.1 days

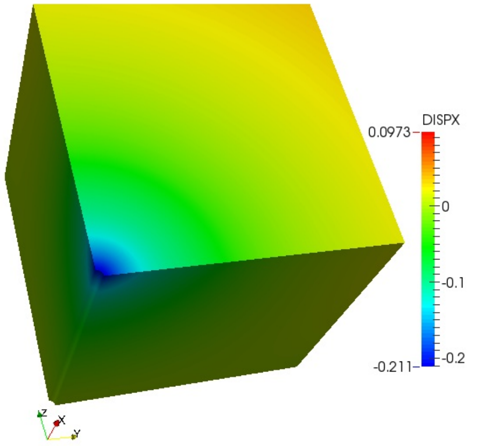

Figure 5.11: Quarter wellbore model: x-displacement at 2.0 days

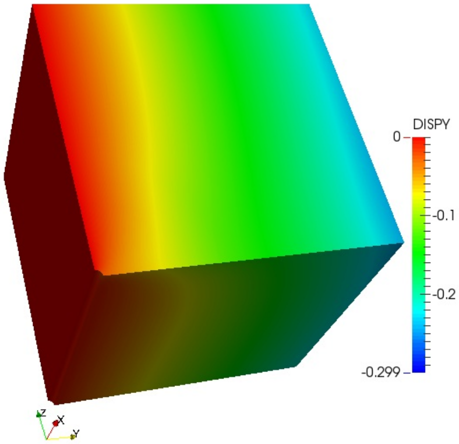

Figure 5.12: Quarter wellbore model: y-displacement at 0.1 days

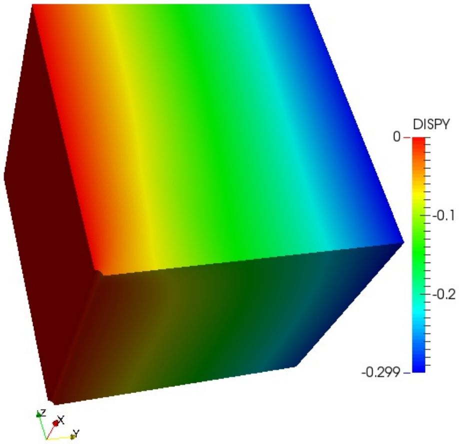

Figure 5.13: Quarter wellbore model: y-displacement at 2.0 days

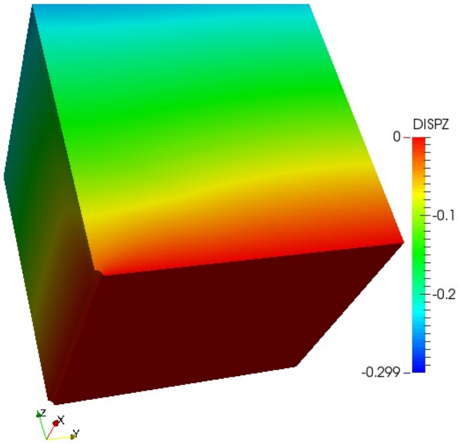

Figure 5.14: Quarter wellbore model: z-displacement at 0.1 days

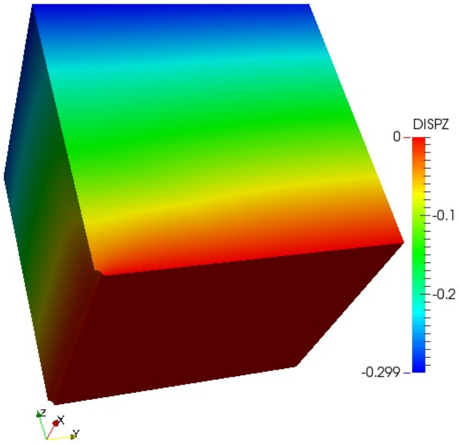

Figure 5.15: Quarter wellbore model: z-displacement at 2.0 days

in the remaining elements. The model domain is 20 ft × 1500 ft × 1500 ft with 10 × 150 × 150 elements. Two-phase flow is assumed in this example. Gravity and capillary pressure are ignored. The initial reservoir pressure is 400 psi with uniform water saturation equal to 0.316. A BHP specified water injection well is drilled at y=5 ft and z=5 ft while a BHP specified production well is located at y=1495 ft and z=1495 ft. No-flow boundary conditions are assumed for all surfaces. Zero normal displacement and zero shear traction boundary conditions are enforced on x=20 ft, y=0 ft, and z=0 ft. Zero traction boundary conditions are prescribed on x=0 ft, y=1500 ft, and z=1500 ft. Table 5.2 lists model parameters for IPARS simulation together with numbers of degrees of freedom for both flow and geomechanics models. The simulation was run with 128 processes.

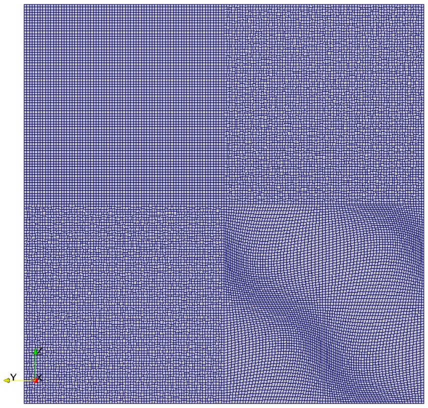

Figure 5.16: Coupled hexahedral mesh

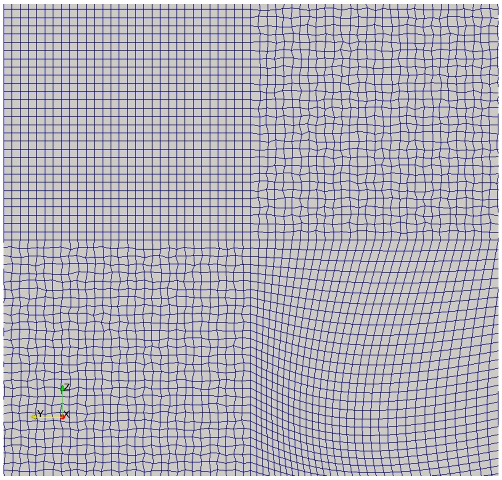

Figure 5.17: Coupled hexahedral mesh: zoomed-in

Figures 5.18 and 5.19 are water saturation profile at 80.1 days, one

SYMBOL	QUANTITY	VALUE
t^T	total simulation time	80.1 days
X_L	dimension in x	20 ft
Y_L	dimension in y	1500 ft
Z_L	dimension in z	1500 ft
N_x	number of grids in x	10
N_y	number of grids in y	150
N_z	number of grids in z	150
k	permeability in x,y,and z	500 md
ϕ_0	initial porosity	0.2
μ_w	water viscosity	1.0 cp
μ_o	oil viscosity	2.0 cp
c_f	water compressibility	1.0×10^{-6} $1/psi$
c_o	oil compressibility	1.0×10^{-4} $1/psi$
p_0	initial pressure	400 psi
S_w^0	initial water saturation	0.316
BHP_{inj}	water injector BHP	1000 psi
BHP_{prod}	producer BHP	100 psi
E	Young's modulus	1.0×10^6 psi
ν	Poisson's ratio	0.3
α	Biot's constant	1.0
DoF_{flow}	Number of pressure unknowns	225000
DoF_{mech}	Number of displacement unknowns	752433

Table 5.2: Parameters for coupled mesh case

with mesh visualized and one without. The evolution of pressure field (see Figures 5.20 and 5.21) indicates the average pressure of the reservoir increases as a result of the injection-production activity. Figures 5.22–5.27 show the geomechanical response of the reservoir matrix to the pressure increase. The solid skeleton expands in all three directions at the end of the simulation.

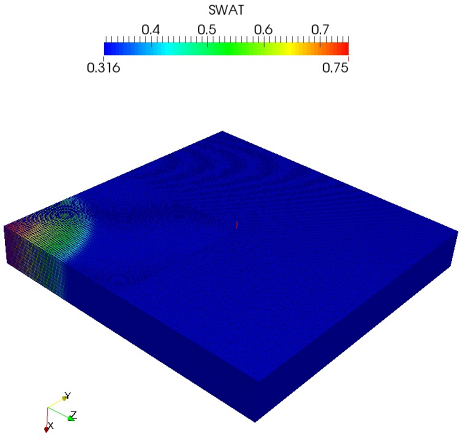

Figure 5.18: Coupled mesh case: water saturation at 80.1 days with mesh

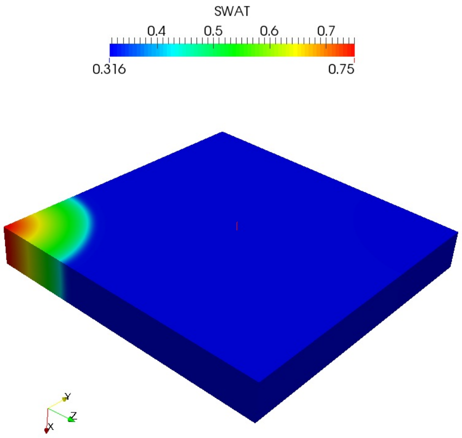

Figure 5.19: Coupled mesh case: water saturation at 80.1 days

To illustrate that the MFMFE method with non-symmetric quadrature rule produces accurate approximation on distorted hexahedra, we compare the solution on the coupled mesh to the solution on a uniform rectangular mesh. The rectangular mesh also has $10 \times 150 \times 150$ elements. Each element is of size 2 ft $\times 10$ ft $\times 10$ ft. All other model parameters are the same. We compare the injection well rate in Figure 5.28 and production well water/oil ratio in Figure 5.29. Comparison of y-displacement at 80.1 days between the simulation on

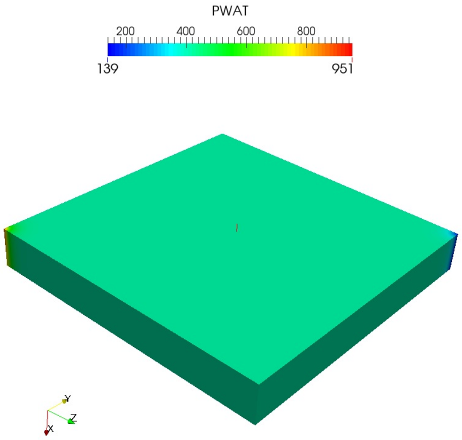

Figure 5.20: Coupled mesh case: water pressure at 0.1 days

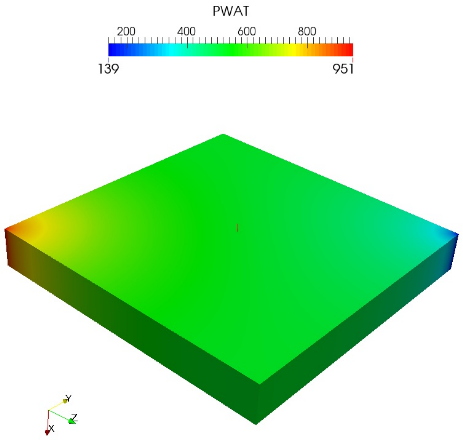

Figure 5.21: Coupled mesh case: water pressure at 80.1 days

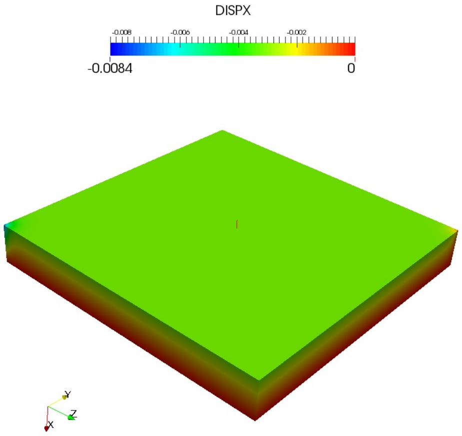

Figure 5.22: Coupled mesh case: x-displacement at 0.1 days

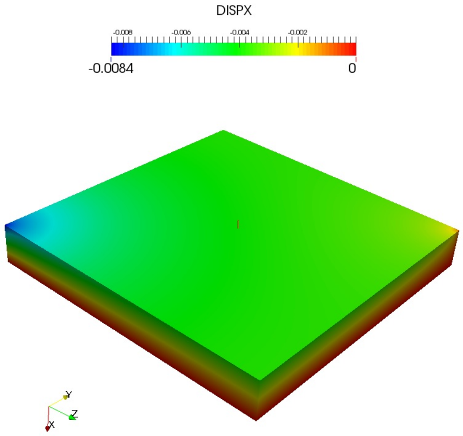

Figure 5.23: Coupled mesh case: x-displacement at 80.1 days

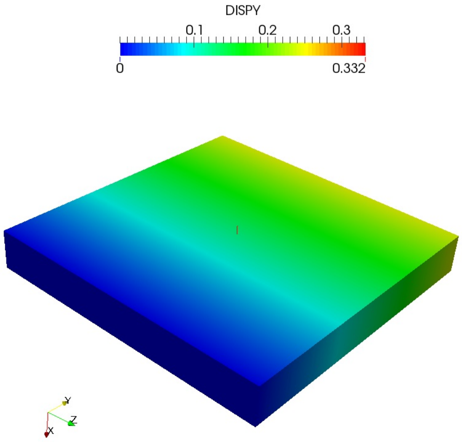

Figure 5.24: Coupled mesh case: y-displacement at 0.1 days

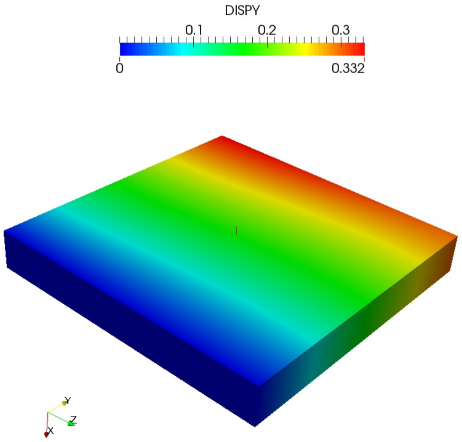

Figure 5.25: Coupled mesh case: y-displacement at 80.1 days

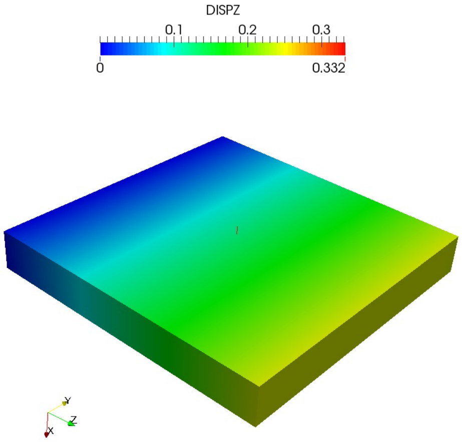

Figure 5.26: Coupled mesh case: z-displacement at 0.1 days

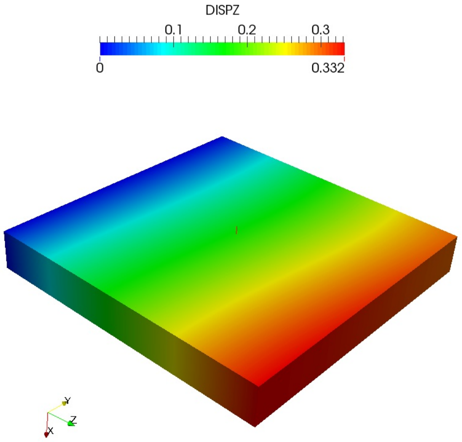

Figure 5.27: Coupled mesh case: z-displacement at 80.1 days

coupled mesh and the simulation on rectangular mesh is given in Figures 5.30 and 5.31. These comparisons demonstrate satisfactory match between the two simulation results.

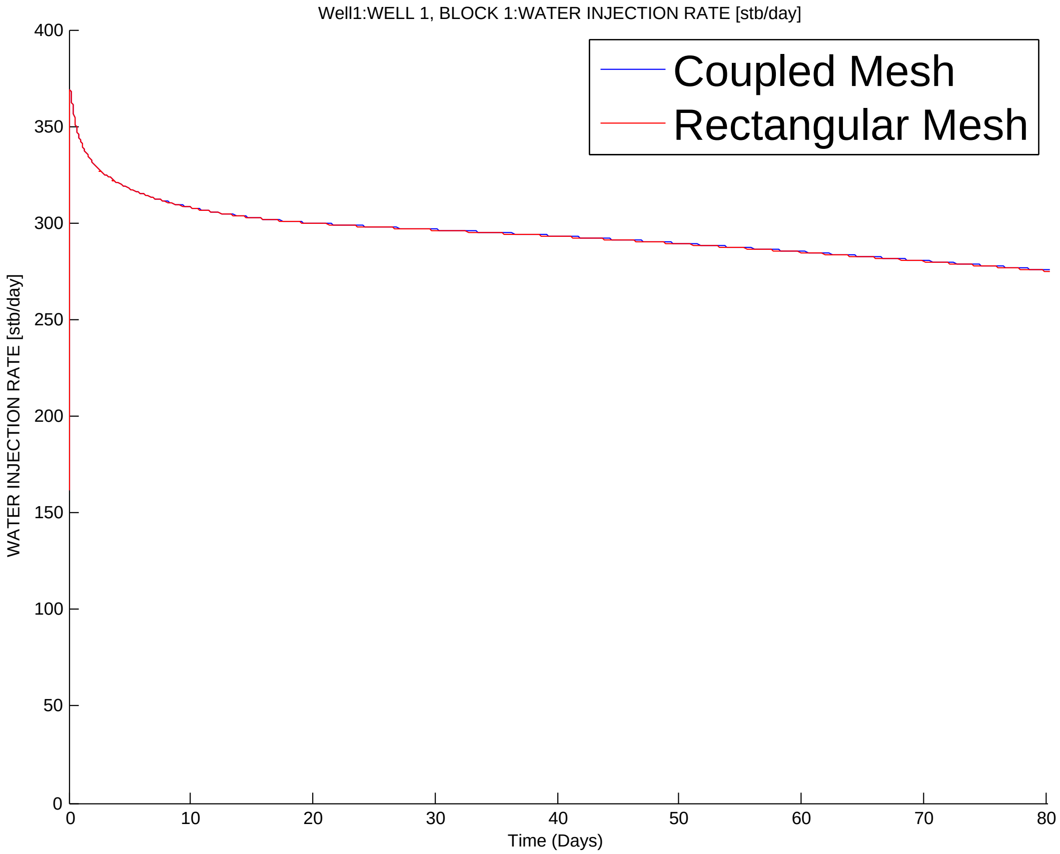

Figure 5.28: Injection well rate comparison between coupled mesh and rectangular mesh

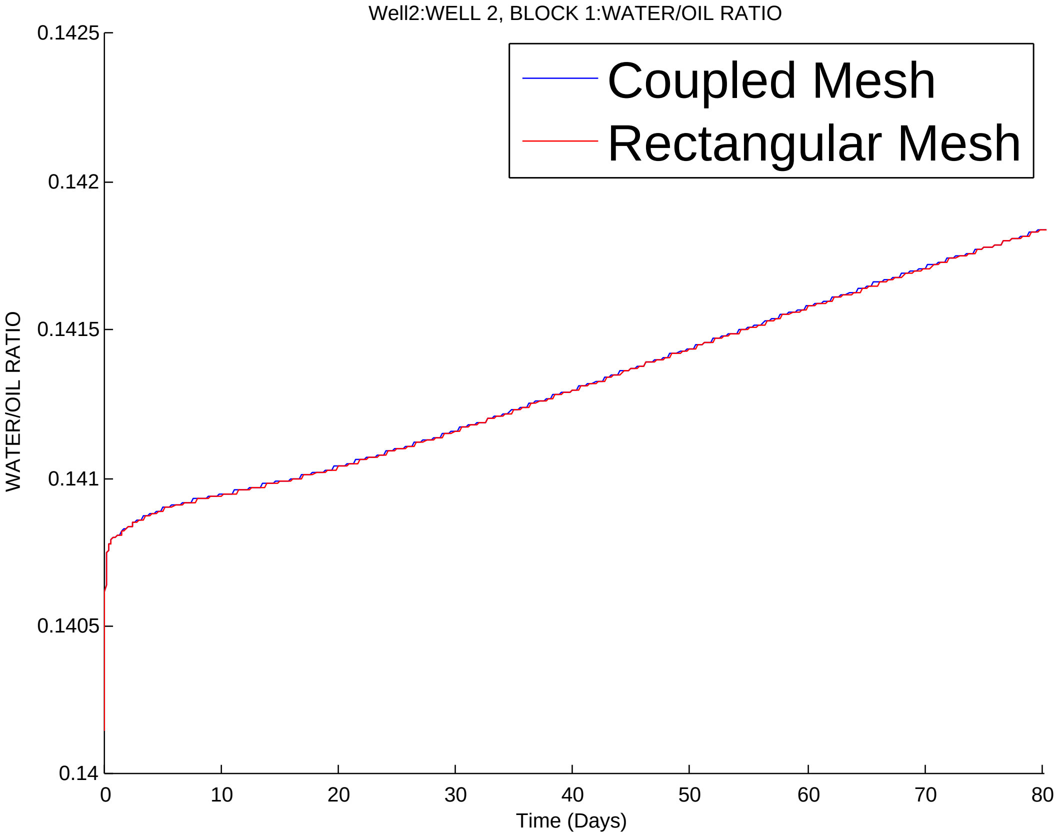

Figure 5.29: Production well water/oil ratio comparison between coupled mesh and rectangular mesh

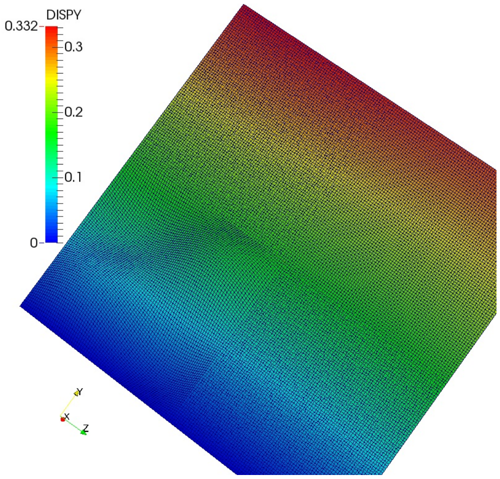

Figure 5.30: Y-displacement at 80.1 days on coupled mesh

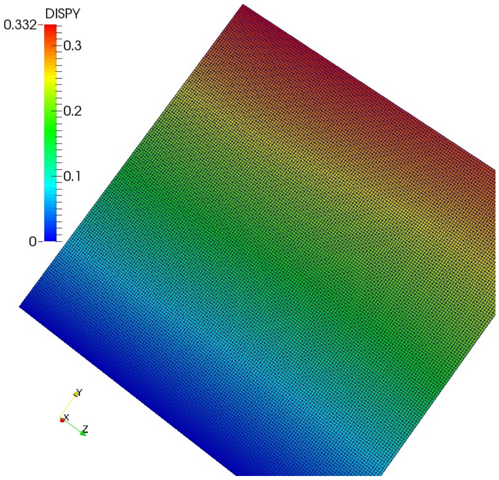

Figure 5.31: Y-displacement at 80.1 days on rectangular mesh

Chapter 6

Parallel Simulation

6.1 Introduction

Simulations of coupled poromechanical or thermoporomechanical processes in field scale with high resolution usually impose significant demands on both computer memory and computation time. For example, a reservoir model can consist of millions of grid cells and nodes. In the compositional flow model, each cell requires memory for multi component and phase related data; in the MFMFE flow model, each grid node (vertex) needs to store the inverse of a local mass matrix which is up to 12×12 in size; in the linear elasticity model, each node necessitates the storage of a displacement vector, a stress tensor, and a strain tensor. The 27-pt stencil in MFMFE and CG formulations also requires a large amount of memory for the linear system storage. The challenge in computation time is a result of two factors: 1. the high cost to solve the large linear systems for pressure, temperature, and displacement, respectively; 2. the long time span of the physical processes which can be several years for an EOR process or hundred of years for a CO_2 leakage prediction. Distributed memory parallel computing provides a means to deal with these memory and computation time challenges.

In this work we focus on parallelization of the coupled poroelasticity simulator developed in Chapters 3, 4, and 5. The geomechanics, MFE compositional flow [45], MFMFE single and two-phase flow [138, 142], and energy balance models [126] are developed as individual modules within the IPARS framework [136]. The IPARS framework handles structured (logically rectangular) grids and was originally designed for element-based data communication such as pressure data in flow models. In this work, we enhance the capability of the IPARS framework for node-based data communication to parallelize the geomechanics model. We also parallelize the two-phase MFMFE flow model developed in [138]. Because the linear system of the geomechanics model is more costly to solve than those of the flow and thermodynamics models, we are only concerned with parallel performance of linear solvers for the geomechanics model within the scope of this work. For our purpose of efficiently simulating field scale problems for long time span, strong scalability of the linear solver is important. We use the generalized minimal residual (GMRES) solver with the BoomerAMG preconditioner from the hypre library [77] and the geometric multigrid (GMG) solver from the UG4 software toolbox [61] to solve the geomechanics linear system. To improve mesh partitioning quality and solver performance, we integrate the multilevel k-way mesh partitioner from METIS [67] into IPARS.

6.2 Numerical Examples

All parallel simulations presented in this dissertation are performed on the supercomputer Stampede in Texas Advanced Computing Center at The University of Texas at Austin. Stampede has 6400 computing nodes, most of which are configured with two 8-core Intel Xeon E5-2680 processors running at 2.7 GHz (3.5 GHz with turbo) and one 61-core Intel Xeon Phi SE10P coprocessor running at 1.1 GHz. Each node has 32 GB host memory for the two E5-2680 processors and an additional 8 GB memory for the coprocessor. Computing nodes are connected by a 56 Gb/s FDR InfiniBand network [29]. Our simulations only utilize the 8-core E5-2680 processors but not the coprocessors.

6.2.1 Cranfield Case

As the first numerical example, we rerun the Cranfield CO_2 sequestration simulation using different numbers of processors to verify the parallelization of the coupled compositional flow and linear elasticity model in IPARS. The model description can be found in Section 4.3.1.2 and the input parameters are listed in Table 4.4. Type I stress-dependent permeability in equation 4.59 is employed with $b = 1.0 \times 10^{-3}\ 1/psi$. Figures 6.1 and 6.2 show excellent matches of reservoir average pressure history and BHP history for the injector CFU 31-F1 among simulations with 8, 16, 32, 64, and 128 processors. For this example, we use the GMRES solver from the hypre library [77] with BoomerAMG as the preconditioner to solve the elasticity linear system. The

Number of Processes	Solver Time (s)	Speedup Efficiency
8	15722.875	1
16	8233.990234	0.95475429
32	4680.088867	0.839881221
64	2790.81543	0.704224061
128	1246.232422	0.7885204

Table 6.1: Speedup efficiency for Cranfield case

linear solver relative tolerance is set to 1.0×10^{-8}. Figure 6.3 is the scalability test result for the elasticity linear solver and Table 6.1 lists the numbers for the speedup efficiency. About 79 % of ideal speedup is observed from 8 processes to 128 processes. We would like to point out that the linear solver (biconjugate gradient stabilized solver with multigrid preconditioner) time for the compositional flow model for the 8 processes run is 862.853 s, or 5.5% of the elasticity linear solver time.

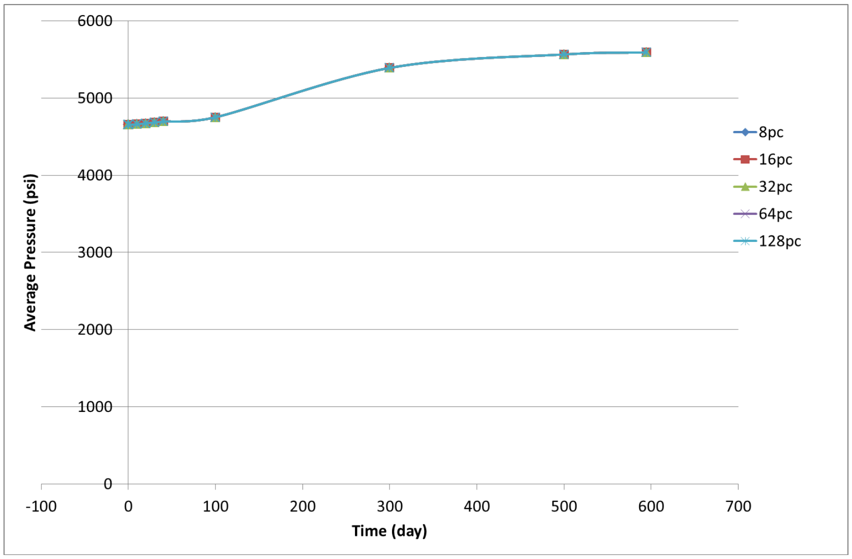

Figure 6.1: Average pressure history comparison for Cranfield case

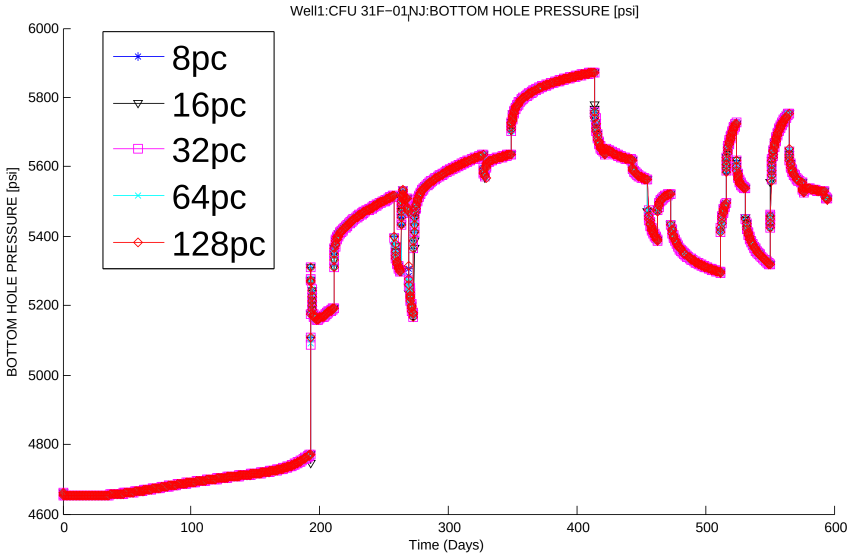

Figure 6.2: Injector CFU 31-F1 BHP history comparison for Cranfield case

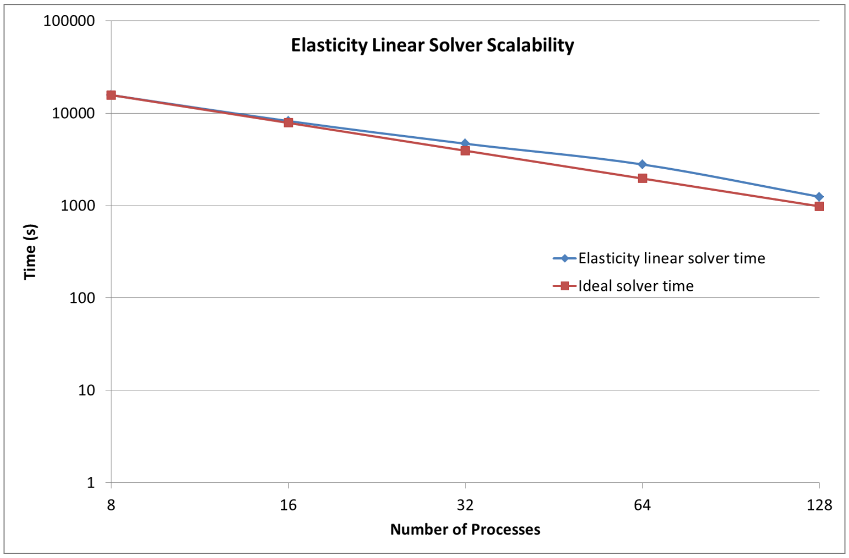

Figure 6.3: Scalability test for Cranfield case

6.2.2 Coupled Mesh Case

In the second numerical example we verify the parallelization of the coupled two-phase MFMFE flow and linear elasticity model on general hexahedral grids. We rerun the case with coupled hexahedral mesh in Section 5.4.2. Most of the model parameters are the same as in Table 5.2, but this time we refine the mesh to $10 \times 300 \times 300$ and shorten the total simulation time to 10.1 days. As a result, the number of pressure degrees of freedom for the MFMFE flow model increases to 900000 and the number of displacement degrees of freedom for the CG elasticity model increases to 2989833. We use the GMRES solver with the BoomerAMG preconditioner from the hypre library [77] and a relative tolerance of 1.0×10^{-8} for the elasticity linear system. Six simulations were run using 8, 16, 32, 64, 128, and 256 processes. In Figures 6.4–6.6, we compare the water rate for the injection well and the oil and water rates for the production well from the six simulations. The matched results demonstrate that the coupled two-phase MFMFE flow and CG linear elasticity simulator runs correctly on the parallel computer. Figure 6.7 shows the scalability of the elasticity linear solver on different numbers of processes and the numbers of speedup efficiency are summarized in Table 6.2. The elasticity linear solver attains about 69 % of ideal speedup from 8 processes to 256 processes on the coupled anisotropic mesh with distorted hexahedral elements.

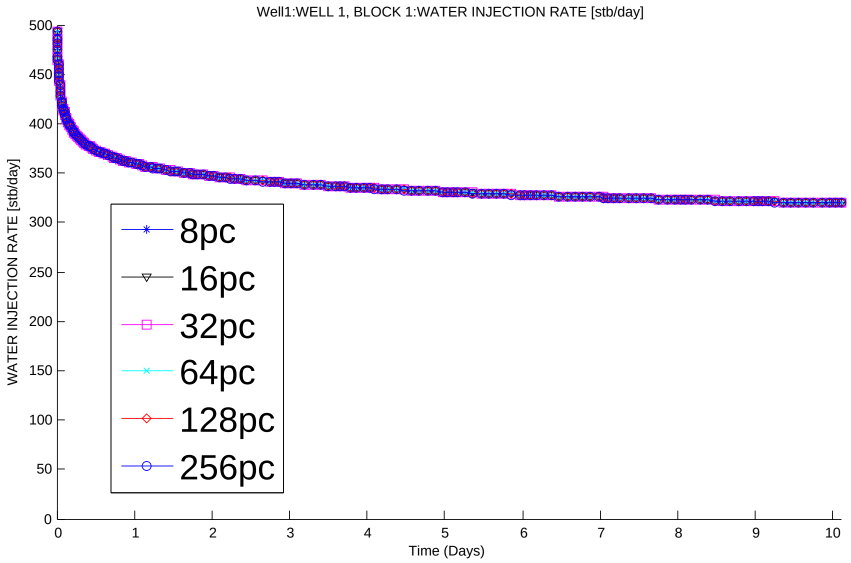

Figure 6.4: Water injection rate for coupled mesh case

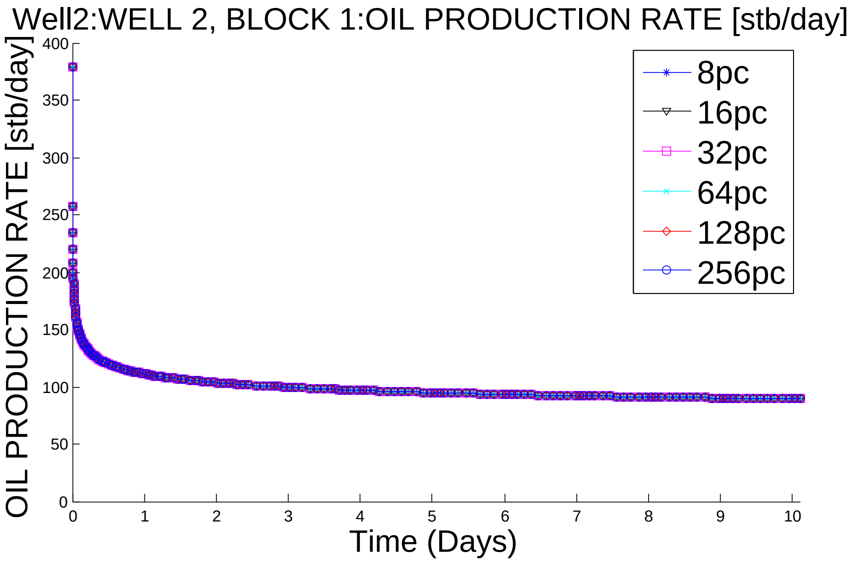

Figure 6.5: Oil production rate for coupled mesh case

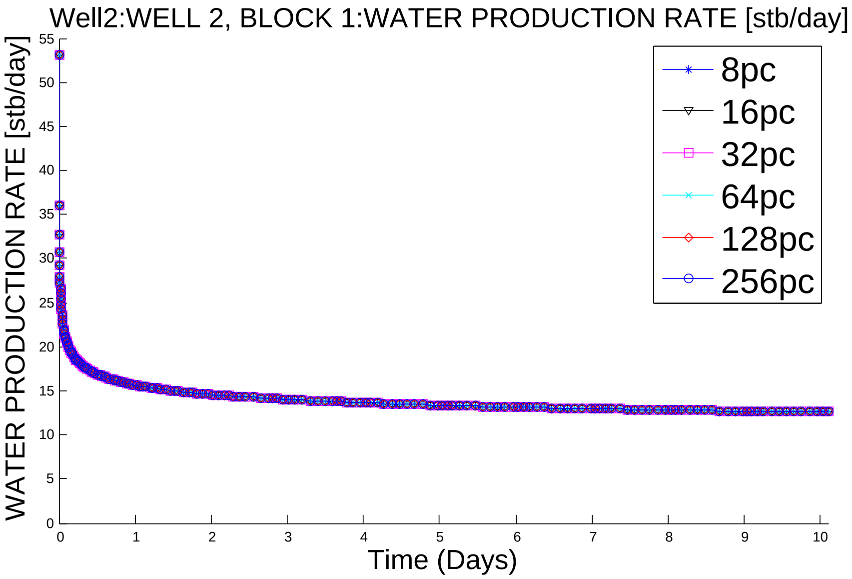

Figure 6.6: Water production rate for coupled mesh case

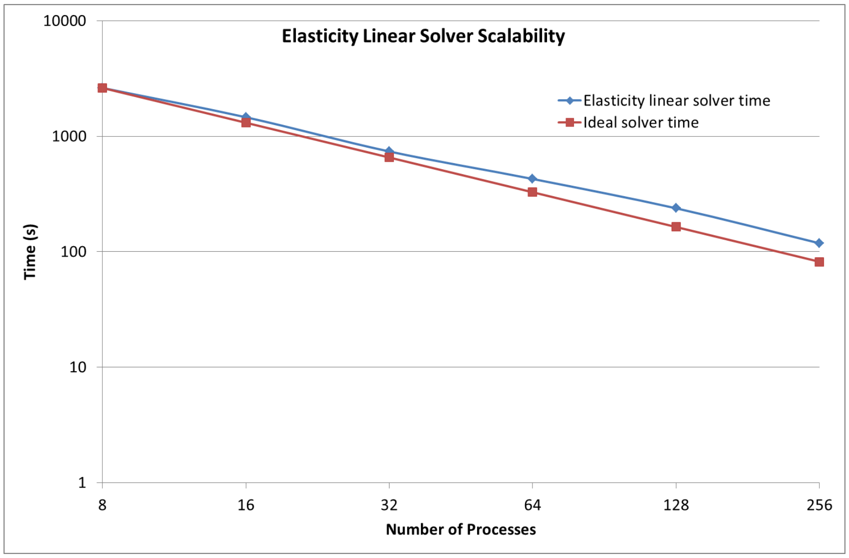

Figure 6.7: Scalability test for coupled mesh case

Number of Processes	Solver Time (s)	Speedup Efficiency
8	2623.572	1
16	1463.32	0.89644507
32	739.651	0.886760107
64	427.321	0.767447656
128	238.169	0.688474361
256	118.508	0.691823548

Table 6.2: Speedup efficiency for coupled mesh case

6.2.3 Large Scale Scalability Test

For the third example in this section, we test the scalability of elasticity linear solvers on up to 2048 processes. We use both the GMRES solver with the BoomerAMG preconditioner from the hypre package [77] and the GMG solver from the UG4 toolbox [61]. The numerical model is a quarter of a 5-spot injection-production problem. The reservoir is 100 ft × 3600 ft × 3600 ft in size with $16 \times 576 \times 576$ rectangular elements. The total number of pressure degrees of freedom is 5308416 and the total number of displacement degrees of freedom is 16979379. An injection well is placed at y=3.125 ft and z=3.125 ft but it is shut-in during the simulation. A rate specified production well is drilled at y=3596.875 ft and z=3596.875 ft. The reservoir fluid has six hydrocarbon components and no-flow boundary conditions are enforced on all surfaces for the compositional flow model. A compressive overburden stress of 4200 psi is prescribed on the top surface of the reservoir for the geomechanics model. All other surfaces have zero normal displacement and zero shear traction boundary conditions. Important parameters are summarized in Table 6.3.

For the purpose of the scalability test, we only ran the simulation for

SYMBOL	QUANTITY	VALUE
t^T	total simulation time	0.1 days
Δt	time step size	0.01 days
LX	reservoir dimension in x	100 ft
LY	reservoir dimension in y	3600 ft
LZ	reservoir dimension in z	3600 ft
NX	number of grids in x	16: $(4 \times 5, 4 \times 7.5, 8 \times 6.25)$ ft
NY	number of grids in y	576
NZ	number of grids in z	576
p_0	initial pressure	$(4\times3984.3, 4\times3990.3, 8\times4000)$ psi
k_{xx}	x-permeability (varies in x)	$(4\times50, 4\times50, 8\times25)$ md
k_{yy}, k_{zz}	y- and z-permeability (varies in x)	$(4\times500, 4\times50, 8\times200)$ md
ϕ_0	initial porosity	0.30
N_c	number of hydrocarbon components	6: C_1, C_3, C_6, C_{10}, C_{15}, C_{20}
c_w	water compressibility	3.3×10^{-6} 1/psi
ρ_w^0	water reference density	62.4 lbm/ft^3
S_w^0	initial water saturation	0.2
n_i	initial hydrocarbon component concentration	0.5, 0.03, 0.07, 0.20, 0.15, 0.05
E	Young's modulus	1.0×10^5 psi
ν	Poisson's ratio	0.3
ρ_s	rock mass density	2.65 g/cm^3
α	Biot's constant	1.0
σ_{ob}	compressive overburden stress	4200 psi
Q_{prod}	constant production rate	12000 BBL/day
DoF_{flow}	number of pressure degrees of freedom	5308416
DoF_{mech}	number of displacement degrees of freedom	16979379

Table 6.3: Parameters for large scale scalability test case

0.1 days with 10 time steps. The total number of elasticity linear system solves is 22 including the initialization step. Both hypre and GMG solvers use a relative tolerance of 1.0×10^{-8}. Tables 6.4 and 6.5 show computation time and speedup efficiencies using hypre and GMG with IPARS's original grid partitioning algorithm (M=1). Scalability results are also plotted in Figure 6.8. Hypre scales better than GMG when more than 128 processes are used, but GMG takes much less absolute computation time than hypre does. The wiggles in the scalability curves in Figure 6.8 are related to mesh partitioning. To see this clearly, we perform additional scalability tests using element-based (M=2) and node-based (M=3) mesh partitioning schemes by METIS. The GMG solver is used in the additional tests. Results are presented in Tables 6.5–6.7 and Figure 6.9. Wiggles in the scalability curves are removed when the mesh is partitioned by METIS. It indicates that METIS produces more consistent mesh partitioning quality. For the geometry of the current problem, the element-based mesh partitioning using METIS leads to the shortest absolute computation time and the best scalability among the three mesh partitioning schemes. It is noticed from the scalability curves that the speedup efficiency deteriorates to below 50% with more than 256 processes. One reason is that the inter-process communication overhead increases as the number of partitions in the mesh increases. The optimal number of processes used in parallel simulation is problem specific. We should point out that the scalability of the elasticity linear solvers in IPARS is not optimal at present. More investigations are required to further improve it.

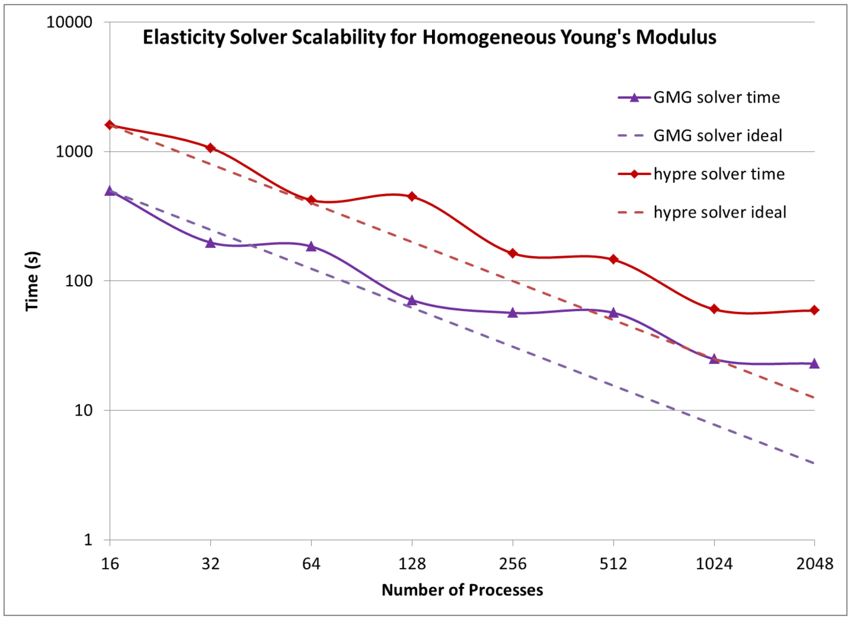

Figure 6.8: Large scale scalability test (M=1)

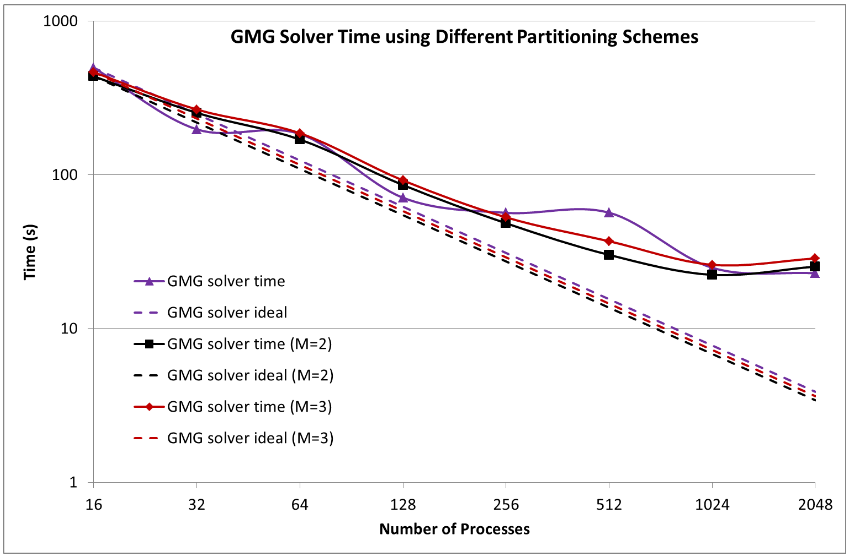

Figure 6.9: GMG scalability with different partitioning schemes

Number of Processes	Solver Time (s)	Speedup Efficiency
16	1597.494385	1
32	1065.671875	0.749524512
64	420.8533936	0.94896133
128	446.7695923	0.446957003
256	163.1486053	0.611978257
512	145.8405914	0.342303189
1024	60.3127174	0.413857157
2048	59.0236702	0.211447794

Table 6.4: Speedup efficiency for hypre (M=1)

Number of Processes	Solver Time (s)	Speedup Efficiency
16	496.5845337	1
32	197.750351	1.255584456
64	184.5298615	0.672769884
128	70.9749451	0.874577171
256	56.6203117	0.548151934
512	56.7251091	0.273569622
1024	24.8560829	0.312162354
2048	22.917141	0.169286678

Table 6.5: Speedup efficiency for GMG (M=1)

Number of Processes	Solver Time (s)	Speedup Efficiency
16	437.4377441	1
32	252.9203949	0.864773567
64	169.7435303	0.644262764
128	85.8347549	0.637034708
256	48.4179764	0.564663397
512	30.143465	0.453495625
1024	22.362711	0.305641152
2048	25.3090801	0.135029893

Table 6.6: Speedup efficiency for GMG (M=2)

Number of Processes	Solver Time (s)	Speedup Efficiency
16	464.7821045	1
32	266.0411377	0.873515481
64	186.3984222	0.623371833
128	91.956337	0.631797274
256	52.8983383	0.549145445
512	36.9891434	0.39266767
1024	25.9923859	0.27939799
2048	28.5843525	0.127031396

Table 6.7: Speedup efficiency for GMG (M=3)

To see the influences of heterogeneities of material properties on the linear solver performance, we replace the homogeneous Young's modulus in the numerical example (see Table 6.3) by a manufactured heterogeneous Young's modulus field. The heterogeneous Young's modulus is generated by the equation

$$\begin{aligned} E &= 1.0 \times 10^5 \times 100^d \\ d &= \frac{1}{3}\left(\left|\sin\left(\frac{x_c}{360}\cdot 2\pi\right)\right| + \left|\sin\left(\frac{y_c}{360}\cdot 2\pi\right)\right| + \left|\sin\left(\frac{z_c}{10}\cdot 2\pi\right)\right|\right) \end{aligned} \quad (6.1)$$

where (x_c, y_c, z_c) are coordinates at center of mass of a grid cell in the mesh. Figures 6.10 and 6.11 show the profile of Lame coefficient λ associated with homogeneous and heterogeneous Young's moduli, respectively. We run scalability tests employing the hypre and the GMG solvers with element-based mesh partitioning scheme (M=2) for the heterogeneous Young's modulus case. Results in Figure 6.12 and Tables 6.8–6.9 show an apparent increase in absolute computation time for both hypre and GMG solvers when heterogeneous Young's modulus is used. Again hypre scales better than GMG especially for large number of processes, but it is slower than GMG in absolute computation time.

In Figure 6.13, we compare the total number of linear iterations using GMG for homogeneous Young's modulus (with M=1, 2, and 3) and heterogeneous Young's modulus. It is clear that the convergence rate of the linear solver depends on the mesh partitioning quality and the heterogeneity of material properties. Figures 6.14–6.19 illustrate pressure, x-displacement, and oil saturation at 0.1 days for both homogeneous and heterogeneous Young's modulus. Results shown are from simulations with 2048 processes.

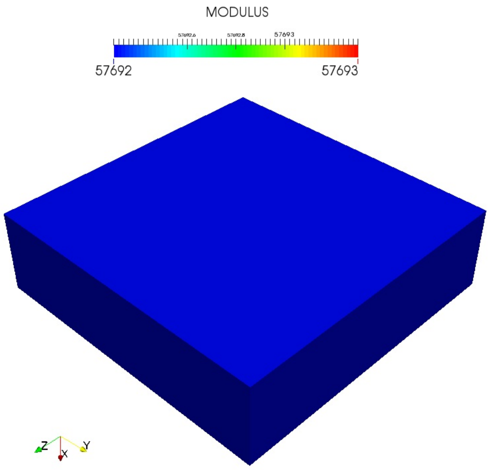

Figure 6.10: Homogeneous Lame coefficient λ

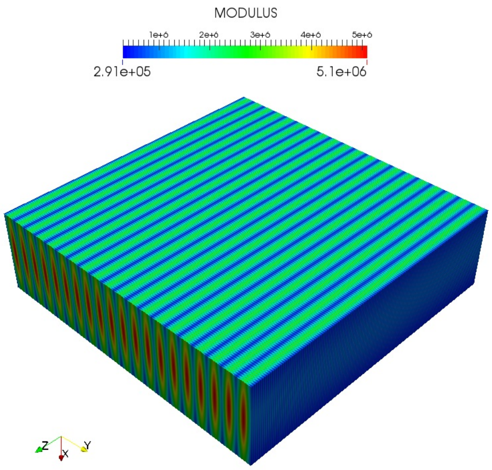

Figure 6.11: Heterogeneous Lame coefficient λ

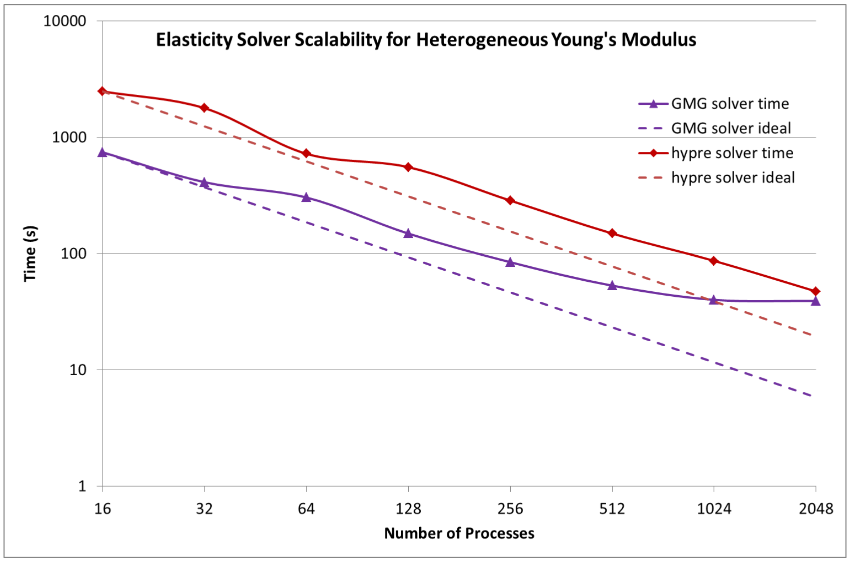

Figure 6.12: Scalability test with heterogeneous E

Number of Processes	Solver Time (s)	Speedup Efficiency
16	2481.227783	1
32	1779.239868	0.69727186
64	721.418335	0.85984361
128	553.7258301	0.560121013
256	285.7250061	0.542748213
512	148.9085388	0.520711363
1024	86.5571136	0.447902922
2048	47.2770844	0.410020886

Table 6.8: Speedup efficiency for hypre with heterogeneous E

Number of Processes	Solver Time (s)	Speedup Efficiency
16	742.9155273	1
32	411.0117798	0.903764276
64	303.509552	0.611937518
128	148.5568085	0.625110635
256	84.3283768	0.55061205
512	52.9948502	0.438082382
1024	40.0372124	0.289931652
2048	39.1412964	0.148283989

Table 6.9: Speedup efficiency for GMG with heterogeneous E

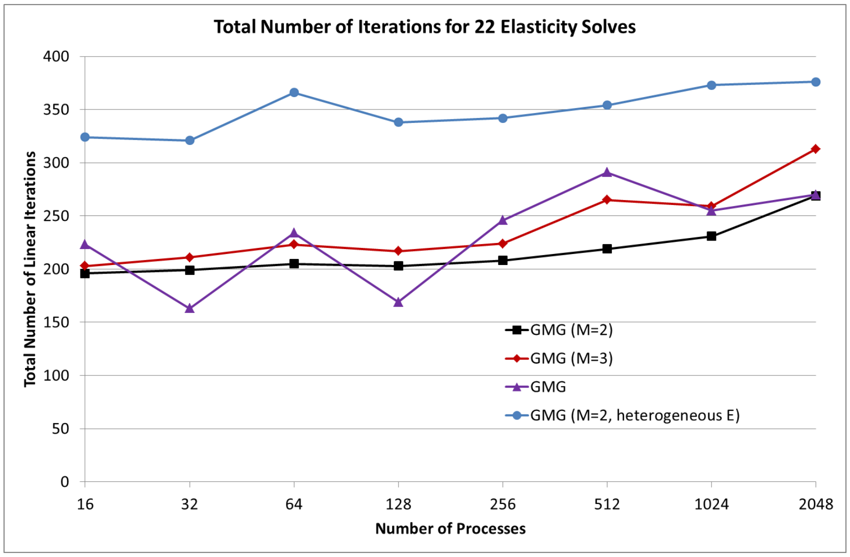

Figure 6.13: Total number of linear iterations using GMG

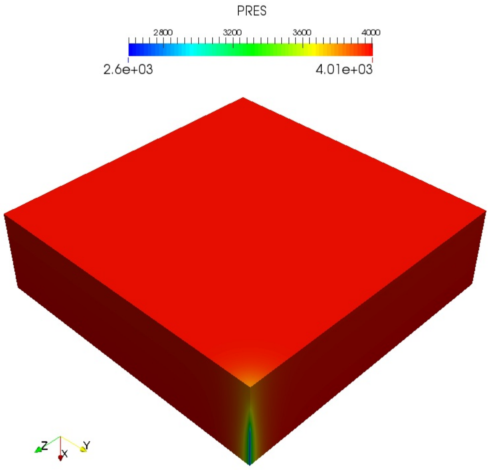

Figure 6.14: Pressure at 0.1 days with homogeneous E

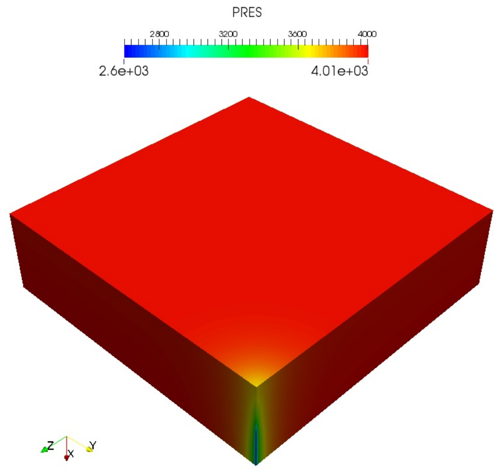

Figure 6.15: Pressure at 0.1 days with heterogeneous E

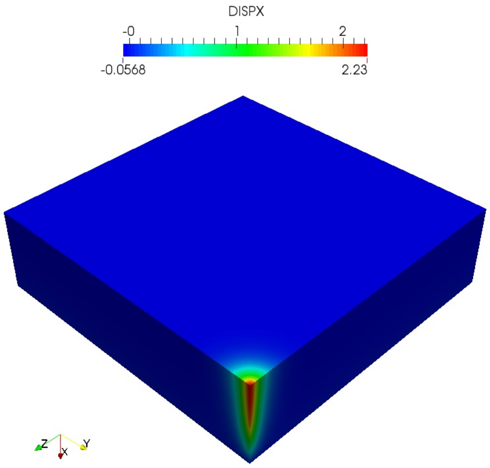

Figure 6.16: X-displacement at 0.1 days with homogeneous E

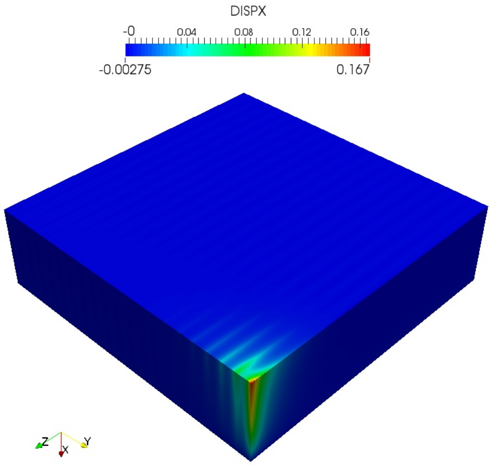

Figure 6.17: X-displacement at 0.1 days with heterogeneous E

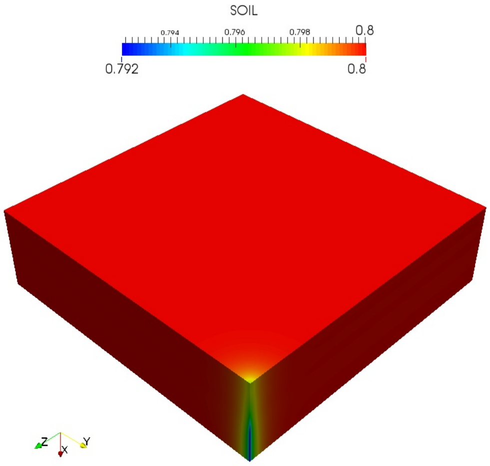

Figure 6.18: Oil saturation at 0.1 days with homogeneous E

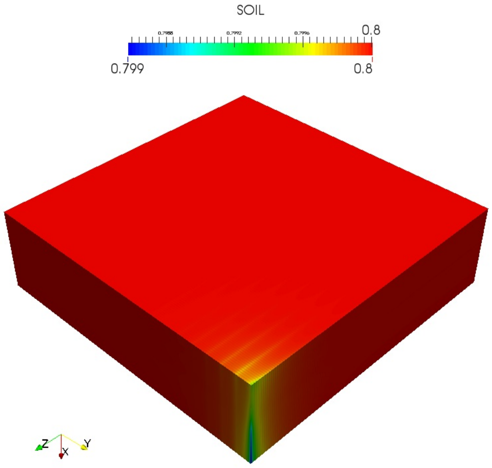

Figure 6.19: Oil saturation at 0.1 days with heterogeneous E

Chapter 7

Conclusions and Future Work

7.1 Conclusions

In this work we developed a coupled poroelasticity simulator under the IPARS framework. The quasi-static isotropic linear elasticity model was iteratively coupled to different flow models. We studied the interactions between reservoir fluid flow, solid skeleton strain and stress, and heat transfer using various numerical examples. We also parallelized the geomechanics model and the two-phase MFMFE flow model. Scalability of linear solvers for the geomechanics model was investigated. Conclusions drawn from this work are as follows:

- We used Mandel's problem as an example to study the convergence behavior of two widely-used iterative coupling schemes, the undrained split and the fixed-stress split. While both coupling schemes yield a convergent solution, the fixed-stress split converges faster than the undrained split. These results verified the theoretical convergence proof given by Mikelić and Wheeler [91].
- We integrated a module for a quasi-static isotropic linear elasticity model on 8-node general hexahedra using CG discretization into IPARS. We

considered both fluid-solid and thermal-solid couplings by treating pressure and thermal loads as external loads in the elasticity model. The GMRES solver with the BoomerAMG preconditioner from the hypre package and the GMG solver from the UG4 toolbox are employed to solve the linear equations for the displacement degrees of freedom.

- We derived model equations for the coupled compositional flow and linear elasticity model under a small deformation assumption. This is an extension to Gai's work [51] which coupled black-oil with the linear elasticity model. Thermal coupling was taken into account in the derivation of the reservoir porosity term. We chose the fixed-stress split to iteratively couple compositional flow and linear elasticity models because it requires minimal modifications to the existing compositional flow model and it converges quickly. The convergence of the iteratively coupled compositional flow and linear elasticity model was verified by a fully implicitly coupled poromechanics simulator.
- We considered permeability coupling between compositional flow and geomechanics models. We showed the geomechanical effects of porosity and permeability coupling on reservoir pressure field by running the Cranfield CO_2 sequestration model with geomechanics and stress-dependent permeability. The results demonstrated that the coupled poromechanics model is necessary for better history matching and prediction in reservoir simulation.

- To account for thermal effects on compositional flow phase behavior and solid structure stress evolution, we explicitly coupled the poromechanics model to a simplified energy conservation model developed by Thomas [126]. A time-split scheme was used to solve heat convection and conduction successively. We showed that temperature variations can have a significant effect on reservoir solid skeleton deformation. The higher order Godunov method used to solve the heat convection equation can well capture the sharp temperature front. We also found that for multiphase flow scenarios, solving the concentration/saturation equation using MFE/CCFD and the temperature equation using Godunov methods leads to non-physical temperature solutions.

- We coupled a linear elasticity model with DOECO2 which is a compositional gas reservoir simulator to account for the geomechanical effects in EOR and CO_2 sequestration processes. The coupled poroelasticity model was validated by comparing numerical results with IPARS. We also tested it with a field scale CO_2 flooding EOR simulation.

- We showed model equations for coupled two-phase flow with a linear elasticity model. The single phase and two-phase flow models were discretized using MFMFE which leads to a cell-centered positive definite pressure system. With numerical examples, we demonstrated that the coupled MFMFE flow and linear elasticity models can handle realistic geometry and boundary conditions. We also showed that for the same physical problem, the simulation with a distorted hexahedral mesh matches its counterpart with a uniform rectangular (smooth) mesh. It verified that the coupled MFMFE flow using a non-symmetric quadrature rule with the CG linear elasticity model yields accurate pressure, velocity, and displacement solutions on distorted hexahedral mesh [144].

- We enhanced the capability of the IPARS framework to handle node-based data communication which is necessary for parallelization of the geomechanics model. We parallelized the two-phase MFMFE flow model in IPARS and tested it with the geomechanics model on a massively parallel computer. Strong scalability tests of the linear solvers for the elasticity model showed good speedup for problems with from a few million to 17 million degrees of freedom on up to 256 processes. Scalability deteriorates as too many processes are used and the inter-process communication cost overwhelms the parallel speedup. Numerical results also showed that the convergence rate of the linear solvers depends on the mesh partitioning quality and the heterogeneity of material properties. The mesh partitioning produced by METIS leads to better solver performance compared to the partitioning generated by the original scheme in IPARS. For the examples tested in this work, the GMRES solver with the BoomerAMG preconditioner is more scalable than the GMG solver from the UG4 toolbox. But the latter is generally much faster than the former in absolute computation time.

7.2 Future Work

We suggest several research directions following this work:

- Add an elastoplasticity model into IPARS and couple it with MFE compositional flow and MFMFE flow models. Plasticity model is needed for simulating problems such as well damage and sand production. It is also needed to account for compaction hysteresis effect which results in permanent porosity and permeability reduction.

- Use Godunov methods to solve the concentration/saturation equation in the compositional flow model to capture the concentration/saturation front. This is necessary for the thermal energy balance model to work in multiphase flow scenarios.

- Further investigate the scalability of linear solvers for the geomechanics model. Currently the speedup efficiency of the linear solvers is not optimal. Fine-tuning of the BoomerAMG preconditioner and the GMG solver are necessary to achieve better performance in both absolute computation time and parallel speedup efficiency.

- We have already implemented utility routines for data decomposition and communication for a two-dimensional non-growing fracture model in IPARS. We have successfully tested the coupled two-phase MFMFE reservoir flow, MFMFE fracture flow, and CG linear elasticity model with several small cases on up to 32 processes. The hypre solver is used to solve the geomechanics system with extra open fracture nodes. Further tests need to be performed with large scale cases and multiple non-planar fractures on more computing processes. Results will be published in a future research paper.

- With the help from Dr. Nägel, adjust the coarsening scheme used in the GMG solver from the UG4 toolbox to treat the additional open fracture nodes in the geomechanics model when fractures exist in the reservoir. Currently the coarsening scheme in the GMG solver for IPARS is based on the tensor-product structure of the mesh (logically rectangular mesh). A new coarsening strategy needs to be developed when additional open fracture nodes break the logically rectangular structure of the mesh.
- Incorporate fracture mechanics models into IPARS for modeling hydraulic fracturing processes.
- Couple the elastoplasticity model with the MFMFE compositional flow model on hexahedral grids and parallelize the MFMFE compositional flow model.

Bibliography

[1] I. Aavatsmark. An introduction to multipoint flux approximations for quadrilateral grids. *Computational Geosciences*, 6(3–4):405–432, 2002.

[2] I. Aavatsmark, G.T. Eigestad, R.A. Klausen, M.F. Wheeler, and I. Yotov. Convergence of a symmetric mpfa method on quadrilateral grids. *Computational Geosciences*, 11(4):333–345, 2007.

[3] Y. Abousleiman, A.H.D. Cheng, L. Cui, E. Detournay, and J.C. Roegiers. Mandel's problem revisited. *Géotechnique*, 46:187–195, 1996.

[4] G. Acs, S. Doleschall, and E. Farkas. General purpose compositional model. *SPE Journal*, 25(4):543–553, 1985.

[5] O. Al-Hinai, G. Singh, G. Pencheva, T. Almani, and M.F. Wheeler. Modeling multiphase flow with nonplanar fractures. In *SPE Reservoir Simulation Symposium*, The Woodlands, Texas, USA, Feb. 2013.

[6] T. Arbogast, L.C. Cowsar, M.F. Wheeler, and I. Yotov. Mixed finite element methods on nonmatching multiblock grids. *SIAM Journal on Numerical Analysis*, 37(4):1295–1315, 2000.

[7] T. Arbogast, G. Pencheva, M.F. Wheeler, and I. Yotov. A multiscale mortar mixed finite element method. *Multiscale Modeling & Simulation*, 6(1):319–346, 2007.

[8] F. Armero. Formulation and finite element implementation of a multiplicative model of coupled poro-plasticity at finite strains under fully saturated conditions. *Computer Methods in Applied Mechanics and Engineering*, 171(3-4):205–241, 1999.

[9] D.N. Arnold. Mixed finite element methods for elliptic problems. *Computer Methods in Applied Mechanics and Engineering*, 82(1-3):281–300, 1990.

[10] M. Bataee and S. Irawan. Review of geomechanical application in reservoir modeling. *Journal of Applied Science*, 14(10):981–990, 2014.

[11] A. N. Beni, A. Varavei, M. Delshad, and R. Farajzadeh. Modeling gas solubility in water for foam propagation in porous media. In *SPE Reservoir Simulation Symposium*, The Woodlands, Texas, USA, Feb. 2013.

[12] M. R. Beygi, M. Delshad, V. S. Pudugramam, G. A. Pope, and M. F. Wheeler. Novel three-phase compositional relative permeability and three-phase hysteresis models. In *SPE Western Regional & AAPG Pacific Section Meeting*, Monterey, California, USA, Apr. 2013.

[13] M.A. Biot. Consolidation settlement under a rectangular load distribution. *Journal of Applied Physics*, 12(5):426–430, 1941.

[14] M.A. Biot. General theory of three-dimensional consolidation. *Journal of Applied Physics*, 12(2):155–164, 1941.

[15] M.A. Biot. Theory of elasticity and consolidation for a porous anisotropic solid. *Journal of Applied Physics*, 26(2):182–185, 1955.

[16] M.A. Biot. General solutions of the equations of elasticity and consolidation for a porous material. *Journal of Applied Mechanics*, 23(1):91–96, 1956.

[17] M.A. Biot. Theory of deformation of a porous viscoelastic anisotropic solid. *Journal of Applied Physics*, 27(5):459–467, 1956.

[18] M.A. Biot. Theory of propagation of elastic waves in a fluid-saturated porous solid. i. low-frequency range. *Journal of the Acoustical Society of America*, 28(2):168–178, 1956.

[19] M.A. Biot. Theory of propagation of elastic waves in a fluid-saturated porous solid. ii. higher-frequency range. *Journal of the Acoustical Society of America*, 28(2):179–191, 1956.

[20] M.A. Biot. Thermoelasticity and irreversible thermodynamics. *Journal of Applied Physics*, 27(3):240–253, 1956.

[21] P.L. Bondor and E. De Rouffignac. Land subsidence and well failure in the Belridge diatomite oil field, Kern county, California. part II. applications. In *The Fifth International Symposium on Land Subsidence*, The Hague, Holland, Oct. 1995.

[22] J.R. Booker and J.C. Small. An investigation of the stability of numerical solutions of Biot's equations of consolidation. *International Journal of Solids and Structures*, 11(7):907–917, 1975.

[23] F. Brezzi, J. Douglas, R. Durán, and M. Fortin. Mixed finite elements for second order elliptic problems in three variables. *Numerische Mathematik*, 51(2):237–250, 1987.

[24] F. Brezzi, J. Douglas, and L.D. Marini. Two families of mixed finite elements for second order elliptic problems. *Numerische Mathematik*, 47(2):217–235, 1985.

[25] W.L. Briggs, V.E. Henson, and S.F. McCormick. *A multigrid tutorial: second edition*. Society for Industrial and Applied Mathematics, Philadelphia, PA, USA, 2000.

[26] Z. Cai, J.E. Jones, S.F. McCormick, and T.F. Russell. Control-volume mixed finite element methods. *Computational Geosciences*, 1(3–4):289–315, 1997.

[27] N. Carrillo. Simple two- and three-dimensional cases in the theory of consolidation of soils. *Journal of Mathematics and Physics*, 21(1):1–5, 1942.

[28] M.M. Carroll and N. Katsube. The role of terzaghi effective stress in linearly elastic deformation. *Journal of Energy Resources Technology*, 105(4):509–511, 1983.

[29] Texas Advanced Computing Center. Stampede user guide.

[30] Y. Chang. *Development and Application of an Equation of State Compositional Simulator*. PhD thesis, The University of Texas at Austin, 1990.

[31] P.A. Charlez. *Mechanics of Porous Continua.* Wiley, New York, 1995.

[32] H.Y. Chen, L.W. Teufel, and R.L. Lee. Coupled fluid flow and geomechanics in reservoir study I. theory and governing equations. In *SPE Annual Technical Conference & Exhibition*, Dallas, Texas, USA, Oct. 1995.

[33] Z. Chen. Expended mixed finite element methods for quasilinear second-order elliptic problems. *Mathematical Modelling and Numerical Analysis*, 32(4):479–499, 1998.

[34] Z. Chen. *Finite Element Methods and Their Applications.* Springer-Verlag, Berlin, 2005.

[35] Z. Chen and L. Douglas. Prismatic mixed finite elements for second order elliptic problems. *Calcolo*, 26(2-4):135–148, 1989.

[36] L.Y. Chin, R. Raghavan, and L.Y. Thomas. Fully coupled geomechanics and fluid-flow analysis of wells with stress-dependent permeability. *SPE Journal*, 5(1):32–45, 2000.

[37] L.Y. Chin and L.K. Thomas. Fully coupled analysis of improved oil recovery by reservoir compaction. In *SPE Annual Technical Conference and Exhibition*, Houston, Texas, USA, Oct. 1999.

[38] L.Y. Chin, L.K. Thomas, J.E. Sylte, and R.G. Pierson. Iterative coupled analysis of geomechanics and fluid flow for rock compaction in reservoir simulation. *Oil & Gas Science and Technology*, 57(5):485–497, 2002.

[39] K.H. Coats. An equation of state compositional model. *SPE Journal*, 20(5):363–376, 1980.

[40] O. Coussy. A general theory of thermoporoelastoplasticity for saturated porous materials. *Transport in Porous Media*, 4:281–293, 1989.

[41] O. Coussy. *Rock Mechanics volume 1: Theoretical Fundamentals.* Editions Technip, Paris, 1991.

[42] C.W. Cryer. A comparison of the three-dimensional consolidation theories of Biot and Terzaghi. *Quarterly Journal of Mechanics and Applied Mathematics*, 16(4):401–412, 1963.

[43] C.N. Dawson and M.F. Wheeler. *The mathematics of finite elements and applications*, chapter An operator-splitting method for advection-diffusion-reaction problems. Academic Press, London, UK, 1987.

[44] Fraeijs de Veubeke. Displacement and equilibrium models in the finite element method. In O.C. Zienkiewicz and G. Holister, editors, *Stress Analysis*, pages 145–197. John Wiley & Sons, New York, 1965.

[45] R.H. Dean. Compositional flow model in IPARSv3. May 2000.

[46] R.H. Dean and J.H. Schmidt. Hydraulic-fracture predictions with a fully coupled geomechanical reservoir simulator. *SPE Journal*, 14(4):707–714, 2009.

[47] R.H. Dean, C.M. Stone X. Gai, and S.E. Minkoff. A comparison of techniques for coupling porous flow and geomechanics. *SPE Journal*, 11(1):132–140, 2006.

[48] M. Delshad, X. Kong, R. Tavakoli, S.A. Hosseini, and M.F. Wheeler. Modeling and simulation of carbon sequestration at cranfield incorporating new physical models. *International Journal of Greenhouse Gas Control*, 18:463–473, 2013.

[49] M. Delshad, S.G. Thomas, and M.F. Wheeler. Modeling co_2 sequestration using a sequentially coupled 'iterative-impec-time-split-thermal' compositional simulator. In 11^{th} *European Conference on the Mathematics of Oil Recovery*, Bergen, Norway, Sep. 2008.

[50] L. Demkowicz, J. Kurtz, D. Pardo, M. Paszynksi, W. Rachowicz, and A. Zdunek. *Computing with Hp-Adaptive Finite Elements, Vol. 2: Frontiers: Three Dimensional Elliptic and Maxwell Problems with Applications.* Chapman & Hall/CRC, Boca Raton, London, New York, 2007.

[51] X. Gai. *A Coupled Geomechanics and Reservoir Flow Model in Parallel Computers*. PhD thesis, The University of Texas at Austin, 2004.

[52] B. Ganis, V. Girault, M.E. Mear, G. Singh, and M.F. Wheeler. Modeling fractures in a poro-elastic medium. *Oil & Gas Science and Technology*, 2013.

[53] B. Ganis, R. Liu, B. Wang, and M.F. Wheeler. *Radon Series on Computational and Applied Mathematics Vol. 12: Simulation of Flow in Porous Media*, chapter Multiscale Modeling of Flow and Geomechanics. De Gruyter, Jul. 2013.

[54] J. Geertsma. The effect of fluid pressure decline on volumetric changes of porous rocks. *Trans. AIME*, 210:331–340, 1957.

[55] J. Geertsma. Problems of rock mechanics in petroleum production engineering. In *1st ISRM Congress*, Lisbon, Portugal, Sep.-Oct. 1966.

[56] R.E. Gibson, G.L. England, and M.J.L. Hussey. The theory of one-dimensional consolidation of saturated clays. I. finite non-linear consolidation of thin homogeneous layers. *Géotechnique*, 17(3):261–273, 1967.

[57] V. Girault, S. Sun, M.F. Wheeler, and I. Yotov. Coupling discontinuous galerkin and mixed finite element discretizations using mortar finite elements. *SIAM Journal on Numerical Analysis*, 46(2):949–979, 2008.

[58] V. Girault, M.F. Wheeler, B. Ganis, and M.E. Mear. A lubrication fracture model in a por-elastic medium. Technical Report ICES REPORT

13-32, The Institute for Computational Engineering and Sciences, the University of Texas at Austin, Dec. 2013.

[59] M. Gutierrez. Fully coupled analysis of reservoir compaction and subsidence. In *European Petroleum Conference*, London, United Kingdom, Oct. 1994.

[60] M. Gutierrez, R.W. Lewis, and I. Masters. Petroleum reservoir simulation coupling fluid flow and geomechanics. *SPE Reservoir Evaluation & Engineering*, 4(3):164–172, 2001.

[61] I. Heppner, M. Lampe, A. Nägel, S. Reiter, M. Rupp, A. Vogel, and G. Wittum. Software framework UG4: Parallel multigrid on the hermit supercomputer. In W.E. Nägel, D.H. Kröner, and M.M. Resch, editors, *High Performance Computing in Science and Engineering '12*, pages 435–449. Springer Berlin Heidelberg, 2013.

[62] L.R. Herrmann. Elasticity equations for incompressible and nearly incompressible materials by a variational theorem. *AIAA Journal*, 3(10):1896–1900, 1965.

[63] T. Hughes. *The Finite Element Method.* Prentice-Hall, Englewood Cliffs, New Jersey, 1987.

[64] R. Ingram, M.F. Wheeler, and I. Yotov. A multipoint flux mixed finite element method on hexahedra. *SIAM Journal on Numerical Analysis*, 48(4):1281–1312, 2010.

[65] N. Inoue and S.A.B. Fontoura. Explicit coupling between flow and geomechanical simulators. In *International Conference on Computational Methods for Coupled Problems in Science and Engineering Proceedings*, Ischia Island, Italy, Jun. 2009.

[66] B. Jha and R. Juanes. A locally conservative finite element framework for the simulation of coupled flow and reservoir geomechanics. *Acta Geotechnica*, 2(3):139–153, 2007.

[67] G. Karypis. METIS: A software package for partitioning unstructured graphs, partitioning meshes, and computing fill-reducing orderings of sparse matrices, Mar. 2003.

[68] G. Karypis and V. Kumar. Multilevel k-way partitioning scheme for irregular graphs. *Journal of Parallel and Distributed Computing*, 48(1):96–129, 1998.

[69] J. Kim, G.J. Moridis, D. Yang, and J. Rutqvist. Numerical studies on two-way coupled fluid flow and geomechanics in hydrate deposits. *SPE Journal*, 17(2):485–501, 2012.

[70] J. Kim, E. Sonnenthal, and J. Rutqvist. Formulation and sequential numerical algorithms of coupled fluid/heat flow and geomechanics for multiple porosity materials. *International Journal for Numerical Methods in Engineering*, 92(5):425–456, 2012.

[71] J. Kim, H.A. Tchelepi, and R. Juanes. Rigorous coupling of geomechanics and multiphase flow with strong capillarity. In *SPE Reservoir Simulation Symposium*, The Woodlands, Texas, Feb. 2011.

[72] J. Kim, H.A. Tchelepi, and R. Juanes. Stability, accuracy, and efficiency of sequential methods for coupled flow and geomechanics. *SPE Journal*, 16(2):249–262, 2011.

[73] J. Kim, H.A. Tchelepi, and R. Juanes. Stability and convergence of sequential methods for coupled flow and geomechanics: Drained and undrained splits. *Computer Methods in Applied Mechanics and Engineering*, 200(23-24):2094–2116, 2011.

[74] J. Kim, H.A. Tchelepi, and R. Juanes. Stability and convergence of sequential methods for coupled flow and geomechanics: Fixed-stress and fixed-strain splits. *Computer Methods in Applied Mechanics and Engineering*, 200(13-16):1591–1606, 2011.

[75] O. Kolditz, S. Bauer, L. Bilke, N. Böttcher, J.O. Delfs, T. Fischer, U.J. Görke, T. Kalbacher, G.T. Kosakowski, C.I. McDermott, C.H. Park, F. Radu, K. Rink, H. Shao, H.B. Shao, F. Sun, Y.Y. Sun, A.K. Singh, J. Taron, M. Walther, W. Wang, N. Watanabe, Y. Wu, M. Xie, W. Xu, and B. Zehner. OpenGeoSys: an open-source initiative for numerical simulation of thermo-hydro-mechanical/chemical (THM/C) processes in porous media. *Environmental Earth Sciences*, 67(2):589–599, 2012.

[76] X. Kong. *Petrophysical Modeling and Simulation Study of Geological CO_2 Sequestration.* PhD thesis, The University of Texas at Austin, 2014.

[77] Lawrence Livermore National Laboratory. hypre user's manual, 2011.

[78] X. Li and O.C. Zienkiewicz. Multiphase flow in deforming porous media and finite element solutions. *Computers & Structures*, 2(45):211–227, 1992.

[79] R. Liu. *Discoutinous Galerkin Finite Element Solution for Poromechanics.* PhD thesis, The University of Texas at Austin, 2004.

[80] J. Lohrenz, B.G. Bray, and C.R. Clark. Calculating viscosities of reservoir fluids from their compositions. *Journal of Petroleum Technology*, 16(10):1171–1176, 1964.

[81] P. Longuemare, M. Mainguy, P. Lemonnier, A. Onaisi, Ch. Gérard, and N. Koutsabeloulis. Geomechanics in reservoir simulation: Overview of coupling methods and field case study. *Oil & Gas Science and Technology*, 57(5):471–483, 2002.

[82] Computer Modelling Group Ltd. User's guide for gem: Advanced compositional and unconventional reservoir simulator, 2012.

[83] B. Lu. *Iteratively Coupled Reservoir Simulation for Multiphase Flow in Porous Media.* PhD thesis, The University of Texas at Austin, 2008.

[84] B. Lu and M.F. Wheeler. Iterative coupling reservoir simulation on high performance computers. *Petroleum Science*, 6(1):43–50, 2009.

[85] J. Lu, P.J. Cook, S.A. Hosseini, C. Yang, K.D. Romanak, T. Zhang, B.M. Freifeld, R.C. Smyth, H. Zeng, and S.D. Hovorka. Complex fluid flow revealed by monitoring co_2 injection in a fluvial formation. *Journal of Geophysical Research*, 2012.

[86] M. Mainguy and P. Longuemare. Coupling fluid flow and rock mechanics: Formulation of the partial coupling between reservoir and geomechanical simulators. *Oil & Gas Science and Technology*, 57(4):355–367, 2002.

[87] J. Mandel. Consolidation des sols. *Géotechnique*, 3:287–299, 1953.

[88] M.N. Mayuga. Geology and development of Californias giant Wilmington oil field. In *M 14: Geology of Giant Petroleum Fields*, page 158184, 1970.

[89] A. Mehrabian and Y.N. Abousleiman. Generalized Biot's theory and Mandel's problem of multiple-porosity and multiple-permeability poroelasticity. *Journal of Geophysical Research: Solid Earth*, 119(4):2745–2763, 2014.

[90] A. Mikelić, B. Wang, and M.F. Wheeler. Numerical convergence study of iterative coupling for coupled flow and geomechanics. *Computational Geosciences*, 2014.

[91] A. Mikelić and M.F. Wheeler. Convergence of iterative coupling for coupled flow and geomechanics. *Computational Geosciences*, 17(3):455–461, 2013.

[92] A. Mikelić, M.F. Wheeler, and B. Wang. Numerical convergence study of iterative coupling for coupled flow and geomechanics. In *13th European Conference on the Mathematics of Oil Recovery*, Biarritz, France, Sep. 2012.

[93] A. Mikelić, M.F. Wheeler, and T. Wick. A phase-field method for propagating fluid-filled fractures coupled to a surrounding porous medium. Technical Report ICES REPORT 14-08, The Institute for Computational Engineering and Sciences, the University of Texas at Austin, Apr. 2014.

[94] S.E. Minkoff, C.M. Stone, S. Bryant, M. Peszynska, and M.F. Wheeler. Coupled fluid flow and geomechanical deformation modeling. *Journal of Petroleum Science and Engineering*, 38(1–2):37–56, 2003.

[95] L.X. Nghiem, D.K. Fong, and K. Aziz. Compositional modeling with an equation of state. *SPE Journal*, 21(6):687–698, 1981.

[96] Department of Petroleum and Geosystems Engineering at The University of Texas at Austin. User's guide for DOECO2 "compositional gas reservoir simulator", 2013.

[97] F. Pan. *Development and Application of a Coupled Geomechanics Model for a Parallel Compositional Reservoir Simulator.* PhD thesis, The University of Texas at Austin, 2009.

[98] F. Pan, K. Sepehrnoori, and L.Y. Chin. A new solution procedure for a fully coupled geomechanics and compositional reservoir simulator. In *SPE Reservoir Simulation Symposium*, The Woodlands, Texas, Feb. 2009.

[99] P. Papadopoulos. Introduction to the finite element method, Aug. 2005.

[100] D.W. Peaceman. Interpretation of well-block pressures in numerical reservoir simulation. In *SPE-AIME* 52^{nd} *Annual Fall Technical Conference and Exhibition*, Denver, Oct. 1977.

[101] D. Peng and D.B. Robinson. A new two-constant equation of state. *Industial & Engineering Chemistry Fundamentals*, 15(1):59–64, 1976.

[102] P.J. Phillips and M.F. Wheeler. A coupling of mixed and continuous galerkin finite element methods for poroelasticity i: The continuous in time case. *Computational Geosciences*, 11(2):131–144, 2007.

[103] P.J. Phillips and M.F. Wheeler. A coupling of mixed and continuous galerkin finite element methods for poroelasticity ii: The discrete-in-time case. *Computational Geosciences*, 11(2):145–158, 2007.

[104] W.E. Pratt and D.W. Johnson. Local subsidence of the goose greek oil field. *The Journal of Geology*, 34(7):577590, 1926.

[105] R. Raghavan and L.Y. Chin. Productivity changes in reservoirs with stres-dependent permeability. *SPE Reservoir Evaluation & Engineering*, 7(4):308–315, 2004.

[106] P.A. Raviart and J.M. Thomas. A mixed finite element method for 2nd order elliptic problems. In *Mathematical Aspects of the Finite Element Method, Lecture Notes in Mathematics*, volume 606, pages 292–315. Springer, New York, 1977.

[107] T. Reza, B. Ganis, S. Sanjay, and M.F. Wheeler. Integration of surface uplift and injection data for estimation of geomechanical properties and reservoir parameters of a co_2 sequestration field using ensemble-based algorithms. In *11th. World Congress on Computational Mechanics*, Barcelona, Spain, Jul. 2014.

[108] J.R. Rice and M.P. Cleary. Some basic stress diffusion solutions for fluid-saturated elastic porous media with compressible constituents. *Review of Geophysics*, 14(2):227–241, 1976.

[109] T.F. Russell and M.F. Wheeler. *The Mathematics of Reservoir Simulation*, chapter Finite element and finite difference methods for continuous flows in porous media, pages 35–106. Society for Industrial and Applied Mathematics, Philadelphia, 1983.

[110] J. Rutqvist, D.W. Vasco, and L. Myer. Coupled reservoir-geomechanical analysis of co2 injection and ground deformations at in salah, algeria. *International Journal of Greenhouse Gas Control*, 4(2):225–230, 2010.

[111] P. Samier and S. De Gennaro. Practical iterative coupling of geomechanics with reservoir simulation. In *SPE Reservoir Simulation Symposium*, Houston, Texas, USA, Feb. 2007.

[112] R.L. Schiffman and D. Znidarcic. Discussion: On Terzaghi's concept of consolidation. *Géotechnique*, 34(1):130–134, 1984.

[113] B.A. Schrefler, R.W. Lewis, and V.A. Norris. A case study of surface subsidence of the polesine area. *International Journal of Rock Mechanics and Mining Sciences and Geomechanics*, 1(4):377–386, 1977.

[114] A. Settari and F.M. Mourits. Coupling of geomechanics and reservoir simulation models. In *Proceedings of Eigth Internatinoal Conference on Computer Methods and Advances*, pages 2151–2158, 1994.

[115] A. Settari and F.M. Mourits. A coupled reservoir and geomechanical simulation system. *SPE Journal*, 3(3):219–226, 1998.

[116] A. Settari and D.A. Walters. Advanced in coupled geomechanics and reservoir modeling with application to reservoir compaction. *SPE Journal*, 6(3):334–342, 2001.

[117] G. Singh, G. Pencheva, K. Kumar, T. Wick, B. Ganis, and M.F. Wheeler. Impact of accurate fractured reservoir flow modeling on recovery predictions. In *SPE Hydraulic Fracturing Technology Conference*, The Woodlands, Texas, Feb. 2014.

[118] P. Song and I. Yotov. Coupling surface and subsurface flows with curved interfaces. In J. Li, H. Yang, and E. Machorro, editors, *Contemporary Mathematics Volume 586: Recent Advances in Scientific Computing and Applications*, pages 331–340. American Mathematical Society, Rhode Island, 2013.

[119] Y.B. Sukirman and R.W. Lewis. Three dimensional fully coupled flow: Consolidation modelling using finite element method. In *SPE Asia Pacific Oil and Gas Conference*, Melbourne, Australia, Nov. 1994.

[120] D.W. Taylor. *Fundamentals of Soil Mechanics.* John Wiley & Sons, London, 1948.

[121] K. Von Terzaghi. Die berechnung der durchlässigkeitsziffer des tones aus dem verlauf der hydrodynamischen spannungsercheinungen. *Sitzungsberichte der mathem. & naturw. Klasse*, 132:125–138, 1923.

[122] K. Von Terzaghi. *Erdbaumechanik auf bodenphysikalischer Grundlage.* Wien, Deuticke, 1925.

[123] K. Von Terzaghi. *Theoretical Soil Mechanics.* John Wiley and Sons, New York, 1943.

[124] K. Von Terzaghi and R.B. Peck. *Soil Mechanics in Engineering Practice.* John Wiley and Sons, New York, 1951.

[125] L.K. Thomas, L.Y. Chin, R.G. Pierson, and J.E. Sylte. Coupled geomechanics and reservoir simulation. *SPE Journal*, 8(4):350–358, 2003.

[126] S.G. Thomas. *On Some Problems in the Simulation of Flow and Transport through Porous Media.* PhD thesis, The University of Texas at Austin, 2009.

[127] D. Tran. *Processes of Coupling between Geomechanics Deformation and Reservoir Flow in Porous Media.* PhD thesis, The University of Calgary, 2002.

[128] D. Tran, L. Nghiem, and L. Buchanan. Improved iterative coupling of geomechanics with reservoir simulation. In *SPE Reservoir Simulation Symposium*, Woodlands, Texas, USA, Jan.–Feb. 2005.

[129] D. Tran, L. Nghiem, and L. Buchanan. An overview of iterative coupling between geomechanical deformation and reservoir flow. In *SPE International Thermal Operations and Heavy Oil Symposium*, Calgary, Alberta, Canada, Nov. 2005.

[130] D. Tran, L. Nghiem, and L. Buchanan. Aspects of coupling between petroleum reservoir flow and geomechanics. In *43rd US Rock Mechanics Symposium and 4th US-Canada Rock Mechanics Symposium*, Asheville, NC, USA, Jun.–Jul. 2009.

[131] D. Tran, A. Settari, and L. Nghiem. New iterative coupling between a reservoir simulator and a geomechanics module. *SPE Journal*, 9(3):362–369, 2004.

[132] J.P. Verdon. *Microseismic Monitoring and Geomechanical Modelling of CO2 Storage in Subsurface Reservoirs.* Springer, New York, 2012.

[133] J. Wan. *Stabilized Finite Element Methods for Coupled Geomechanics and Multiphase Flow.* PhD thesis, Stanford University, 2004.

[134] J.G. Wang, G.R. Liu, and P. Lin. Numerical analysis of biot's consolidation process by radial point interpolation method. *International Journal of Solids and Structures*, 39(6):1557–1573, 2002.

[135] A. Weiser and M.F. Wheeler. On convergence of block-centered finite differences for elliptic problems. *SIAM J. Numer. Anal.*, 25:351–375, 1988.

[136] J. Wheeler, M.F. Wheeler, K. Banas, S. Bryant, S. Chippada, R.H. Dean, J. Eaton, C. Edwards, O. Eslinger, H. Florez, E. Jenkins, S. Lacroix, H. Klie, W. Lee, R. Liu, Q. Lu, B. Momken, M. Noh, M. Parashar, V. Parr, G. Pencheva, M. Peszynska, P. Quandalle, B. Riviere, A. Rodriguez, K. Sephernoori, S. Sun, S. Thomas, Y. Vassilevski, P. Wang, X. Gai, and I. Yotov. IPARS user's manual, Aug. 2007.

[137] M.F. Wheeler and G. Xue. Accurate locally conservative discretizations for modeling multiphase flow in porous media on general hexahedra grids. In *ECMOR XII: 12th European Conference on the Mathematics of Oil Recovery*, Oxford, England, Sep. 2010.

[138] M.F. Wheeler, G. Xue, and I. Yotov. Accurate cell-centered discretizations for modeling multiphase flow in porous media on general hexahedral and simplicial grids. In *SPE Reservoir Simulation Symposium*, Woodlands, Texas, USA, Feb. 2011.

[139] M.F. Wheeler, G. Xue, and I. Yotov. Benchmark 3d: A multipoint flux mixed finite element method on general hexahedra. In J. Fořt, J. Fürst, J. Halama, R. Herbin, and F. Hubert, editors, *Finite Volumes for Complex Applications VI : Problems & Perspectives Springer Proceedings in Mathematics 4*, pages 1055–1065. Springer-Verlag, Berlin, 2011.

[140] M.F. Wheeler, G. Xue, and I. Yotov. A family of multipoint flux mixed finite element methods for elliptic problems on general grids. *Procedia Computer Science*, 4:918–927, 2011.

[141] M.F. Wheeler, G. Xue, and I. Yotov. Local velocity postprocessing for multipoint flux methods on general hexahedra. *International Journal of Numerical Analysis and Modeling*, 9(3):607–627, 2012.

[142] M.F. Wheeler, G. Xue, and I. Yotov. A multipoint flux mixed finite element method on distorted quadrilaterals and hexahedra. *Numerische Mathematik*, 121(1):165–204, 2012.

[143] M.F. Wheeler, G. Xue, and I. Yotov. A multiscale mortar multipoint flux mixed finite element method. *ESAIM: Mathematical Modelling and Numerical Analysis*, 46(4):759–796, 2012.

[144] M.F. Wheeler, G. Xue, and I. Yotov. Coupling multipoint flux mixed finite element methods with continuous galerkin methods for poroelasticity. *Computational Geosciences*, 18(1):57–75, 2014.

[145] M.F. Wheeler and I. Yotov. A cell-centered finite difference method on quadrilaterals. In D.N. Arnold, P.B. Bochev, R.B. Lehoucq, R.A. Nicolaides, and M. Shashkov, editors, *The IMA Volumes in Mathematics and Its Applications*, pages 189–207. Springer, New York, 2006.

[146] M.F. Wheeler and I. Yotov. A multipoint flux mixed finite element method. *SIAM Journal on Numerical Analysis*, 44(5):2082–2106, 2006.

[147] O.C. Zienkiewicz, R. Taylor, and D.D. Fox. *The Finite Element Methods for Solid and Structural Mechanics*. Butterworth-Heinemann, 2013.

[148] D. Znidarcic and R.L. Schiffman. On Terzaghi's concept of consolidation. *Géotechnique*, 32(4):387–389, 1982.

Vita

Bin Wang was born in Fuqing, China in 1984. He is the second child of Mingyu Wang and Ruiyun Zhou. In July 2007, he received his Bachelor of Science degree in Theoretical and Applied Mechanics, with a double-major in Theoretical and Applied Mathematics, from Peking University in China. He enrolled in the PhD program in the Department of Aerospace Engineering and Engineering Mechanics at the University of Texas at Austin in August 2007.

Email: binwang@utexas.edu

This dissertation was typeset with LaTeX[†] by the author.

[†] LaTeX is a document preparation system developed by Leslie Lamport as a special version of Donald Knuth's TeX Program.